Spring 5-2-2022

A Compartmentalized Mathematical Models of Normal and Failing Mouse Cardiac Myocytes

Tesfaye Negash Asfaw

A Compartmentalized Mathematical Models of Normal and Failing Mouse Cardiac Myocytes

by

Tesfaye Asfaw

Under the Direction of Vladimir Bondarenko, Ph.D.

A Dissertation Submitted in Partial Fulfillment of the Requirements for the Degree of

Doctor of Philosophy

in the College of Arts and Sciences

Georgia State University

2022

ABSTRACT

Atrial fibrillations and heart failure are among the leading cardiovascular diseases in the world. Understanding the development and progression of these diseases requires a thorough knowledge of the electrophysiological mechanisms in a healthy and diseased cardiac myocyte. This goal can be achieved by using mathematical modeling along with experimental investigations. Here, we developed two new comprehensive mathematical models of the mouse atrial and ventricular myocytes. The first one is a novel compartmentalized mathematical model of mouse atrial myocytes. This model combines the action potential, $[Ca^{2+}]_i$ dynamics, and β-adrenergic signaling cascade for a subpopulation of right atrial myocytes with a developed transverse-axial tubule system. The model consists of three compartments related to β-adrenergic signaling (caveolae, extracaveolae, and cytosol) and employs local control of Ca^{2+}-release. It also simulates the mechanisms of action potential generation and describes atrial-specific Ca^{2+} handling and frequency dependences of the action potential and $[Ca^{2+}]_i$ transients. The model showed that the T-type Ca^{2+} current significantly affects the later stage of the action potential with little effect on $[Ca^{2+}]_i$ transients. Blocking the small-conductance Ca^{2+}-activated K^+ current leads to the prolongation of the action potential at high intracellular Ca^{2+} concentrations. Simulation results obtained from the atrial cell model were compared to those from ventricular myocytes. The developed model presents a valuable tool for studying complex electrical properties in the mouse atria and could be applied to understand atrial physiology and arrhythmogenesis. The second model is a novel compartmentalized mathematical model of failing mouse ventricular myocytes after TAC procedure. The model effectively describes the cell geometry, action potentials, $[Ca^{2+}]_i$ transients, and β_1- and β_2-adrenergic signaling in the failing cells. Simulation results obtained from a failing cells' model were compared to those from the normal ventricular myocytes. Exploration

of the model revealed the sarcoplasmic reticulum Ca^{2+} load mechanisms in failing ventricular myocytes. We also described a proarrhythmic behavior of Ca^{2+} dynamics upon stimulation with isoproterenol and mechanisms of the proarrhythmic behavior suppression. The developed model can be used to explain the existing experimental data on failing mouse ventricular myocytes and make experimentally testable predictions of the failing myocyte behavior.

INDEX WORDS: Atrial myocytes, T-type Ca^{2+} current, Ventricular myocytes, TAC, β-adrenergic, Heart failure, Late sodium current.

A Compartmentalized Mathematical Models of Normal and Failing Mouse Cardiac Myocytes

by

Tesfaye Asfaw

Committee Chair: Vladimir Bondarenko

Committee: Igor Belykh

Jun Kong

Gennady Cymbalyuk

Electronic Version Approved:

Office of Graduate Services

College of Arts and Sciences

Georgia State University

May 2022

DEDICATION

This dissertation is dedicated to my family and friends, who have been a continuous source of encouragement and support.

ACKNOWLEDGEMENTS

First and foremost, I would like to express my sincere gratitude to my advisor Professor Vladimir E. Bondarenko, for the continuous assistance and guidance that he has given me. He has been supportive since the first day I began working with him. This dissertation would not have been possible without the insight and expertise of Dr. Vladimir E. Bondarenko.

Moreover, I would like to thank my dissertation, candidacy, and qualifying exams committee members, Dr. Igor Belykh, Dr. Gennady Cymbalyuk, Dr. Jun Kong, Dr. Michael Stewart, and Dr. Yaroslav Molkov, for being willing to be on the committees, and their extremely valuable comments despite their busy schedules.

I would also like to thank Dr. Remus Oşan, Dr. Andrey Shilnikov, Dr. Alexandra Smirnova, Dr. Michael Stewart, and all Department of Mathematics and Statistics faculty for providing me with the tools I needed to complete my Ph.D. study successfully.

In addition, I would like to thank friends and family who encouraged and supported me while I was working on my dissertation and all people who contributed in some way to this dissertation.

Finally, I would extend my gratitude to the University System of Georgia (USG) for supporting my education through the Tuition Assistance Program (TAP).

TABLE OF CONTENTS

LIST OF TABLES

LIST OF FIGURES

LIST OF ABBREVIATIONS

AC	Adenylyl cyclase
AMP	Adenosine monophosphate
AP	Action potential
APD	Action potential duration
AV	Atrioventricular
β-AR	Beta-adrenergic
CaM	Calmodulin
CaMKII	Ca^{2+}/calmodulin-dependent protein kinase II
cAMP	Cyclic adenosine monophosphate
Casq2	Calsequestrin 2
GRK2	G Protein-Coupled Receptor Kinase 2
HF	Heart failure
JSR	Junctional Sarcoplasmic Reticulum
LV	Left ventricle
Nav	Voltage-gated sodium channel
PDE	Phosphodiesterase
PKA	Protein kinase A
PKI	Protein kinase inhibitor
PLM	phospholemman
PLN	Phospholamban
PP1	Protein phosphatase 1
RA	Right atria

RyR	Ryanodine receptors
SA	Sinoatrial
SERCA	Sarcoplasmic reticulum Ca^{2+}ATPase
SR	Sarcoplasmic reticulum
TAC	Transverse aortic constriction
TATS	Transverse-axial tubular system
TnC	Troponin C
TNF	Tumor necrosis factor
TnI	Troponin I
TnT	Troponin T

1 INTRODUCTION

1.1 Structure and Electrophysiology of Cardiac Cells

1.1.1 Heart Function

The electrical system of the heart controls the mechanical functioning of the heart. The heart creates electrical impulses (action potentials) and controls the impulses' route via a specific conduction pathway. Myocardial electrical activity is responsible for generating action potentials in individual cardiac cells. The normal coordinated electrical functioning of the whole heart is readily detected in surface electrocardiograms. The functioning of the heart depends on action potential (AP) generation and propagation, followed by relaxation and a period of refractoriness until the next impulse is generated. A cardiac impulse is generated by the sinoatrial (SA) node located in the right atrium (Figure 1.1). The SA node establishes the basic rhythm of the heartbeat and is called the pacemaker of the heart (Klabunde, 2012; Baranchuk et al., 2021).

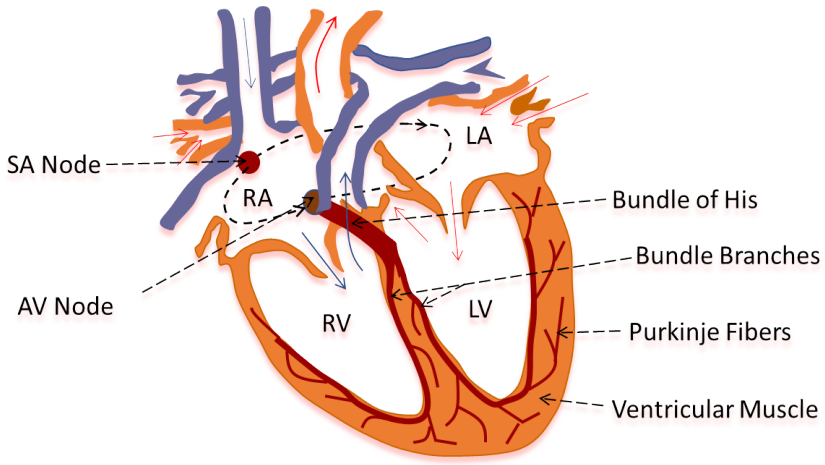

Figure 1.1 *Anatomy of the cardiac conduction system and the path of the action potential propagation*

The electrical impulse generated at the SA node passes into the atria and is transmitted to another mass of specialized cells, the atrioventricular (AV) node, located between the atria and

ventricles. The electrical stimulus from the SA node that reaches the AV node is briefly delayed, which gives the atria time to contract and empty into the ventricles before ventricular contraction occurs. Once the atria are empty of blood, the valves between the atria and ventricles close. At this point, the atria begin to refill, and the electrical stimulus travels down into a large bundle of specialized tissue, the Bundle of His, which conducts it down to the ventricles through the Purkinje fibers. The Purkinje fibers carry the electrical impulse from both the left and right bundle branch to the myocardium of the ventricles. The electric signal that arrives at the ventricle ultimately causes the muscle tissue of the ventricles to contract to eject blood out of the heart (Harmrell, 2018).

The heart's effective pumping action requires precise coordination of the myocardial contractions (millions of cells), which is accomplished via the action potential propagation through the heart.

1.1.2 Action Potential and Ionic Currents in Normal Hearts

An elementary and distinctive property of any excitable cell is its action potential profile. The propagation of cardiac action potential (AP) provides the coupling of the electrical and mechanical functions of the heart, which is essential for normal heart operations. The normal orderly contraction of the atria and ventricles requires the rapid and synchronous activation of groups of cardiac cells (Grant, 2009).

The action potential of myocardial cells is characterized by an initial rapid upstroke followed by a plateau of maintained depolarization and the final repolarization. The duration of the action potential determines the time course of the repolarization of the cell. The generation, duration, and shape of the action potential are the results of the selective permeability of ion

channels distributed on the cell membrane. During the action potential, the permeability of ion channels changes, and each ion moves down its electrochemical gradients.

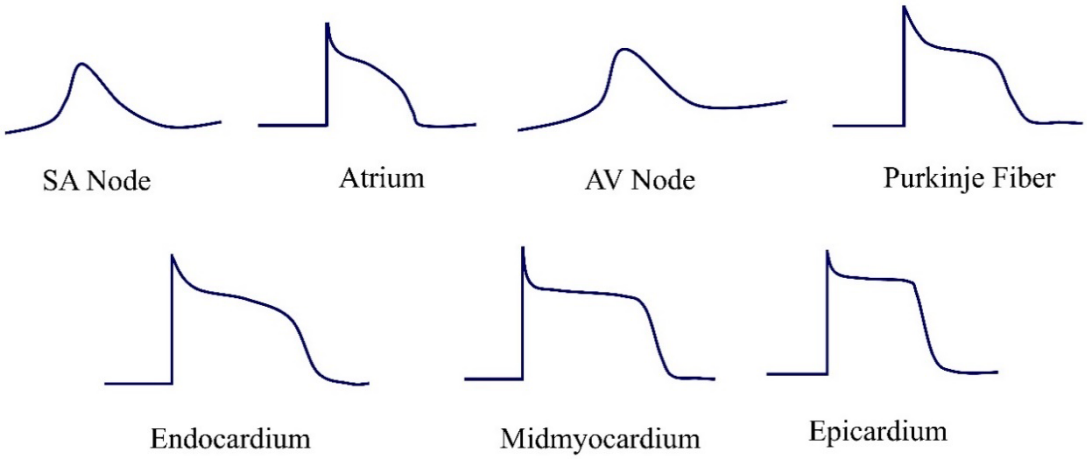

Figure 1.2 *Typical action potential waveforms corresponding to the different regions of the heart.*

The AP is shaped by its underlying ionic currents and varies depending on the species and specific region in the heart, including the sinoatrial node, atria, atrioventricular node, His-Purkinje system, and ventricles (Nerbonne & Kass, 2005; Rahm et al., 2018). The shapes of action potentials in different heart regions are distinct (Figure 1.2). The SA and AV node's action potentials are brief and activate slowly. The atrial and ventricular action potentials activate fast and are longer. Action potential shape and duration are also species-specific because of differences in the sets of underlying inward and outward ionic currents (Nattel et al., 2007; Liu et al., 2016).

The 5 phases of the typical normal action potential for large mammals are shown in Figure 1.3. (Nerbonne, 2004).

Phase 4: Resting potential (-80 to -70 mV). The resting potential in a healthy cardiac myocyte is mainly determined by the inwardly rectifying potassium currents (I_{K1}).

Phase 0: Rapid depolarization phase. Voltage-gated Na^+ channels open to produce the inward fast Na^+ current that depolarizes the cell.

Phase 1: Rapid repolarization phase. This phase sets the potential for the next phase of the action potential. Voltage-gated Na^+ channels inactivate, and some voltage-gated K^+ channels (like the transient outward K^+ currents) begin to open.

Phase 2: A plateau phase. This phase marks the entry of Ca^{2+} into the cell. K^+ efflux continues and is counter-balanced by Ca^{2+} influx. It is the longest phase and is unique among excitable cells.

Phase 3: Final rapid repolarization. This phase restores the membrane potential to resting value. Voltage-gated Ca^{2+} channels close, and delayed rectifier voltage-gated K^+ channels open.

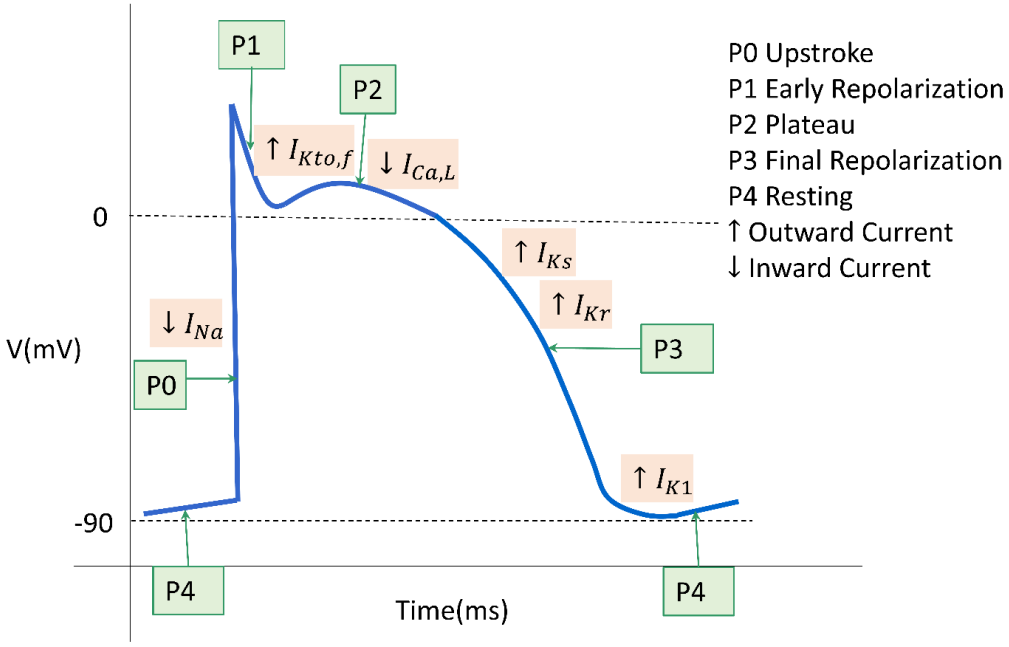

Figure 1.3 *A schematic of typical action potential for human ventricular myocyte.*

In smaller mammals, like mice and rats, the shape of the action potential and the set of repolarization ionic currents are quite different (Figure 1.4). As in large mammals, the AP starts from phase 4 (resting potential of about -80 to -70 mV). Then it is followed by Phase 0, AP upstroke, generated by the activation of the fast Na^+ current. Phase 1 (initial repolarization) is predominantly defined by the rapidly recovering transient outward K^+ current $I_{Kto,f}$. Then the action

potential demonstrates a decaying quasi-plateau (that corresponds to Phase 2 and Phase 3 in the large mammals) defined by competition of the inward Ca^{2+} and outward K^{+} currents. As a result, the murine action potential shows a continuing repolarization phase rather than a distinctive plateau. Finally, the quasi-plateau transfers to phase 4, resting potential.

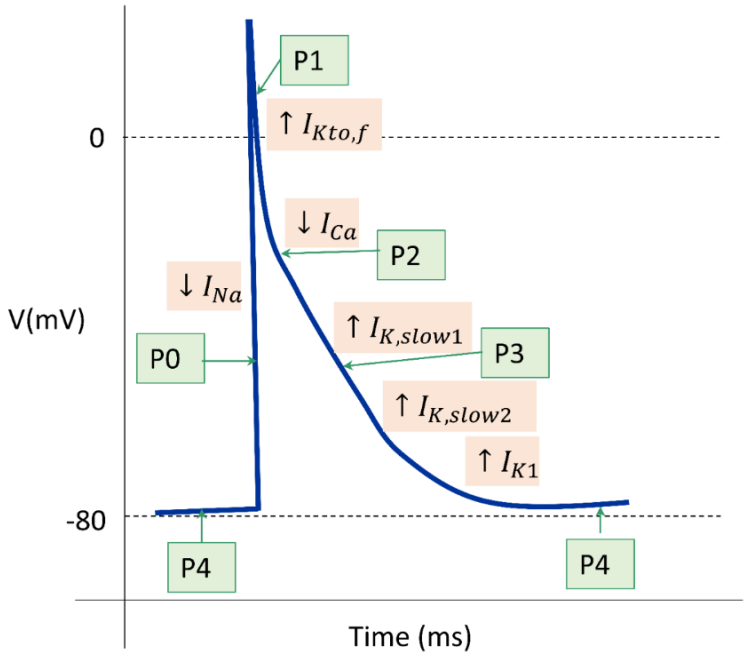

Figure 1.4 *A schematic of typical action potentials for mouse ventricular myocyte.*

In general, the duration of cardiac action potentials increases with body size. The action potential duration for mouse ventricles is about 50 ms (Danik et al., 2002), compared to 250 ms in humans (Edvardssonetal et al., 1984). The shape of the AP is further characterized by measuring its duration at different levels of repolarizations, 25%, 50%, 75%, and 90%. These AP durations are commonly called APD_{25}, APD_{50}, APD_{75}, and APD_{90}. In this dissertation, we will be using APD_{25}, APD_{50}, APD_{75}, and APD_{90} to characterize mouse atrial and ventricular APs.

1.1.3 Structural and Electrical Remodeling in Heart Failure

Heart failure (HF) is one of the leading cardiovascular diseases in the world. HF has been defined as "a complex syndrome that results from any structural or functional impairment of

ventricular filling or ejection of blood" (Yancy et al., 2013). Understanding the development and progression of HF requires an in-depth knowledge of the electrophysiological mechanisms in a healthy and diseased cardiac myocyte. Common denominators of heart failure include ion channel remodeling, cellular uncoupling, altered calcium homeostasis, and extracellular matrix changes. Most of the functional changes in a failing heart result from ion channel remodeling in myocytes. i.e., changes in the expression and function of proteins involved in the electrical activity of cardiac myocytes (Coronel et al., 2013).

1.1.3.1 Structural Remodeling

In failing hearts, cardiac myocytes are increased in size (Konstam et al., 2011). This leads to changes in t-tubules and dyadic space structure. It was found experimentally that the volume density and the surface area of junctional sarcoplasmic reticulum (SR) and those of SR-coupled t-tubules were decreased in failing heart cells (Wu et al., 2012). Moreover, the spatial span of individual t-tubule–SR junctions was markedly reduced in failing heart cells (Wu et al., 2012). Some RyRs move away from T-tubules or lose contact with L-type Ca^{2+} channels and do not participate in Ca^{2+}-induced Ca^{2+} release (Song et al., 2006; van Oort et al., 2011). These structural changes impair Ca^{2+}-induced Ca^{2+}-release, which is responsible for myocyte contraction.

1.1.3.2 Electrical Remodeling

In addition to structural remodeling, failing myocytes demonstrate significant electrical remodeling. The cardiac action potential is generated by the opening and closing of membrane-embedded ion channels, permeable to different ions. The ion channel composition of each cardiac cell contributes to the formation and characteristics of the cardiac action potential that is important for the propagation of electric signals (Bartos et al., 2015). Moreover, ion channel complexes form

the basis for excitation-contraction coupling, including calcium-induced calcium release and mechanical contraction.

Several ion channels are remodeled during the development of heart failure. They were studied in multiple heart failure models that have been developed to assess specific ion channels functions in different animal species (Houser et al., 2012).

Na^+ Currents

The cardiac myocytes depend on a rapid influx of sodium ions (Na^+) to generate an action potential. The influx of Na^+ allows the depolarization of myocytes and propagation of the action potential through the myocardial tissues.

Voltage-gated cardiac Na^+ (Na_v) channels open rapidly upon membrane depolarization (Figure 1.3, Figure 1.4) and underlie the rapidly rising phases of the action potentials in excitable cells. Voltage-gated sodium channel $Na_v1.5$ is the main sodium channel expressed in myocardial cells. The SCN5A gene, found on chromosome 3p21, encodes the $Na_v1.5$ channel. Although the properties of the voltage-gated Na^+ channels expressed in different cardiac cells are similar, these channels' biophysical and pharmacological properties are distinct from Nav channels expressed in other excitable cells, such as neurons and skeletal muscle (Nerbonne & Kass, 2005).

$Na_v1.5$ channels activate at a membrane voltage of about -55 mV, and the activation of these channels is sharply voltage-dependent. The inactivation of Na_v channels is also voltage-dependent. The sodium current (I_{Na}) magnitude is determined by the density of the Na_v channels on the plasma membrane and the channels' opening probability (Dong et al., 2020).

In HF, peak I_{Na} has been shown to be reduced by posttranslational reduction of the alpha subunit $Na_v1.5$ and other posttranslational modifications (Ufret Vincenty et al. 2001).

Late (Persistent) Na^+ current

In addition to the rapidly opening, persistent openings of cardiac Nav channels are occasionally observed at depolarized membrane potentials and action potential plateau (Figure 1.3). The inward Na^+ current through open Na_v channels during the action potential plateau (phase 2) will counter the effects of the increased K^+ efflux, thereby slowing or delaying repolarization and increasing action potential duration. The late sodium current ($I_{Na,L}$) of a normal myocyte is generally small, less than 0.1% of the peak I_{Na}, but it may be much higher (more than three-fold) in a diseased myocyte (Kistamás et al., 2021; Berecki et al., 2006). Therefore, abnormalities in the inactivation of Na^+ channels lead to a persistent late sodium current that causes the prolongation of APD and early afterdepolarizations (EADs) (Ufret-Vincenty et al., 2001; Yu et al., 2018).

The late Na^+ current ($I_{Na,L}$) is increased in several models of HF (Undrovinas et al., 2010; Maltsev & Undrovinas, 2008; Valdivia et al., 2005). Increased late I_{Na} opposes repolarizing currents and lengthens the AP. An increase in late I_{Na} in pathological states also increases Na^+ loading adequately to raise intracellular Na^+. Increased intracellular Na^+ will cause increased intracellular Ca^{2+} because less energy is available in the Na^+ gradient to extrude Ca^{2+} through Na^+/Ca^{2+} exchange (Bers, 2002; Pourrier et al., 2014).

K^+ Currents

In cardiomyocytes, potassium channels are the most abundant and important ion channels dictating the cell's repolarization. They regulate the resting membrane potential, the frequency of pacemaker cells, and the shape and duration of the cardiac action potential. The driving force for K^+ efflux is high during the plateau phase of the action potential in ventricular and atrial myocytes. As the Ca^{2+} channels inactivate, the outward K^+ currents predominate, resulting in repolarization, bringing the membrane voltage back to its resting potential (Grandi et al., 2017).

There are diverse K^+ channel types with distinct kinetic and voltage-dependent properties. Cardiac K^+ currents can be distinguished based on differences in their functional and pharmacological properties. They include the rapidly activating and inactivating transient outward current (I_{Kto}), the ultra-rapidly activating (I_{Kur}), rapidly activating (I_{Kr}), and slow (I_{Ks}) components of the delayed rectifier, and the inward rectifier (I_{K1}). The activation time constants of the currents change in a quite large interval, from fractions of a millisecond to hundreds of milliseconds (Tamargo et al., 2004). The inactivation time constants of K^+ currents also have a large range, from tens milliseconds to seconds (Xu & Nerbonne, 1999; Zhou et al., 2003).

Voltage-gated K^+ currents in myocytes from different species and heart regions have the same time- and voltage-dependent properties. This suggests that the same (or very similar) molecular entities contribute to the generation of each of the various types of voltage-gated K^+ channels in different heart regions and species. However, the kinetics of repolarization varies significantly with the cardiac region and species reflecting the variations in relative levels of K^+ channel expressions. This heterogeneity contributes considerably to the observed regional and species-wide differences in action potential forms. Changes in the properties or the functional expression of voltage-gated K^+ channels, as occurs in various myocardial diseases, can, therefore, have notable effects on action potential waveforms, propagation, and rhythmicity (Nerbonne & Kass, 2005).

Experimental studies show an increase in the whole-cell membrane capacitance (C_m) and a decrease in the $I_{Kto,f}$, $I_{K,slow}$, I_{Kss}, and I_{K1} densities in Transverse Aortic Constriction (TAC) as compared to sham LV myocytes. In addition, a decrease in the amplitude of $I_{K,slow}$, and an increase in the amplitude of I_{Kss} was reported in several TAC models (Marionneau et al., 2008; Tamayo et al., 2020). The inward rectifying potassium current (I_{K1}) stabilizes the resting membrane potential

and is responsible for shaping the action potential's initial depolarization and final repolarization phases. Studies indicate a decrease in the inwardly rectifying K^+ currents I_{K1} in TAC LV myocytes (Marionneau et al., 2008; Nattel, 2008; Näbauer & Kääb, 1998).

Ca^{2+} Currents

In cardiac muscle, two types of Ca^{2+} channels, the L-type (low threshold type) and T-type (transient-type), transport Ca^{2+} into the cells. The L-type channels are found in all cardiac cell types. The T-type channel is found principally in the pacemaker, atrial, and Purkinje cells (Grant, 2009).

The L-type cardiac calcium channel $Ca_v1.2$ plays a critical role in excitation-contraction coupling and action potential duration. The Ca^{2+} ions entering the cardiomyocytes through the $Ca_v1.2$ channels shape the ventricular action potential plateau phase. The L-type Ca^{2+} channels are also required for contraction by inducing calcium release from the sarcoplasmic reticulum. A small influx of Ca^{2+} through $Ca_v1.2$ triggers the ryanodine receptor (RyR) opening and the release of Ca^{2+} ions from the SR. Phosphorylation of RyR channels increases their permeability to calcium and increases the contractility of their respective cardiac myocytes (Shaw & Colecraft, 2013). In addition, the Ca^{2+} ion channel properties can be regulated by drugs and toxins that bind the channel pore, the voltage sensor, or the C terminus.

In general, there are no significant functional abnormalities in the basic properties of I_{CaL} in myocytes isolated from failing human and mouse hearts (Kamp & He, 2002). Available data indicate that I_{CaL} density may be increased in mild hypertrophy but unchanged in moderate degrees of hypertrophy and at the early stages of heart failure (Toischer et al., 2010; Li et al., 2013; Tamayo et al., 2020).

1.1.4 Calcium Handling in Heart Failure

The influx of Ca^{2+} into the cytosol as Ca^{2+} current (I_{Ca}) and the release of Ca^{2+} from the sarcoplasmic reticulum are central to the excitation-contraction coupling (Fig. 1.5). The triggering Ca^{2+} current (I_{Ca}) is generated by the L-type Ca^{2+} channels expressed in the transverse tubules (T-tubules) and is initiated by membrane depolarization. The excitation-contraction coupling is achieved by increasing cytosolic $[Ca^{2+}]_i$ levels from nanomolar (100 nmol/L) to micromolar (10 μmol/L) (Walker and Spinale, 1999). Precise regulation of Ca^{2+} is vital for the proper myocyte function (Bers, 2000). Depolarization of the myocyte triggers the entry of small amounts of Ca^{2+} through the L-type Ca^{2+} channels located on the cell membrane, which in turn prompts SR Ca^{2+} release through ryanodine receptors, a process known as calcium-induced calcium release. The rapid rise in cytosolic levels activates Ca^{2+}–troponin-C interactions and induces sarcomere contraction. For relaxation to occur, Ca^{2+} must dissociate from troponin C, which requires a reduction in cytosolic Ca^{2+}. The activity of the sarcoplasmic reticulum Ca^{2+}-ATPase (SERCA), an ATP-dependent calcium pump, returns cytosolic Ca^{2+} into the SR to restore the background Ca^{2+} level. In addition to the SERCA pump, Ca^{2+} extrudes the cytosol via the sarcolemmal Na^{+}/Ca^{2+} exchanger (NCX) and Ca^{2+} pump.

The two major factors determining the rate, strength, and duration of myocyte contraction are the amount and rate of Ca^{2+} delivered to and removed from the cytoplasm. The SR Ca^{2+} load is essential in determining the amount of SR Ca^{2+} released in response to each inward Ca^{2+} current.

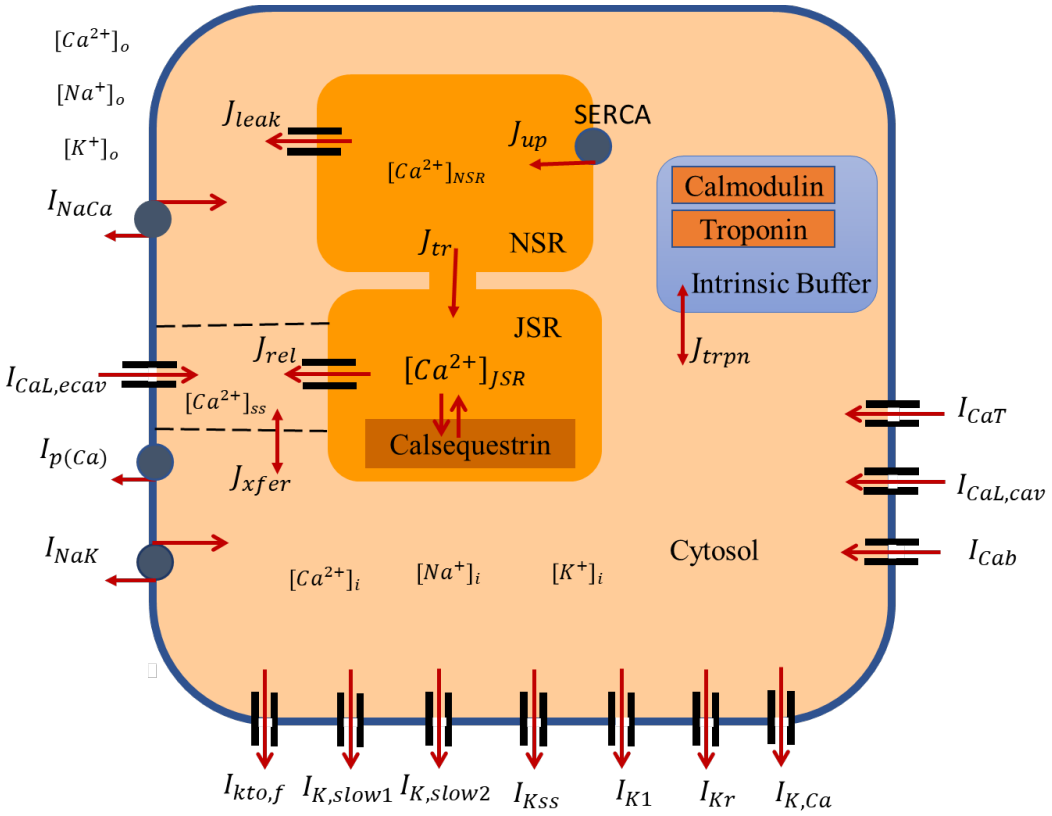

Figure 1.5 *Schematic diagram of the mouse atria model ionic currents and Ca^{2+} fluxes.*

Alterations in myocyte ion currents and Ca^{2+} handling proteins can contribute to heart failure by causing structural remodeling and ventricular hypertrophy. Studies indicate that SR Ca^{2+} load is reduced in heart failure (Hobai & O'Rourke, 2001; Lindner et al., 1998). Moreover, the Ca^{2+} transient from failing hearts exhibits a reduced rate of Ca^{2+} removal from the cytosol (Tamayo et al., 2020). A failing human heart also shows increased resting intracellular Ca^{2+} level, leading to diastolic dysfunction (Beuckelmann et al., 1992; Eisner et al., 2020).

Sarcoplasmic Reticulum Ca^{2+}-ATPase (SERCA)

To restore the myocardial relaxation, Ca^{2+} is mainly returned to intracellular stores by the cardiac isoform sarcoplasmic reticulum Ca^{2+} ATPase 2a (SERCA2a) and into the extracellular space by the Na^+/Ca^{2+} exchanger. In humans and other bigger animals, 70-80% of the systolic Ca^{2+} is removed from the cytosol by SERCA and 20-30% by Na^+/Ca^{2+} exchanger (Frank et al., 2003).

In contrast, SERCA plays a more predominant role in rat and mouse cardiac myocytes with an approximately 90% contribution to removing Ca^{2+} and about 7-10% by Na^{+}/Ca^{2+} exchanger. Upon sarcoplasmic resequestration, Ca^{2+} binds mainly to the SR Ca^{2+} storage protein, calsequestrin, and other Ca^{2+}-binding proteins, such as calreticulin and the histidine-rich-binding proteins (Bers, 2002).

In both experimental and clinical heart failure, SERCA2a expression is significantly reduced, leading to abnormal Ca^{2+} handling and impaired contractility. Inefficient SR Ca^{2+} uptake in myocytes is associated with a decrease in the expression and activity of the SERCA2a (Lipskaia et al., 2013; del Monte & Hajjar, 2008)

Phospholamban (PLN)

PLN is an SR protein that regulates the activity of SERCA. In the dephosphorylated form, PLN decreases the apparent Ca^{2+}-affinity of SERCA2a. The inhibitory effect of PLN on SERCA is removed because of the dissociation of the PLN/SERCA2a complex upon phosphorylation of PLN through β-adrenergic stimulation and enhanced cyclic adenosine monophosphate (cAMP) - dependent protein kinase A (PKA) activity (Frank & Kranias, 2000; Maier & Bers, 2007**).** The PLN levels show no change in a mouse failing myocyte (Vinet et al., 2012).

Calsequestrin

Calsequestrin is the major calcium-binding protein in the sarcoplasmic reticulum. It is the most abundant Ca^{2+} binding protein in the junctional SR of cardiac muscle. Experiments on mice show that removing the cardiac variant calsequestrin (Casq2) causes a steep increase in SR Ca^{2+} release supporting the regulatory effect of Casq2. An increase in $[Ca^{2+}]_{SR}$ also increases RyR open probability resulting in a much higher likelihood of SR Ca^{2+} release. (Lukyanenko et al. 1996;

Gyorke & Gyorke, 1998; Györke et al., 2009). Experimental data on failing mouse ventricular myocytes show no change in the expression of calsequestrin (Vinet et al., 2012)

1.1.5 The β-adrenergic Pathway

The β-adrenergic receptors (β-ARs) are G-protein coupled receptors located on the sarcolemma. Two major subtypes of β-ARs (β_1-AR, β_2-AR) have been identified in cardiac cells. Each subtype has different affinities for different ligands, which allow independent activation of each subtype. While β_2-AR is coupled to both G_s and G_i proteins in cardiomyocytes, β_1 is associated only with G_s proteins. The β_1 subtype is the most prominent in cardiac cells. In normal human cardiac myocytes, there is approximately a 4:1 ratio of β_1-AR to β_2-AR (de Lucia & Koch, 2018; Lohse et al., 2003; Zhu et al., 2011). In mice, the β_1-AR to β_2-AR ratio is 2:1 (Hilal-Dandan et al., 2000).

By stimulating the β-adrenergic pathways, the sympathetic nervous system can significantly enhance the Ca^{2+} circulation mechanisms and hence the excitation and contraction of cardiomyocytes. In the cardiomyocyte's sarcolemma, agonists such as epinephrine and norepinephrine bind to β_1- or β_2-adrenergic receptors, ultimately leading to the phosphorylation of $Na_V1.5$, $Ca_V1.2$, RyR, PLN, and other proteins. The binding of agonists to the β-adrenergic receptors activates adenylyl cyclase (AC), resulting in cAMP production from the hydrolysis of ATP. The cAMP acts as a second messenger to activate protein kinase A (cAMP-dependent protein kinase), which can phosphorylate different targets within the cell (Wachter et al., 2012; Lohse et al., 2003; Woo & Xiao, 2012).

PKA plays multiple roles in heart function regulation, including contraction, metabolism, ion fluxes, and gene transcription. PKA is a protein comprised of two catalytic (PKA-C) and two regulatory (PKA-R) subunits (Wachter & Gilbert, 2012). The binding of cAMP to the PKA-R

subunits induces the release of PKA-C, allowing the phosphorylation of many target proteins involved in the excitation-contraction (E–C) coupling mechanism, such as cardiac troponin I (cTnI), cardiac myosin binding protein C (cMyBPC), phospholamban (PLB), L-type calcium channel, phosphodiesterase (PDE), cAMP-response element-binding protein (CREB), and the ryanodine receptors to modify their function. PKA phosphorylation increases the RyR and SERCA activities, causing a faster opening and closing of the channels. The simultaneous increase of RyR and SERCA activities from PKA phosphorylated PLN results in overall hastened SR Ca^{2+} release and uptake (Marks, 2013; Najafi et al., 2016).

Thus, the net effect of β-adrenergic stimulation is to increase the overall amplitude of Ca^{2+} transients by accelerating the cardiomyocyte's Ca^{2+} channels and pumps, Ca^{2+} transport activities. Isoproterenol, a β-AR agonist, increases the strength of the cardiac contraction by increasing the level of myocardial cAMP. cAMP levels are tightly regulated by the cyclic nucleotide degrading enzymes phosphodiesterases (PDEs). PDEs break down cyclic nucleotide phosphodiesterases, such as cAMP and cGMP. PDE isoforms, PDE4 and PDE8, are specific for cAMP degradation, while PDE1, PDE2, and PDE3 can hydrolyze cAMP and cGMP (Najafi et al., 2016).

The activation of the inhibitory G-protein (G_i-protein) inhibits the β-adrenergic signaling system. Therefore, the stimulation of this pathway inactivates PKA, decreases Ca^{2+} entry into the cell, and Ca^{2+}release by the sarcoplasmic reticulum (Klabunde, 2012).

Researches suggest that the β-adrenergic receptor system plays a major role in heart failure. Studies indicate a reduction of the β_1-AR density on the plasma membrane from a failing heart by about 50%. In contrast, β_2-AR shows no such change in the failing heart. (Madamanchi, 2007; Bristow et al., 1989; Woo & Xiao, 2012)

1.2 Mathematical Models of Mouse Atrial Myocytes

Mathematical modeling of cardiac myocytes and tissues is complementary to the experimental investigations and a potent tool for studying cardiac electrical activity, intracellular Ca^{2+} dynamics, protein signaling networks, pathological remodeling, and arrhythmogenesis. Multiple mathematical models have been developed to describe experimentally observed behavior of cardiac myocytes from different heart regions, such as ventricles, atria, sino-atrial node, Purkinje fibers, and others (Bondarenko et al., 2004; Demir et al., 1994; Jafri et al., 1998; Nygren et al., 1998; Vaidyanathan et al., 2013). The majority of the mathematical models are species-specific; they describe the behavior of cardiac cells from the human, dog, rabbit, guinea pig, rat, and mouse hearts.

Prevailing fractions of mathematical models have been developed for ventricular myocytes, which allowed the simulations of action potential and $[Ca^{2+}]_i$ transients. These models have also simulated the frequency dependence and role of AP and $[Ca^{2+}]_i$ transients in pro-arrhythmic activity (see, for example, (Bondarenko et al., 2004; Grandi et al., 2010; Jafri et al., 1998; Luo & Rudy, 1994)). Less attention has been given to the atrial cardiomyocytes, perhaps, due to less severe consequences of atrial arrhythmias and/or because of the more complex atrial structure and dynamics. However, recent experimental focus has turned to the heart atria and atrial cells (Heijman et al., 2016), which in turn demanded comprehensive models of atrial myocytes.

More than 300 computational studies have used mathematical models for the atrial myocyte of different species to simulate atrial electrophysiology, Ca^{2+} dynamics, arrhythmias, and therapeutic interventions (Heijman et et., 2016). Initially, they focused on a different shape of atrial AP as compared to that in ventricular myocytes and were developed for various species, including rabbits, dogs, and humans (Courtemanche et al., 1998; Hilgemann & Noble, 1987; Nygren et al.,

1998; Ramirez et al., 2000). Later modeling studies have been devoted to the differences in Ca^{2+} dynamics between atrial and ventricular myocytes (see (Heijman et al., 2016) for a comprehensive review), including compartmentalized Ca^{2+} signaling and coherent local control of Ca^{2+}-induced Ca^{2+} release (Jafri et al., 1998). The modeling of atrial myocytes is also complicated by their complex structure. Atria consists of both myocytes with transverse-axial tubule system (TATS) and those that do not have TATS (Glukhov, Balycheva, et al., 2015; Lenaerts et al., 2009). In addition, atrial and ventricular myocytes demonstrate different expressions of Ca^{2+} handling proteins (Gaborit et al., 2007; Lüss et al., 1999), which also need to be considered in mathematical modeling.

Most of the mathematical atrial cell models have been developed for human myocytes (Courtemanche et al., 1998; Koivumäki et al., 2011; Grandi et al., 2011; Nygren et al., 1998). There also exist detailed models for rabbits (Hilgemann & Noble, 1987; Lindblad, 1996), bullfrogs (Rasmusson et al., 1990), and canine (Kneller et al., 2002; Ramirez et al., 2000) atrial myocytes. For mice, an atrial AP model by Davis et al. (2014) was modified from a ventricular cell model (Bondarenko et al., 2004), where the ventricular ion currents were adjusted to reproduce atrial AP. However, the model by Davis et al. (2014) did not include atrial-specific ionic currents, namely the T-type Ca^{2+} current (I_{CaT}) and the small-conductance Ca^{2+}-activated K^+ current ($I_{K,Ca}$), and lacked the vital differences in Ca^{2+} dynamics between atrial and ventricular myocytes.

In this study, we developed a comprehensive compartmentalized mathematical model of mouse atrial myocytes. The model was designed for a subpopulation of right atrial myocytes with developed TATS that was observed experimentally in a substantial fraction (23-84%) of mouse atrial myocytes (Yue et al., 2017). Importantly, our new model 1) has a revised cell geometry, 2) includes atrial-specific ion currents I_{CaT} and $I_{K,Ca}$, and 3) formulates atrial AP, Ca^{2+} dynamics, and

β-adrenergic signaling system in a compartmentalized manner which is based on a rigorous review of the latest experimental studies on mouse atrial myocytes (Fig. 2.1). We also reformulated the outward K^+ currents by separating I_{Kur} into $I_{K,slow1,}$ and $I_{K,slow2}$ due to their differential response to β-adrenergic stimulation and made several other model adjustments to fit experimental data. The resulting model was able to generate, with high accuracy, the mouse's right atrial AP, $[Ca^{2+}]_i$ and $[Na^+]_i$ dynamics, and their frequency dependences. It also recapitulates voltage-clamp experiments for the $I_{Ca,T,}$ and the $I_{K,Ca}$ currents and estimate their impact on AP and $[Ca^{2+}]_i$ generation at baseline and under β-adrenergic stimulation. We also showed the differences in the AP, $[Ca^{2+}]_i$ transients, and Ca^{2+} fluxes in mouse atrial and ventricular myocytes models. Finally, a sensitivity analysis of the model was performed to demonstrate the stability of the model with respect to perturbations due to the cell-to-cell variability of the ionic currents within the mouse right atria.

1.3 Mathematical Models of Heart Failure

Heart failure is a complex cardiac disease that manifests in a significantly reduced heart fractional shortening and ejection fraction, generally due to decreased intracellular calcium transients ($[Ca^{2+}]_i$) and myocyte contractions. Heart failure is considered as the final common pathway of many cardiac pathologies (Coronel et al., 2013). At the cellular level, heart failure progression results in structural and functional remodeling that affects cell structure, properties of ionic currents and transporters, and cellular signaling systems (Tomaselli & Marban, 1999; Nattel et al., 2007). The failing cardiac myocytes increase in size, which is accompanied by adaptive and maladaptive changes in t-tubules structure, sarcoplasmic reticulum size, dyadic space, and contractile protein expression (Schaper et al., 2002; Li et al., 2013). In addition, cardiac myocytes from failing hearts exhibit the prolongation of the action potential, resulting from the destruction of the delicate balance between the depolarizing and repolarizing currents. In most cases, failing

myocytes show a decrease in the fast Na^+ current (I_{Na}), the transient outward K^+ currents ($I_{Kto,f}$ and $I_{Kto,s}$), the time-independent inwardly rectifying K^+ current (I_{K1}), and the slow delayed-rectifier K^+ current (I_{Ks}); no change in the rapid delayed-rectifier K^+ current (I_{Kr}) and the L-type Ca^{2+} current (I_{CaL}); and an increase in the late Na^+ current (I_{NaL}) and the Na^+/Ca^{2+} exchanger current (I_{NaCa}) (Tomaselli & Marban, 1999; Nattel et al., 2007; Rivaud et al. 2017). Further, the Ca^{2+} dynamics was found to be impaired, in the failing myocytes, due to a reduction in the function of the SERCA2a pump, an increase in the functions of the Na^+/Ca^{2+} exchanger, and an increase in Ca^{2+} leak from the sarcoplasmic reticulum (Nattel et al., 2007). Finally, the modified β_1- and β_2-adrenergic signaling in the failing hearts resulted in blunted response to adrenergic stimulation (Woo & Xiao, 2012).

Multiple experimental models of heart failure have been investigated in different species, including humans (Zaragoza et al., 2011; Riehle & Bauersachs, 2019; Spannbauer et al., 2019). The mouse is the most studied species used in heart failure investigations. Several models of heart failure have been developed for mice that include genetic modifications (van Oort et al., 2011), myocardial infarction (Yoo et al., 2009), and transverse aortic constriction (TAC) (Li et al., 2013; Ljubojevic-Holzer et al., 2020), etc. Specifically, experimental models of mouse heart failure using TAC demonstrate structural remodeling, the changes in properties of ionic currents and transporters, and cellular signaling systems similar to those seen in larger animals and humans (Nienaber et al., 2003; Fabritz et al., 2010; Li et al., 2013; Bryant et al., 2018; Ljubojevic-Holzer et al., 2020).

In addition to the common features of heart failure, such as action potential prolongation, reduced $[Ca^{2+}]_i$ transient, reduced sarcoplasmic reticulum Ca^{2+} load, reduced transient outward K^+ currents ($I_{Kto,f}$ and/or $I_{Kto,s}$), and increased I_{NaCa}, experimental investigations also resulted in several

controversial findings (Tomaselli & Marban, 1999; Nattel et al., 2007). The data on modifications of the SERCA pump demonstrates a decrease in function and mRNA expression but a reduction or no change in corresponding protein expression (Nattel et al., 2007). This finding is closely related to the alterations of phospholamban expression, in which mRNA is reduced, but protein expression demonstrates a reduction or no change. There are also different interpretations of the role of the SERCA pump, the Na^+/Ca^{2+} exchanger, and the ryanodine receptor leak in the reduction of the SR Ca^{2+} load (Bers et al., 2003).

Several mathematical models have been developed to describe failing cardiomyocytes in different species (see (Gomez et al., 2015) for review) to address the issues encountered in the experimental investigations of failing hearts. The first mathematical model of the failing myocytes was developed by Priebe and Beuckelmann for the human ventricle (1998). In their model, the authors considered both normal and failing human ventricular myocytes. In the failing myocytes, they changed several model parameters as compared to the normal myocytes: reduced the transient outward K^+ current, the inward-rectifier K^+ current, the Na^+-K^+ pump, and SERCA pump function, but increased the Na^+/Ca^{2+} exchanger function and Ca^{2+} leak, and did not change the delayed rectifier currents I_{Kr} and I_{Ks} and cell geometry. The model simulated prolongation of the action potential and a reduction of $[Ca^{2+}]_i$ transient, which have been observed experimentally. In addition, Priebe and Beuckelmann have shown larger susceptibility of the failing human ventricular myocytes to early afterdepolarizations (EAD) (Priebe and Beuckelmann, 1998). A similar approach, with some changes in the model's current parameters, has been applied in the mathematical model for the failing canine ventricular myocytes, developed by Winslow et al. (1999). They simulated the prolongation of the action potential and the reduction of $[Ca^{2+}]_i$ transient in the failing myocytes and estimated the differences in the Na^+/Ca^{2+} exchanger and

SERCA pump function between normal and failing myocytes. Yet another mathematical model of failing rabbit ventricular myocyte has been explored by Shannon et al. (2005). It was found that the $[Ca^{2+}]_i$ transient and the SR load were reduced in the failing myocytes. In addition, failing rabbit ventricular myocytes had more depolarized resting potential and were more susceptible to delayed afterdepolarizations (DAD). A mathematical model of failing mouse ventricular myocytes overexpressing TNF-α has also been investigated by Petkova-Kirova et al. (2012). The model simulated action potential prolongation and $[Ca^{2+}]_i$ transient reduction that resulted in the instability of the action potential and Ca^{2+} dynamics in the failing myocytes at lower stimulation frequencies. At the cardiac tissues level, the heart failure model by Petkova-Kirova et al. (2012) demonstrated higher susceptibility to the action potential block, Ca^{2+} alternans, and re-entry.

More recently, attention was paid to the structural changes and their possible significant effects in mathematical models of failing cardiac cells (Polakova & Sobie, 2013). It was suggested by Polakova & Sobie (2013) that the models should consider the changes in t-tubule and dyadic space structure that occurs upon the development of heart failure, which plays an important role in Ca^{2+} homeostasis. Later, the role of re-distribution of the L-type Ca^{2+} channels on the development of EADs in failing human ventricular myocytes was modeled by Sanchez-Alonso et al. (2016). It was demonstrated that redistribution of the L-type Ca^{2+} channels from t-tubules to crest regions in the failing myocytes promoted EADs. In addition, sensitivity analysis of the human failing myocyte model (Mora et al., 2017) revealed the important contribution of the SERCA pump dysfunction to the altered Ca^{2+} homeostasis, with the Na^+/Ca^{2+} exchanger and other Ca^{2+} cycling proteins also playing a significant role.

Finally, a compartmentalized mathematical model of human failing ventricular myocytes that includes modifications of the β-adrenergic signaling system in addition to alteration of the

ionic currents and transporters has been developed (Mora et al., 2021). The model simulated multiple features of the human failing ventricular cells, such as the prolongation of the action potential, reduced $[Ca^{2+}]_i$ transients, and blunted response of the failing myocytes to adrenergic stimulation.

While multiple mathematical models of the failing ventricular myocytes for several species have been developed, they did not consider the increase in the myocyte size that was consistently observed in the failing myocytes. In addition, despite multiple experimental heart failure models developed for mice, there is no comprehensive mathematical model of the failing mouse ventricular myocytes that could be used to interpret the observed experimental data. In this study, we developed a comprehensive, experimentally verified model of the failing mouse ventricular myocytes. It is specifically developed for the mathematical description of failing mouse ventricular myocytes data obtained after transverse aortic constriction, and those experimental data were used for model verification. As a basis, we used mathematical models of mouse ventricular myocytes developed previously (Bondarenko et al., 2004; Petkova-Kirova et al., 2012; Bondarenko, 2014; Rozier and Bondarenko, 2017). In the new model, we redesigned the cells geometry based on the experimental findings from the failing mouse ventricular myocytes, reformulated the set of outward K^+ currents by separating I_{Kur} into $I_{K,slow1}$ and $I_{K,slow2}$ due to their differential response to β-adrenergic stimulation, added late Na^+ current due to its possible important role in heart failure, and made several other model adjustments to fit the experimental data. The resulting model was able to generate, with high accuracy, the mouse's left ventricular AP, $[Ca^{2+}]_i$, and $[Na^+]_i$ dynamics and their frequency dependences under normal and diseased conditions. We also showed the differences in the AP, $[Ca^{2+}]_i$ transients, and Ca^{2+} and Na^+ fluxes in the models of normal and failing mouse ventricular myocytes. The model revealed the major players in the sarcoplasmic

reticulum Ca^{2+} load in failing ventricular myocytes. We also described a proarrhythmic behavior of Ca^{2+} dynamics upon stimulation with isoproterenol and mechanisms of the proarrhythmic behavior suppression. Finally, we performed a sensitivity analysis of the model.

2 A COMPARTMENTALIZED MATHEMATICAL MODEL OF MOUSE ATRIAL MYOCYTES

2.1 Materials and Methods

2.1.1 Model Development

Our mathematical model of mouse atrial myocytes is based on the previously published models of mouse ventricular myocytes (Bondarenko, 2014; Bondarenko, 2004; Petkova-Kirova et al., 2012; Rozier and Bondarenko, 2017). Recent experimental findings from mouse atria and other species revealed myocytes both with and without TATS (Brandenburg et al., 2018; Yue et al., 2017). Here, we developed a model for a subpopulation of right atrial myocytes with a developed transverse-axial tubule system. Our model assumptions are based on the comprehensive experimental study by Yue et al. (2017), who found that about 23% of atrial myocytes possessed TATS with a well-organized spacing of transverse tubules, similar to those in mouse ventricular myocytes. The authors also found that 162 out of 193 atrial myocytes (84%) contained identifiable TATS with varying degrees of TATS organization. In addition, Yue et al. (2017) have demonstrated "near-synchronous" Ca^{2+} transients in atrial myocytes (61 atrial cells, 6 mice), without significant differences between time-to-peaks of Ca^{2+} transient in the subsarcolemmal space, in the cell center, or the global (cellular) Ca^{2+} transient. Therefore in our modeling, we assumed that the Ca^{2+}-induced Ca^{2+} release mechanism for a subpopulation of mouse atrial myocytes with developed TATS, which represent somewhere between 23% and 84% of all mouse atrial myocytes, is similar to or close to that described for mouse ventricular myocytes.

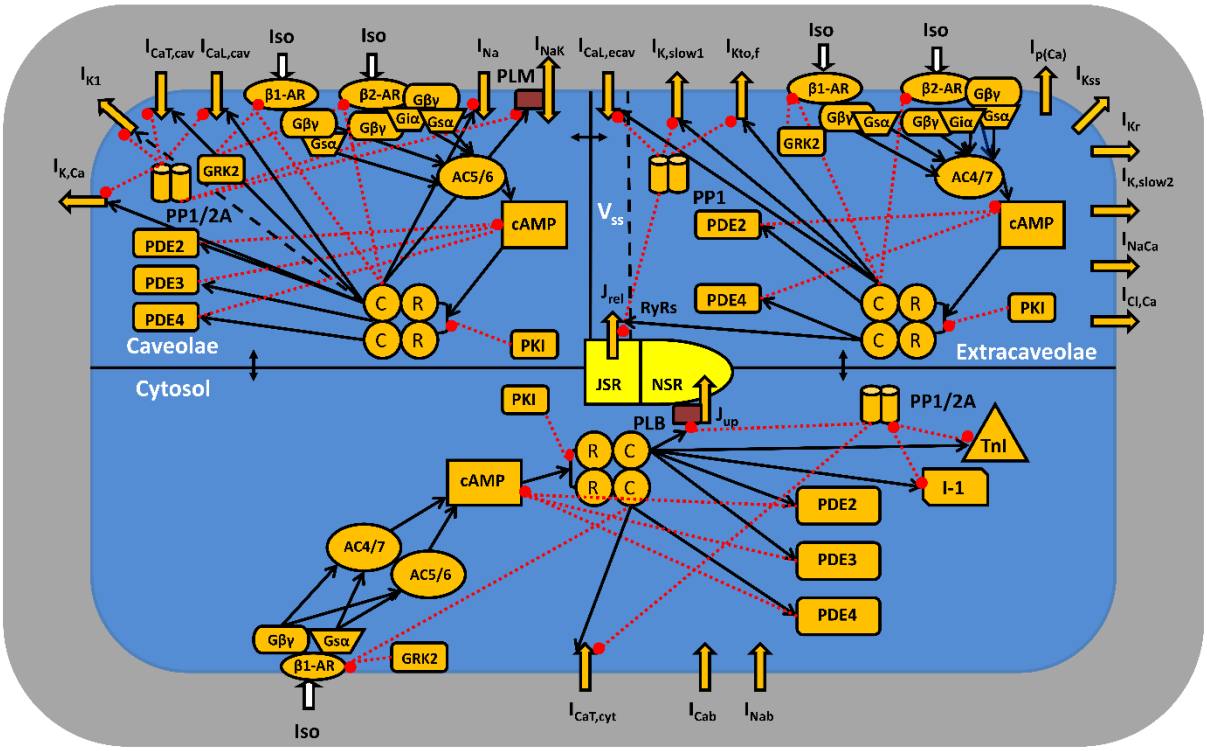

Figure 2.1 *A schematic representation of the mouse right atrial myocyte.*
The cell consists of three compartments (caveolae, extracaveolae, and cytosol) related to the combined β_1- and β_2-adrenergic signaling systems. The subspace volume (V_{ss}) is localized in the extracaveolar compartment. The biochemical portions of the combined β_1- and β_2-adrenergic signaling systems are the β_1-adrenergic receptors (β_1-AR), the β_2-adrenergic receptors (β_2-AR), the α-subunit of stimulatory G-protein ($G_{s\alpha}$), the α-subunit of inhibitory G-protein ($G_{i\alpha}$), the βγ-subunit of G_s and G_i ($G_{\beta\gamma}$), the adenylyl cyclases of type 5/6 or 4/7 (AC5/6 or AC4/7, respectively), the phosphodiesterases of type 2, 3, or 4 (PDE2, PDE3, or PDE4, respectively), the cyclic AMP (cAMP), regulatory (R) and catalytic (C) subunits of protein kinase A holoenzyme, the protein kinase A inhibitor (PKI), the G-protein-coupled receptor kinase of type 2 (GRK2), the protein phosphatases of type 1 and 2A (PP1 and PP2A, respectively), the inhibitor-1 (I-1). Targets of the combined β_1- and β_2-adrenergic signaling systems are in the caveolae (including the fast Na^+ current (I_{Na}), the L-type Ca^{2+} current ($I_{Ca,L,cav}$), the T-type Ca^{2+} current ($I_{Ca,T,cav}$), the small-conductance Ca^{2+}-activated K^+ current ($I_{Ca,K}$), the Na^+/K^+ pump (I_{NaK}), regulated by phospholemman (PLM), phosphodiesterases PDE2-PDE4, and the time-independent K^+ current (I_{K1})), the extracaveolae (including the L-type Ca^{2+} current ($I_{Ca,L,ecav}$), the rapidly recovering transient outward K^+ current ($I_{Kto,f}$), the rapidly activating, slowly inactivating K^+ current ($I_{K,slow1}$, encoded by Kv1.5; 4-AP-sensitive; also named as I_{Kur}, the ultra-rapidly activating delayed rectifier K^+ current), the rapidly activating, slowly inactivating K^+ current ($I_{K,slow2}$, encoded by K_v2.1; TEA-sensitive), ryanodine receptors (RyRs), and phosphodiesterases (PDE2, PDE4)), and cytosol (including the T-type Ca^{2+} current ($I_{CaT,cyt}$), phospholamban (PLB), troponin I (TnI), and phosphodiesterases PDE2-PDE4). Stimulatory links are shown by black arrows and inhibitory links are shown by red dashed lines with balls of effectors. Other transmembrane currents are the sarcolemmal Ca^{2+} pump ($I_{p(Ca)}$, also known as plasmalemmal Ca^{2+}-ATPase, PMCA), the Na^+/Ca^{2+}

exchanger (I_{NaCa}), the rapid delayed rectifier K^+ current (I_{Kr}), the non-inactivating steady-state voltage-activated K^+ current (I_{Kss}), and the Ca^{2+} and Na^+ background currents (I_{Cab} and I_{Nab}), which are not affected by the combined β_1- and β_2-adrenergic signaling systems. The Ca^{2+} fluxes are uptake of Ca^{2+} from the cytosol to the network sarcoplasmic reticulum (NSR) (J_{up}) by the SERCA pump and Ca^{2+} release from the junctional sarcoplasmic reticulum (JSR) (J_{rel}) through the RyRs. $[Ca^{2+}]_i$, $[Na^+]_i$, and $[K^+]_i$ are the intracellular Ca^{2+}, Na^+, and K^+ concentrations in the caveolae, extracaveolae, and cytosol; $[Ca^{2+}]_o$, $[Na^+]_o$, and $[K^+]_o$ are the extracellular Ca^{2+}, Na^+, and K^+ concentrations. Modified from (Bondarenko, 2014).

We also made several principal changes in our mouse ventricular myocyte model to ensure that the new model gives a comprehensive description of mouse atrial electrophysiology, which is currently unavailable. We changed the cell geometry and added two major ionic currents: T-type Ca^{2+} current, $I_{Ca,T}$, and small-conductance Ca^{2+}-activated K^+ current, $I_{K,Ca}$. The magnitude of the rapid delayed rectifier current, I_{Kr}, was increased by a factor of 10 as compared to the mouse ventricular myocyte, according to the experimental data by Nakamura et al. (2010). However, there was no marked contribution to the AP shape in simulations, as it was also observed in Vaidyanathan et al. (2013). We also changed the formulation of the time-independent K^+ current, I_{K1}, to fit the experimental data from mouse atrial myocytes. The ultra-rapidly activating K^+ current, I_{Kur}, was reformulated to include two components, $I_{K,slow1}$ (encoded by $K_v1.5$ channels and also referred to as I_{Kur} component) and $I_{K,slow2}$ (encoded by $K_v2.1$ channels) that demonstrate different responses to the activation of β_1- and β_2-adrenergic signaling systems (Kodirov et al., 2004; Wilson et al., 1994; Zhou et al., 2003; Zhou et al., 2012). The magnitudes of the L-type Ca^{2+} current, $I_{Ca,L}$, and several K^+ currents, were changed to fit the experimental values obtained from mouse atrial myocyte. The following differential equation describes the resulting model's action potential:

$$\frac{dV}{dt} = -\frac{1}{C_m}(I_{CaL} + I_{CaT} + I_{p(Ca)} + I_{NaCa} + I_{Cab} + I_{Na} + I_{Nab} + I_{NaK} + I_{Kto,f} + I_{K1} + I_{K,slow1} + I_{K,slow2} + I_{Kss} + I_{K,Ca} + I_{Kr} + I_{Cl,Ca} - I_{stim}),$$

where I_{CaL} is the L-type Ca^{2+} current, I_{CaT} is the T-type Ca^{2+} current, $I_{p(Ca)}$ is the sarcolemmal Ca^{2+} pump, I_{NaCa} is the current from the Na^+/Ca^{2+} exchanger, I_{Cab} is the Ca^{2+} background current, I_{Na} is the fast Na^+ current, I_{Nab} is the Na^+ background current, I_{NaK} is the current of the Na^+-K^+ pump, $I_{Kto,f}$ is the rapidly recovering transient outward K^+ current, I_{K1} is the time-independent K^+ current, $I_{K,slow1}$ is the rapidly activating, slowly inactivating K^+ current (encoded by $K_v1.5$; 4-aminopyridine-sensitive; also named as I_{Kur}, the ultra-rapidly activating delayed rectifier K^+ current), $I_{K,slow2}$ is the rapidly activating, slowly inactivating K^+ current (encoded by $K_v2.1$; TEA-sensitive), I_{Kss} is the noninactivating steady-state voltage-activated K^+ current, $I_{K,Ca}$ is the small-conductance Ca^{2+}-activated K^+ current, I_{Kr} is the rapid delayed rectifier K^+ current, $I_{Cl,Ca}$ is the Ca^{2+}-activated chloride current, and I_{stim} is the stimulus current.

2.1.2 Cell Geometry and Cell Compartments

Structurally, mouse atrial myocytes differ from ventricular myocytes by the cell size and the volume of subcellular compartments. To deal with these differences, the atrial myocyte's length and diameter were set to 110 μm and 16 μm, respectively, according to the experimental data by Brandenburg et al. (2016), which resulted in cell volume of $V_{cell} = 22.1200\times10^{-6}$ μl. The geometric surface area of atrial myocytes was calculated to be equal to 0.5931×10^{-4} cm^2, and it was the same as their capacitive surface area, in contrast to ventricular myocytes, where capacitive surface area is about 40-50% larger than their geometric surface area (Giles et al., 1988; Hume et al., 1985).

Mouse atrial myocytes also show different sizes of intracellular compartments as a percentage of the total cell volume compared to ventricular myocytes (Forbes et al., 1990). Mitochondria and the sarcoplasmic reticulum (SR) occupy V_{mito} = 24.73±0.61% and V_{SR} = 12.15±0.44% of the right atrial myocytes, respectively, leaving the myoplasm volume of 63.12%

(or $V_{myo} = 13.9600\times10^{-6}$ µl). The network SR and junctional SR constitute 11.54% and 0.61% of the cell volume, respectively, yielding $V_{NSR} = 2.5523\times10^{-6}$ µl and $V_{JSR} = 0.1349\times10^{-6}$ µl. We used these data for our model cell.

To minimize the number of intracellular compartments without losing significant functionality of the model, we introduced three major compartments: caveolae (cav), extracaveolae (ecav), and cytosol (cyt) (Fig. 2.1). The caveolar compartment represents the subsarcolemmal space associated with caveolae microdomains, which represents the cholesterol-rich invaginations of the plasma membrane and includes caveolin-3 scaffolding protein. The extracaveolar compartment represents the subsarcolemmal space associated with cholesterol-rich lipid rafts that do not include caveolin-3. The cytosolic compartment represents the bulk cytoplasmic compartment associated with the remaining cell membrane (Agarwal et al., 2018; Iancu et al., 2007). In our model, TATS is considered as part of the sarcolemma with the presence of the three compartments mentioned above.

The ionic currents are distributed among different compartments, as found experimentally (see (Bondarenko et al., 2004) and references therein for details). The caveolar compartment contains a fraction of the L-type ($I_{CaL,cav}$) and the T-type ($I_{CaT,cav}$) Ca^{2+} currents, the fast Na^+ current (I_{Na}), the small-conductance Ca^{2+}-activated K^+ current ($I_{K,Ca}$), the current of the Na^+-K^+ pump (I_{NaK}), and the time-independent K^+ current (I_{K1}). The extracaveolar compartment includes a fraction of the L-type Ca^{2+} current ($I_{CaL,ecav}$), the rapidly recovering transient outward K^+ current ($I_{Kto,f}$), the rapidly activating, slowly inactivating K^+ current ($I_{K,slow1}$, encoded by $K_v1.5$; 4-aminopyridine-sensitive), the rapidly activating, slowly inactivating K^+ current ($I_{K,slow2}$, encoded by $K_v2.1$; TEA-sensitive), the noninactivating steady-state voltage-activated K^+ current (I_{Kss}), the rapid delayed rectifier K^+ current (I_{Kr}), the sarcolemmal Ca^{2+} pump ($I_{p(Ca)}$), the current form the

Na^+/Ca^{2+} exchanger (I_{NaCa}), and the Ca^{2+}-activated chloride current ($I_{Cl,Ca}$). Finally, the cytosolic compartment contains a fraction of the T-type Ca^{2+} current ($I_{CaT,cyt}$), the Ca^{2+} background current (I_{Cab}), and the Na^+ background current (I_{Nab}).

The model also describes compartmentalized Ca^{2+} dynamics, including local control of Ca^{2+}-induced Ca^{2+} release (Fig. 2.1). Ca^{2+} ions that enter through the extracaveolar fraction of L-type Ca^{2+} channels are localized within the subspace volume (V_{ss}, also called "dyadic space") and cause Ca^{2+} release from the junctional sarcoplasmic reticulum (JSR). Then Ca^{2+} ions from V_{ss} diffuse to the rest of the cell volume, formatting a raising part of intracellular $[Ca^{2+}]_i$ transient. Ca^{2+} ions are pumped back to the network sarcoplasmic reticulum (NSR) by the SERCA pump (J_{up}) and extruded outside of the cell by the Na^+/Ca^{2+} exchanger and the sarcolemmal Ca^{2+} pump, resulting in a decline of $[Ca^{2+}]_i$ transient.

2.1.3 T-type Ca^{2+} Current

In contrast to ventricular myocytes, Mouse atrial myocytes possess significant $I_{Ca,T}$ (Curran et al., 2015). Its maximum magnitude reaches –0.56±0.11 pA/pF (Curran et al., 2015), which makes a small, but a noticeable contribution to the total Ca^{2+} entry to the cell in addition to $I_{Ca,L}$ (magnitude is ~2 pA/pF (Curran et al., 2015; Lomax et al., 2003). It has been shown that $Ca_v3.1$ and $Ca_v3.2$ channel proteins that represent the molecular basis for $I_{Ca,T}$, are co-localized with caveolar scaffolding protein caveolin-3, suggesting their possible localization in the caveolae compartment (Markandeya et al., 2011). On the other hand, the overexpression of the ion channels responsible for $I_{Ca,T}$ demonstrated their localization in both caveolar (68%) and t-tubules (32%) compartments (Jaleel et al., 2008). Jaleel et al. (2008) have also shown that even a larger Ca^{2+} entry produced by $I_{Ca,T}$ in mouse ventricular myocytes overexpressing $Ca_v3.1$, resulted in a much

smaller Ca^{2+} release from the SR, suggesting their primary localization outside the dyadic space in the cytosolic compartment. This observation is in line with the experimental data by Sipido et al. (1998), who have demonstrated a small contribution of $I_{Ca,T}$ to the SR Ca^{2+} release in guinea pig ventricular myocytes.

For our mouse atrial myocyte model, we adopted a Markov model of the T-type Ca^{2+} channel developed by Serrano et al. (1999). The model consists of five closed states (C_0-C_4), five closed-inactivated states (I_0-I_4), an open state O, and an open-inactivated state I_O (Fig. 2.2A). This model reflects the independent activation of four-channel subunits, where 0 to 4 subunits are activated in C_0 to C_4 states, respectively. The forward and backward rate constants (k_{CaTpv} and k_{CaTmv}) and the backward rate constant k_{CaTmo} from open state O to closed state C_4 are voltage-dependent. Forward rate constant k_{CaTpo} is rate-limiting and voltage-independent. Inactivated states are allosterically coupled to both the closed states C_0-C_4 and the open state O. Two allosteric factors f_{CaT} and h_{CaT} regulate the coupling of the inactivated states to the closed states (Serrano et al., 1999). Several rate constants were modified from the Serrano et al. (1999) model to fit the experimental data on $I_{Ca,T}$ (See Appendix A1). Unlike the L-type Ca^{2+} channels, in which inactivation is both Ca^{2+}- and voltage-dependent, $I_{Ca,T}$ inactivation depends only on transmembrane voltage (Vassort et al., 2006).

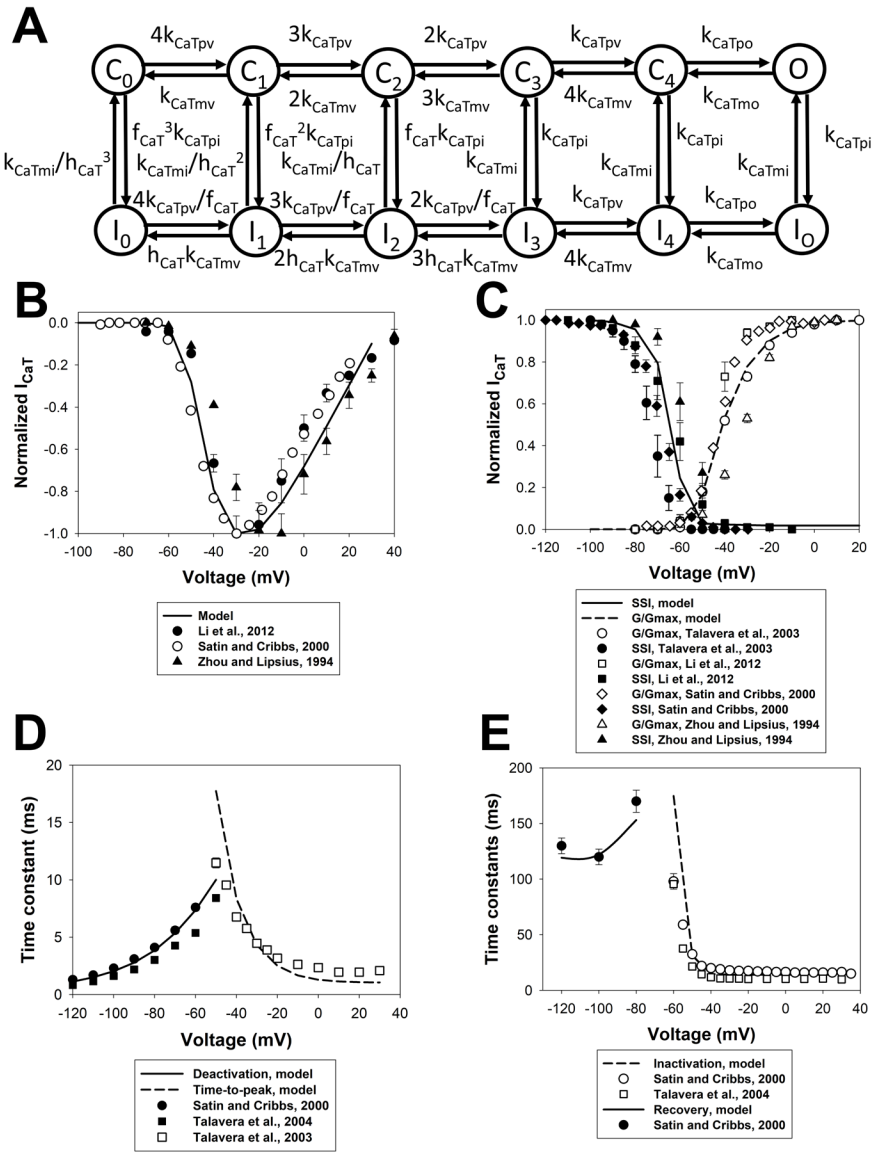

Figure 2.2 *The T-type Ca^{2+} channel's Markov model and current kinetics.*
(A) *The model consists of five closed states (C_0-C_4), five closed-inactivated states (I_0-I_4), an open state O, and open-inactivated state I_O. Transition rates k_{CaTpv}, k_{CaTmv}, and k_{CaTmo} are voltage-dependent.* ***(B)*** *Current-voltage dependences (I-V) for I_{CaT}. Simulation data are shown by a solid black line. Experimental data by Li et al. (2012), Satin and Cribbs (2000), and Zhou and Lipsius (1994) are shown by filled circles, unfilled circles, and filled triangles, respectively.* ***(C)*** *Steady-state inactivation relationships (SSI) and G/G_{max} of I_{CaT}. Simulation data for SSI and G/G_{max} are shown by solid and dashed lines, respectively. Experimental data on SSI by Talavera et al. (2003), Li et al. (2012), Satin and Cribbs (2000), and Zhou and Lipsius (1994) are shown by filled circles, squares, diamonds, and triangles, respectively. Experimental data on G/G_{max} by Talavera et al. (2003), Li et al. (2012), Satin and Cribbs (2000), and Zhou and Lipsius (1994) are shown by*

unfilled circles, squares, diamonds, and triangles, respectively. In (B) and (C), simulation data were obtained by two-pulse protocol: a 500 ms pulses P1 from –100 to +30 mV applied from the holding potential –100 mV in 10-mV steps and followed by a second pulse P2 to –20 mV for 100 ms. ***(D)*** *Deactivation kinetics and time-to-peak currents of $I_{Ca,T}$. Simulation data for deactivation time constant and time-to-peak currents are shown by solid and dashed lines, respectively. Experimental data for deactivation kinetics were obtained by Satin and Cribbs (2000) (filled circles) and Talavera et al. (2004) (filled squares). Experimental data on time-to-peak current were obtained by Talavera et al. (2003) (unfilled squares). For simulation of time-to-peak current, we used the same protocol as in (B) and (C). Simulation data on the deactivation time constant were obtained by the following two-pulse protocol: the pulse P1 was set to –20 mV for 3 ms and followed by a second pulse that ranged between –120 and –50 mV for 200 ms in steps of 10 mV (holding potential was –100 mV). (E) Inactivation and recovery from inactivation kinetics for $I_{Ca,T}$. Simulation data for inactivation and recovery time constants are shown by dashed and solid lines, respectively. Experimental data on inactivation kinetics by Satin and Cribbs (2000) and Talavera et al. (2004) are shown by unfilled circles and squares, respectively. Experimental data on recovery from inactivation kinetics by Satin and Cribbs (2000) are shown by filled circles. Inactivation kinetics were obtained by the same voltage-clamp protocol as in (B) and (C). Recovery from inactivation kinetics was obtained from a two-pulse protocol: pulses to 0 mV (P1) for 1000 ms from holding potential –100 mV were followed by a second 100-ms depolarization (P2) to 0 mV with a variable time gap. Interpulse voltage varied from –120 to –80 mV.*

Simulation and experimental properties of $I_{Ca,T}$ under different experimental protocols are shown in Fig. 2.2, B-E. The model properly describes current-voltage relationships (I-V) (Fig. 2.2B), steady-state inactivation relationships and G/Gmax (Fig. 2.2C), time-to-peak current and deactivation kinetics (Fig. 2.2D), as well as inactivation and recovery from inactivation kinetics (Fig. 2.2E). The simulated maximum magnitude of $I_{Ca,T}$ = –0.56 pA/pF, which is equal to the experimental value of –0.56±0.11 pA/pF (Curran et al., 2015). In our model, we also implemented the effects of β-adrenergic stimulation of $I_{Ca,T}$. Figure 2.3A shows the experimental time course of the magnitude of $I_{Ca,T}$ upon the application of 1 μM isoproterenol reported by Li et al. (2012). Similar time behavior was obtained from our simulations, where dotted, dashed, and solid lines plot time courses of phosphorylated fractions of caveolar $I_{Ca,T}$ ($I_{CaT,cav}$), tubular $I_{Ca,T}$ ($I_{CaT,cyt}$), and averaged phosphorylated fraction of the cellular $I_{Ca,T}$. Our model was able to reproduce the magnitude of increase of $I_{Ca,T}$ upon 10-minute exposure to 1 μM isoproterenol obtained experimentally by Li et al. (2012), as shown in Fig. 2.3B.

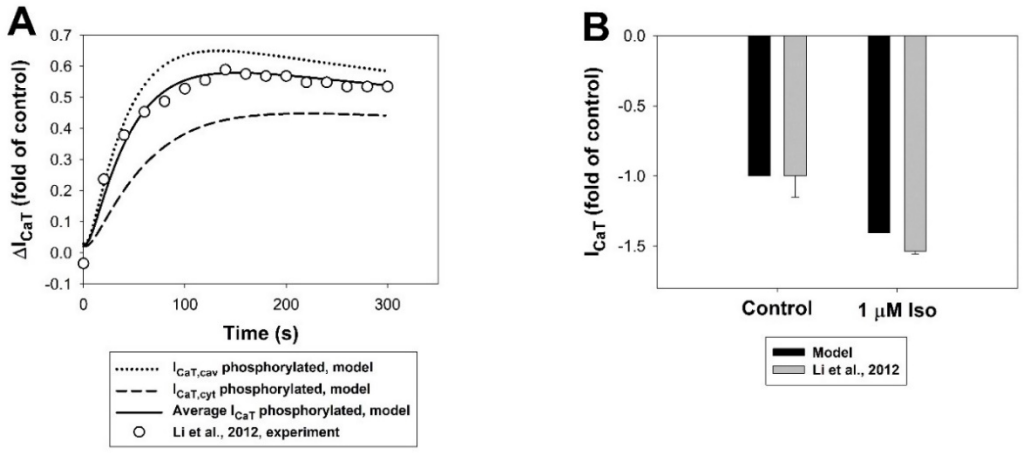

Figure 2.3 *The effects of isoproterenol on T-type Ca^{2+} current (I_{CaT}).*
*(**A**) Simulated time courses of the phosphorylated fraction of $I_{Ca,T,cav}$ and $I_{Ca,T,cyt}$, as well as averaged phosphorylated fraction of $I_{Ca,T}$, are shown by dotted, dashed, and solid lines, respectively, in response to the application of 1 μM isoproterenol. The experimental time course of $I_{Ca,T}$ increase upon stimulation with 1 μM isoproterenol obtained by Li et al. (2012) is shown by unfilled circles. (**B**)Simulated and experimental data (obtained by Li et al. (2012)) on $I_{Ca,T}$ magnitude in control and after 10 minutes exposure to 1 μM isoproterenol are shown by black and gray bars, respectively.*

2.1.4 Small-Conductance Ca^{2+}-Activated K^+ Current

Mouse atrial myocytes are shown to express the small-conductance Ca^{2+}-activated K^+ current, $I_{K,Ca}$, which may contribute to AP shape (Li et al., 2009). This current is activated by intracellular Ca^{2+}, and most of its gating characteristics are voltage-independent (Hirschberg et al., 1998). Experimental data by Zhang et al. (2018) demonstrated that the small-conductance Ca^{2+}-activated K^+ channels are localized quite close to one fraction of the L-type Ca^{2+} channels, at a distance of ~100 nm, which we assume belong to the caveolar compartment. However, they are relatively far from the second fraction of the L-type Ca^{2+} channels, at a distance of ~400-500 nm, which we assume are in the extracaveolar compartment. Similarly, the surface small-conductance Ca^{2+}-activated K^+ channels are localized relatively far from the ryanodine receptors, at distances of ~400 nm, which are in the extracaveolar compartment. We thus can suggest that the small-conductance Ca^{2+}-activated K^+ channels are localized outside of the dyadic space of cardiac

myocytes. In addition, half-activation Ca^{2+} concentration for $I_{K,Ca}$ is around 0.23-0.74 μM Ca^{2+} (Hirschberg et al., 1998; Kennedy et al., 2017), which is much smaller than the Ca^{2+} concentration in dyadic space (tens of μM). To get a gradual response from $I_{K,Ca,}$, the corresponding channels have to be localized quite far from the dyadic space, where the Ca^{2+} concentration declines to less than 1 μM. Further, experimental data demonstrated that the small-conductance Ca^{2+}-activated K^+ channels colocalize with caveolin-1 in different cell types (Balut et al., 2012), and caveolin-1 and caveolin-3 may colocalize in mouse and rat atrial myocytes (Volonte et al., 2008). These experimental facts suggest a possible localization of the small-conductance Ca^{2+}-activated K^+ channels in the caveolae compartment, which, therefore, was implemented in our mathematical model of mouse atrial myocytes.

We employed the Hirschberg et al. (1998) mathematical model of the $I_{K,Ca}$, with several adjustments to fit the experimental data (Fig. 2.4A). The model consists of four closed states (C_1-C_4) and two open states (O_1 and O_2). Forward rate constants (k_{KCaf1}, k_{KCaf2}, and k_{KCaf3}) are Ca^{2+}-dependent, and the other rate constants are voltage- and Ca^{2+}-independent. $I_{K,Ca}$ current is defined by the equation:

$$I_{K,Ca} = g_{K,Ca}(V)(O_1 + O_2),$$

where O_1 and O_2 are the probabilities of finding a channel in open states, $g_{K,Ca}(V)$ is a third-order polynomial function (see Appendix A2).

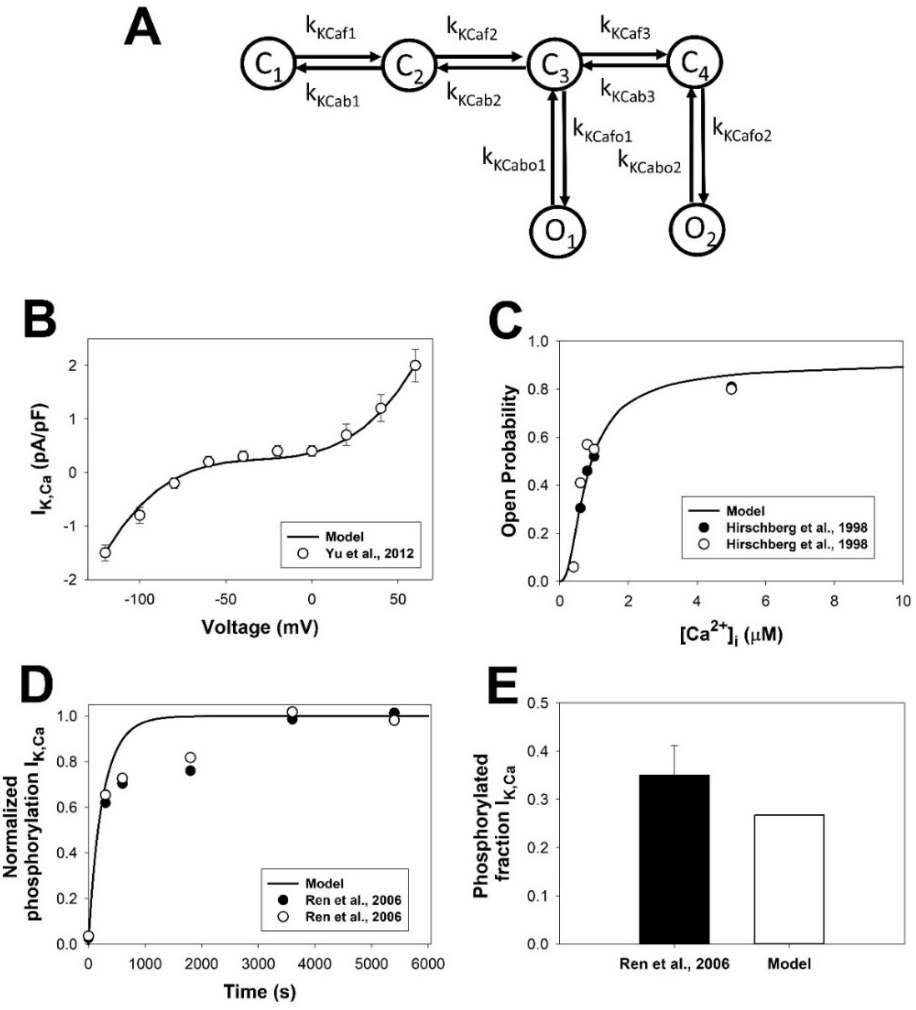

Figure 2.4 *Small-conductance Ca^{2+}-activated K^+ current.*
(A) *Markov model of the small-conductance Ca^{2+}-activated K^+ current ($I_{K,Ca}$). The model consists of four closed states (C_1-C_4) and two open states (O_1 and O_2). Forward rate constants (k_{KCaf1}, k_{KCaf2}, and k_{KCaf3}) are Ca^{2+}-dependent, and the other rate constants are constant.* ***(B)*** *$I_{K,Ca}$ as a function of voltage at $[Ca^{2+}]_i$ = 0.9 μM. Simulation data are shown by a solid line; experimental data by Yu et al. (2012) are shown by unfilled circles. (C) Open probability of the small-conductance Ca^{2+}-activated K^+ channel as a function of $[Ca^{2+}]_i$. Simulation data are shown by a solid line; experimental data by Hirschberg et al. (1998) are shown by filled and unfilled circles.* ***(D)*** *Time course of the small-conductance Ca^{2+}-activated K^+ channel phosphorylation at relatively low concentrations of PKA catalytic subunit (0.032184 μM). Simulation data are shown by a solid line; experimental data by Ren et al. (2006) are shown by filled and unfilled circles.* ***(E)*** *Phosphorylated fraction of the small-conductance Ca^{2+}-activated K^+ channels. Experimental data by Ren et al. (2006) are obtained with 50 μM forskolin together with 100 μM of phosphodiesterase inhibitor Ro-201724. Simulation data are obtained at the maximal concentrations of the catalytic subunits of PKA.*

The simulated current-voltage relationships for $I_{K,Ca}$ are shown in Fig. 2.4B by a solid line. Simulation fits well with the experimental data from mouse atrial myocytes obtained by Yu et al. (2012). $I_{K,Ca}$ current is virtually absent during diastole and is activated by Ca^{2+} entry into the cell during systole. The simulated channel's open probability as a function of intracellular Ca^{2+} is shown in Fig. 2.4C. Symbols plot corresponding experimental data from Hirschberg et al. (1998). It is seen that the half-activation Ca^{2+} concentration for $I_{K,Ca}$ is within the range from 0.2 to 1.0 μM Ca^{2+}, suggesting the current activation by intracellular $[Ca^{2+}]_i$ transients.

The small-conductance Ca^{2+}-activated K^+ channels can be stimulated by both β_1- and β_2-adrenergic signaling systems via the channels' phosphorylation. When phosphorylated, the channels are removed from the membrane and do not participate in the conduction of trans-sarcolemmal current. Simulated and experimental time courses of the phosphorylation of the small-conductance Ca^{2+}-activated K^+ channel at relatively weak stimulation with 0.032184 μM of the catalytic subunit of protein kinase A (PKA) are shown in Fig. 2.4D. It took about 1 hour to obtain a saturation level of phosphorylation, which is relatively small, fractions of a percent. Stronger stimulation by 50 μM forskolin (a non-specific stimulator of adenylyl cyclases) in the presence of 100 μM phosphodiesterase inhibitor Ro-201724 produced a significant effect by removing ~35% of the channel from the surface within 10 minutes (Ren et al., 2006). We also simulated this intervention by the maximum activation of PKA in our model, which resulted in a 26.7% phosphorylation level after 10-minute stimulation, which is close to the experimental finding by Ren et al. (2006).

2.1.5 Other Model Adjustments

First, experimental data shows a significantly smaller density of $I_{Ca,L}$ in mouse atrial myocytes as compared to ventricular myocytes. Therefore, we reduced $I_{Ca,L}$ conductance by a

factor of 3.35 to fit the experimental data by Lomax et al. (2003). Second, the magnitude of the fast-recovering transient outward K^+ current $I_{Kto,f}$ was decreased by a factor ~2.73 from that in the ventricular myocyte model as observed experimentally (Bao et al., 2016; Bondarenko, 2004; Lomax et al., 2003; Petkova-Kirova et al., 2012).

Third, we modified the description of the ultra-rapidly activating K^+ current, I_{Kur}, also called the rapidly activating, slowly inactivating K^+ current ($I_{K,slow}$). In the mathematical model by Bondarenko et al. (2004) and Bondarenko (2014), I_{Kur} includes K^+ currents carried by both $K_v1.5$ and $K_v2.1$ ion channels, which have a different response to β-adrenergic stimulation. An experimental study by Li et al. (1996) demonstrated a 35% increase in I_{Kur} in human atrial myocytes upon stimulation with 1 μM isoproterenol. Additional experiments with an application of 200 μM of 4-aminopyridine, a $K_v1.5$ inhibitor, with and without 1 μM isoproterenol, have shown that the predominant portion of I_{Kur} in the human atria is $K_v1.5$ channels. This finding is also supported by the experimental data on the expression of $K_v1.5$ and $K_v2.1$ in the human atria, where the expression level of $K_v2.1$ is about 1% of $K_v1.5$ (Gaborit et al., 2007). Electrophysiological recordings also show that the magnitude of the remaining component of I_{Kur} in the human atria is about ~15% (Brandt et al., 2000). In mice, K^+ currents encoded by both $K_v1.5$ and $K_v2.1$ have approximately equal magnitudes (Kodirov et al., 2004; London et al., 2001). The effect of PKA on $K_v2.1$ is quite small, as it was shown experimentally (Wilson et al., 1994; Zhou et al., 2012). Therefore, we included two currents: the rapidly activating, slowly inactivating K^+ current, $I_{K,slow1}$ (encoded by $K_v1.5$; 4-aminopyridine-sensitive; also named as I_{Kur}), and the rapidly activating, slowly inactivating K^+ current, $I_{K,slow2}$ (encoded by $K_v2.1$; TEA-sensitive) (Fig. 2.5A). Only $I_{K,slow1}$ is affected by isoproterenol in our mathematical model. The magnitude of $I_{K,slow1}$ plus

$I_{K,slow2}$ was decreased by a factor of 3, based on the data by Xu et al. (1999), which show that $I_{K,slow}$ ($I_{K,slow1}$ plus $I_{K,slow2}$) in mouse ventricular myocytes is by a factor 3 smaller than in atrial myocytes.

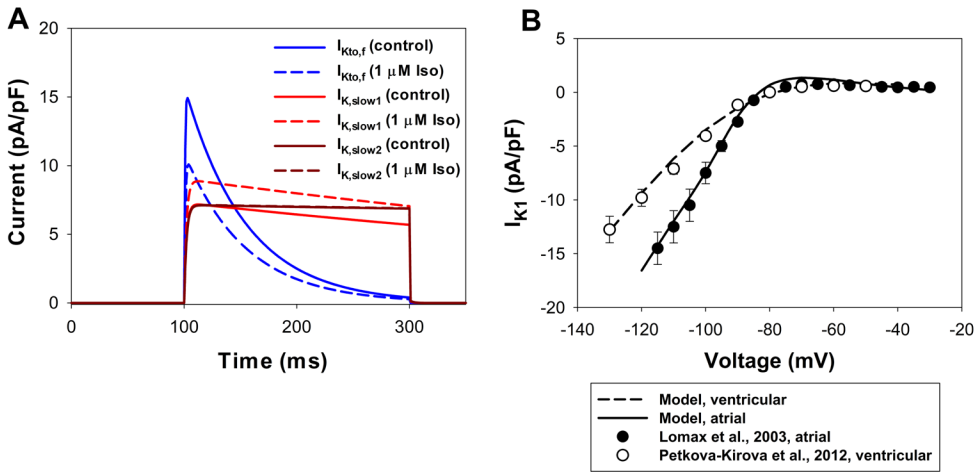

Figure 2.5 *Current traces for K currents and current-voltage relationships for the time-independent K^+ current (I_{K1}).*
(A) *Current traces of $I_{Kto,f}$, IK,slow1, and $I_{K,slow2}$ elicited by a 200-ms depolarization pulse to +40 mV applied to mouse atrial myocytes from the holding potential –80 mV at 100 ms. Simulations for control and after 10-minute exposure to 1 μM isoproterenol are shown by solid and dashed lines, respectively.* ***(B)*** *Current-voltage relationships for the time-independent K^+ current I_{K1} in mouse atrial and ventricular myocytes. Solid and dashed lines show simulated data for I_{K1} for atrial and ventricular myocytes, respectively. Experimental data for atrial (Lomax et al., 2003) and ventricular (Petkova-Kirova et al., 2012) are plotted by filled and unfilled circles, respectively.*

Forth, in the atrial myocyte model, the magnitude of the non-inactivating steady-state K^+ current I_{Kss} was reduced by about 43% from that in the ventricular myocyte model (Xu et al., 1999). In addition, since mouse atrial myocytes possess a relatively large rapid delayed rectifier current, in our model, it was increased accordingly by a factor of 10 as in the ventricular myocyte model (Bondarenko et al., 2004; Nakamura et al., 2010). Finally, we increased the maximum conductance of the time-independent K^+ current I_{K1} by a factor of 1.7 to fit the experimental data for mouse right atrial myocytes by Lomax et al. (2003) (Fig. 2.5B). We also plotted the data on I_{K1}

obtained from mouse ventricular myocytes (Petkova-Kirova et al., 2012) (Fig. 2.5B) for comparison.

We also have made the required adjustments to the Ca^{2+} handling. Experimental data shows that the SR volume and SR Ca^{2+} concentration are larger in mouse atrial versus ventricular myocytes. In particular, the SR Ca^{2+} concentration is twice larger in atrial cells (Brandenburg et al., 2016). In addition, the Ca^{2+} entry through the L- and T-type Ca^{2+} channels in atrial cells is by a factor ~3 smaller than that in ventricular cells due to the relatively small current magnitudes (Bondarenko, 2014; Lomax et al., 2003). This requires a reduction of the Na^+/Ca^{2+} exchanger and Na^+/K^+ pump function in atrial cells. Experimental data from human hearts shows that Na^+/K^+ pump activity in the atrium is ~ 50% of the ventricular activity, and the abundance of Na^+/K^+-ATPase in the atrium is ~65-70% of the ventricular expression in the human and guinea pig hearts (McDonald et al., 2000; Wang et al., 1996). Therefore, we multiplied ventricular $I_{NaK}^{\max}$ by a factor of 0.5. However, the experimental data on the expression of the Na^+/Ca^{2+} exchanger in mouse atrial vs. ventricular myocytes shows similar levels (Groenke et al., 2013), so we did not change the magnitude of k_{NaCa} in the atrial myocyte model. We also reduced the amount of calsequestrin in the atrial cell by 40% of the ventricular value, increased the SR Ca^{2+} maximum pumping rate by 2-fold, and reduced the half-saturation constant for the SR Ca^{2+} pump by a factor of 0.9 to account for a smaller amount of phospholamban, according to Lüss et al. (1999). Several other adjustments were made to obtain proper equilibrium intracellular Ca^{2+}, Na^+, and K^+ concentrations (see Appendix A and Table 2.1).

Table 2.1 *Differences between the model of mouse atrial myocytes presented in this paper and the model of mouse ventricular myocytes.*

Parameter	Definition	Ventricular cell model (6,79)	Atrial cell model
A_{cap}	Capacitive membrane area	1.5340×10^{-4} cm^2	0.5931×10^{-4} cm^2
V^{cell}	Cell volume	38.00×10^{-6} µl	22.12×10^{-6} µl
V^{cyt}	Cytosolic volume	25.84×10^{-6} µl	13.96×10^{-6} µl
V_{JSR}	Junctional SR volume	0.1200×10^{-6} µl	0.1349×10^{-6} µl
V_{NSR}	Network SR volume	2.098×10^{-6} µl	2.5523×10^{-6} µl
V_{ss}	Subspace volume	1.485×10^{-9} µl	2.970×10^{-9} µl
$I_{CaL,max}$	Normalization constant for the L-type Ca^{2+} current	7.0 pA/pF	2.0 pA/pF
v_1	Maximum RyR channel Ca^{2+} permeability	4,500 s^{-1}	405 s^{-1}
v_2	Ca^{2+} leak rate constant from the NSR	0.01740 s^{-1}	0.05220 s^{-1}
v_3	SR Ca^{2+}-ATPase maximum pump rate	3.0600×10^{-4} µMs^{-1}	8.0478×10^{-4} µMs^{-1}
$K_{m,up}^{np}$	Half-saturation constant for SR Ca^{2+}-ATPase pump (non-phosphorylated)	0.41 µM	0.3097 µM
$K_{m,up}^{p}$	Half-saturation constant for SR Ca^{2+}-ATPase pump (phosphorylated)	0.31 µM	0.20375 µM
τ_{xfer}	Time constant for transfer from subspace to myoplasm	0.0080 s	0.0104 s
G_{CaL}	Specific maximum conductivity for L-type Ca^{2+} channel (non-phosphorylated)	0.3772 mS/µF	0.1127 mS/µF
G_{CaLp}	Specific maximum conductivity for L-type Ca^{2+} channel (phosphorylated)	0.7875 mS/µF	0.2351 mS/µF
$[CSQN]_{tot}$	Total junctional SR calsequestrin concentration	15,000 µM	9,000 µM
I_{NaK}^{max}	Maximum Na^+/K^+ pump current	4.0 pA/pF	2.0 pA/pF

$I_{p(Ca)}^{max}$	Maximum Ca^{2+} pump current	0.051 pA/pF	0.153 pA/pF
G_{Cab}	Maximum background Ca^{2+} current conductance	0.000284 mS/µF	0.000213 mS/µF
$G_{Kto,f}$	Maximum conductance for the rapidly inactivating transient outward K^+ current (non-phosphorylated)	0.3846 mS/µF	0.14067 mS/µF
$G_{Kto,fp}$	Maximum conductance for the rapidly inactivating transient outward K^+ current (phosphorylated)	0.3846 mS/µF	0.086231 mS/µF
$G_{K,slow1}$	Maximum conductance for the rapidly activating, slowly inactivating K^+ current (encoded by $K_v1.5$, non-phosphorylated)	0.3424 mS/µF	0.05766 mS/µF
$G_{K,slow1p}$	Maximum conductance for the rapidly activating, slowly inactivating K^+ current (encoded by $K_v1.5$, phosphorylated)	0.53307 mS/µF	0.07496 mS/µF
$G_{K,slow2}$	Maximum conductance for the rapidly activating, slowly inactivating K^+ current (encoded by $K_v2.1$, non-phosphorylated)	Current absent	0.05766 mS/µF
G_{Kss}	Maximum conductance for the noninactivating steady-state K^+ current	0.0611 mS/µF	0.0428 mS/µF
G_{Kr}	Maximum conductance for the rapid delayed-rectifier K^+ current	0.078 mS/µF	0.780 mS/µF
G_{K1}	Maximum conductance for the time-independent K^+ current	0.27 mS/µF	0.459 mS/µF

2.1.6 β_1- and β_2-Adrenergic Signaling Systems

Experimental data shows that the level of the expression and the ratio of β_1- and β_2-adrenergic receptors in atrial cells is quite similar to those reported in ventricular myocytes (Brodde, 1991). Similar expressions were observed in atrial and ventricular myocytes for adenylyl cyclases (Brandenburg et al., 2016) and phosphodiesterases (Hua et al., 2012). Therefore, we used

the same model for β_1- and β_2-adrenergic signaling systems as for ventricular cells (Rozier & Bondarenko, 2017).

2.1.7 Simulation Methods

The model equations were solved by a fourth-order Runge-Kutta method, with two different time steps. A relatively small time step of 0.000002 ms was used during a 15-millisecond interval after the initiation of the stimulus current; for all other times, we used the time step 0.0001 ms. The cellular behavior was simulated without electrical stimulation with a time step of 0.1 ms. The model equations were implemented in FORTRAN 90. All simulations were performed on a single processor under SUSE Linux 11 on a Dell Precision Workstation T3500 with a six-core Intel Xeon CPU W3670 (3.2 GHz, 12 GB RAM). The model was developed for a room temperature of 25ºC (T = 298ºK). Initial conditions were obtained by running the program code without electrical stimulations for about 10,000 seconds to ensure quasi-steady-state. APs and $[Ca^{2+}]_i$ transients were initiated by a stimulus current (I_{stim} = 80 pA/pF, τ_{stim} = 1 ms) with the frequency 1 Hz (electrical stimulation).

2.2 Results

2.2.1 Mouse Atrial Action Potential and Ionic Currents

Experimental data shows that the APs in mouse atrial and ventricular myocytes have different shapes due to different sets of repolarization currents (Hua et al., 2015; Jansen et al., 2018; Lomax et al., 2003; Xu et al., 1999). Some of the experimental data for APD_{20}, APD_{50}, APD_{70}, and APD_{90} are shown in Table 2.2. There are also differences between the APs from the left and right atria (Jansen et al., 2018; Lomax et al., 2003). In general, the atrial AP is more prolonged than the ventricular AP and has additional ionic currents that affect repolarization such as the T-type Ca^{2+} current and small-conductance Ca^{2+} activated K^+ current (Curran et al., 2015; Li et al., 2009; Xu et al., 1999). Stimulation of the β-adrenergic signaling system with isoproterenol prolongs both atrial and ventricular mouse APs (Hua et al., 2015; Tong et al., 2006; Wu et al., 2002).

Table 2.2 *Experimental data on APDs in right atrial myocytes (ms).*

	APD_{20}	**APD_{50}**	**APD_{70}**	**APD_{90}**
Control				
Lomax et al. (2003)		11±2		44±5.5
Hua et al. (2015)		7.0–11.8	18.4–22.0	45.5–49.6
Jansen et al. (2018)	1.7±0.2	10.3±1.4	23.7±3.6	54.6±6.3
10 nM Iso				
Hua et al. (2015)		12.1–16.5	27.6–32.7	58.0–63.6

Our mathematical model was able to reproduce the shape of the atrial AP and APDs found experimentally at different levels of repolarization in the right atrial mouse myocytes and the effects of 1 μM isoproterenol on the APD (Fig. 2.6, Table 2.3). We also compared our simulations with those made for apical ventricular myocytes (Fig. 2.6, Table 2.3). Simulated APD_{25} for right atrial myocytes is 2.83 ms, slightly longer than APD_{20} = 1.7±0.2 ms for right atrial myocytes by

Jansen et al. (2018), but it is comparable to APD_{25} = 2.8±0.6 ms for atrial myocytes from Xu et al. (1999). Simulated APD_{50} is 6.21 ms, which is comparable to the experimental data ~7.0-11.8 ms (Hua et al., 2015; Jansen et al., 2018; Lomax et al., 2003) for right atrial cells. Simulated APD_{90} = 44.39 ms is also closed to the experimental values of 44±5.5 ms (Lomax et al., 2003), 45.5-49.6 ms (Hua et al., 2015), and 54.6±6.3 ms (Jansen et al., 2018).

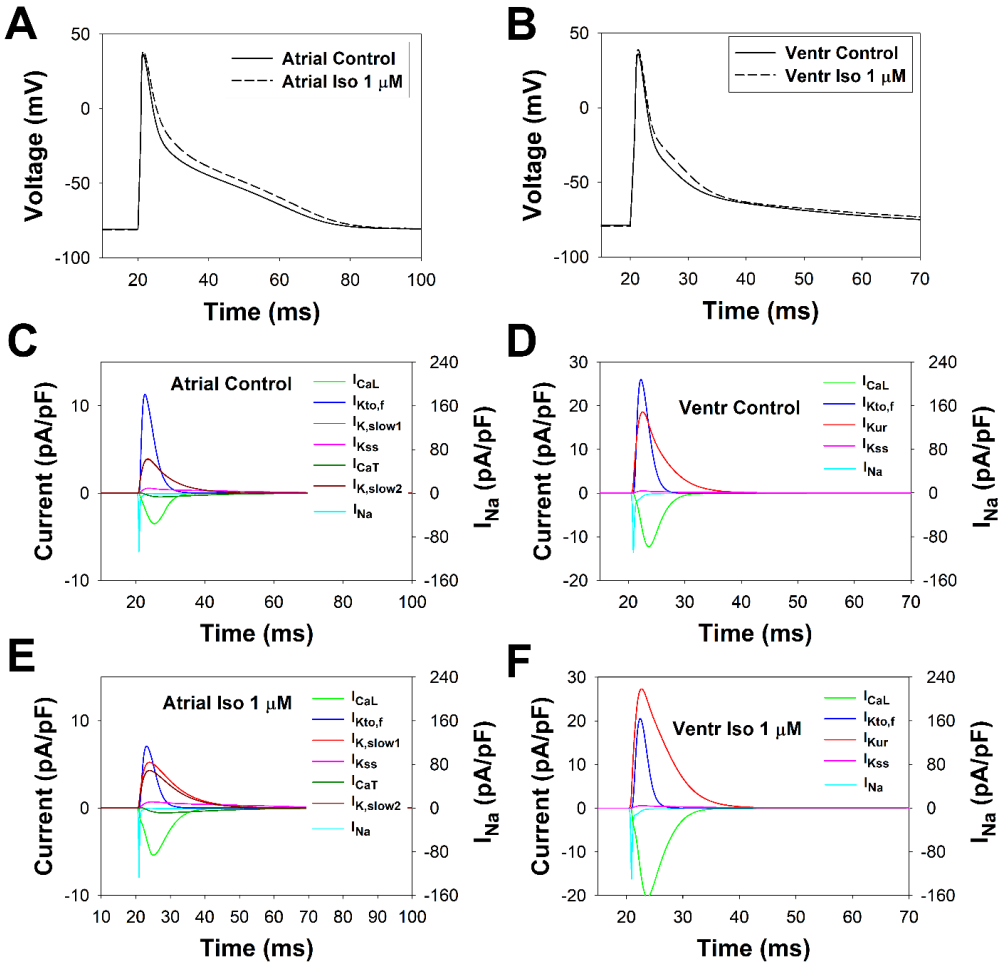

Figure 2.6 *Simulated mouse action potentials in atrial and ventricular myocytes and underlying ionic currents under different physiological conditions.*
(A) *Simulated mouse atrial action potentials for control (solid line) and after a 5 minutes exposure to 1 μM isoproterenol (dashed line).* ***(B)*** *Simulated mouse ventricular action potentials for control (solid line) and after a 5 minutes exposure to 1 μM isoproterenol (dashed line).* ***(C)*** *Simulated major ionic currents underlying mouse atrial action potential in control.* ***(D)*** *Simulated major ionic currents underlying mouse ventricular action potential in control.* ***(E)*** *Simulated major ionic currents underlying mouse atrial action potential after a 5 minutes exposure to 1 μM isoproterenol.*

(F) *Simulated major ionic currents underlying mouse ventricular action potential after a 5 minutes exposure to 1 μM isoproterenol. In (A-F), action potentials and ionic currents are obtained after 300 s stimulation with 1 Hz.*

If we compare APD_{25}, APD_{50}, APD_{75}, and APD_{90} for the right atrial versus apical ventricular myocytes, we see that the APD at all levels of repolarizations is longer for atrial myocytes (Table 2.3). The difference ranges between 66.5% for APD_{25} and 188.0% for APD_{75}. These could be explained by the differences in major repolarization currents for atrial and ventricular myocytes obtained from simulations (Figs. 2.6C and 2.6D). Mouse atrial myocytes have about twice smaller repolarizing, rapidly recovering transient outward K^+ current, $I_{Kto,f}$, compared to ventricular myocytes. The magnitude of the sum of the currents $I_{K,slow1}$ and I_{Kslow2} in atrial cells is much smaller than the magnitude of I_{Kur} in ventricular cells. The difference in outward K^+ currents is partially compensated by the difference in the inward L-type Ca^{2+} current, which is much smaller in the atrial myocytes, resulting in more prolonged APDs in atrial versus ventricular cells. Notice that the contribution of the T-type Ca^{2+} current to atrial APD is quite small as compared to the L-type Ca^{2+} current (Fig. 2.6C).

Table 2.3 *Comparison of the atrial and ventricular mouse action potential durations (ms).*

	Atrial myocyte	**Ventricular myocyte**	**APD prolongation (%) Atrial vs. Ventricular**
Control			
APD_{25}	2.83	1.70	66.5
APD_{50}	6.21	3.19	94.7
APD_{75}	26.89	9.34	188
APD_{90}	44.39	26.16	69.7
1 μM Iso			
APD_{25}	3.47	1.84	88.6
APD_{50}	8.91	3.80	134
APD_{75}	31.72	11.12	184
APD_{90}	48.48	29.97	61.8

The application of 1 μM isoproterenol (5 minutes exposure) resulted in a prolongation of both atrial and ventricular APs in simulations, which is similar to the values observed experimentally (Figs. 2.6A and 2.6B). Table 2.3 shows that atrial APD_{25} was prolonged from 2.83 to 3.47 ms (22.6% lengthening), APD_{50} - from 6.21 to 8.91 ms (43.5%), and APD_{90} - from 44.39 to 48.48 ms (9.2%). APD prolongations are comparable to those obtained after an application of 10 nM isoproterenol on mouse right atrial myocytes (Hua et al., 2015). The average experimental APD_{50} prolongation was 53%, and the average APD_{90} prolongation was 28%. Note that, although the experimental data is for a 10 nM isoproterenol concentration, it can still provide quite valid numbers for comparison to the simulation results. Because, as we demonstrated previously, mouse APDs do not change significantly within isoproterenol concentrations from 10 nM to 1 μM (Grinshpon and Bondarenko, 2016). Significantly smaller APD prolongations were observed in ventricular myocytes (Table 2.3). APD_{25} was prolonged from 1.7 to 1.84 ms (by 8.2%), APD_{50} - from 3.19 to 3.8 ms (by 19.1%), and APD_{90} - from 26.16 to 29.97 ms (by 14.6%). At all levels of repolarization, atrial APDs are more prolonged than ventricular after exposure to a 1 μM isoproterenol.

2.2.2 Ca^{2+} Dynamics in Mouse Atrial Myocytes

Simulated $[Ca^{2+}]_i$ transients and integral Ca^{2+} fluxes in mouse right atrial myocytes without and with an application of 1 μM isoproterenol are shown in Fig. 2.7. Similar simulation data for mouse ventricular myocytes were also plotted in Fig. 2.7. In control, the peak $[Ca^{2+}]_i$ transient in atrial myocytes is equal to 0.4657 μM, which is a little less than the peak $[Ca^{2+}]_i$ transient in ventricular myocytes (0.5294 μM). Simulated time-to-peak for $[Ca^{2+}]_i$ transients in mouse atrial cell is 24.1 ms, which is larger than the time-to-peak of $[Ca^{2+}]_i$ transients in mouse ventricular cell (17.1 ms) and comparable to those observed experimentally by Mancarella et al. (2008; 23±2 ms),

Glukhov, Kalyanasundaram**,** et al. (2015; ~30 ms), and Yue et al. (2017; 28.3±1.2 ms). The simulations are in line with the experimental data by Babu et al. (2007), where $[Ca^{2+}]_i$ transient in atrial myocytes was close to those in ventricular cells. Nevertheless, the simulated Ca^{2+} SR load is about 2 times larger in mouse atrial versus ventricular myocytes (1946 μM vs. 890 μM, respectively), which is close to the experimental Ca^{2+} SR loads (10.5±0.2 A.U. versus 5.85±0.20 A.U., for atrial and ventricular cells, respectively (Brandenburg et al., 2016)).

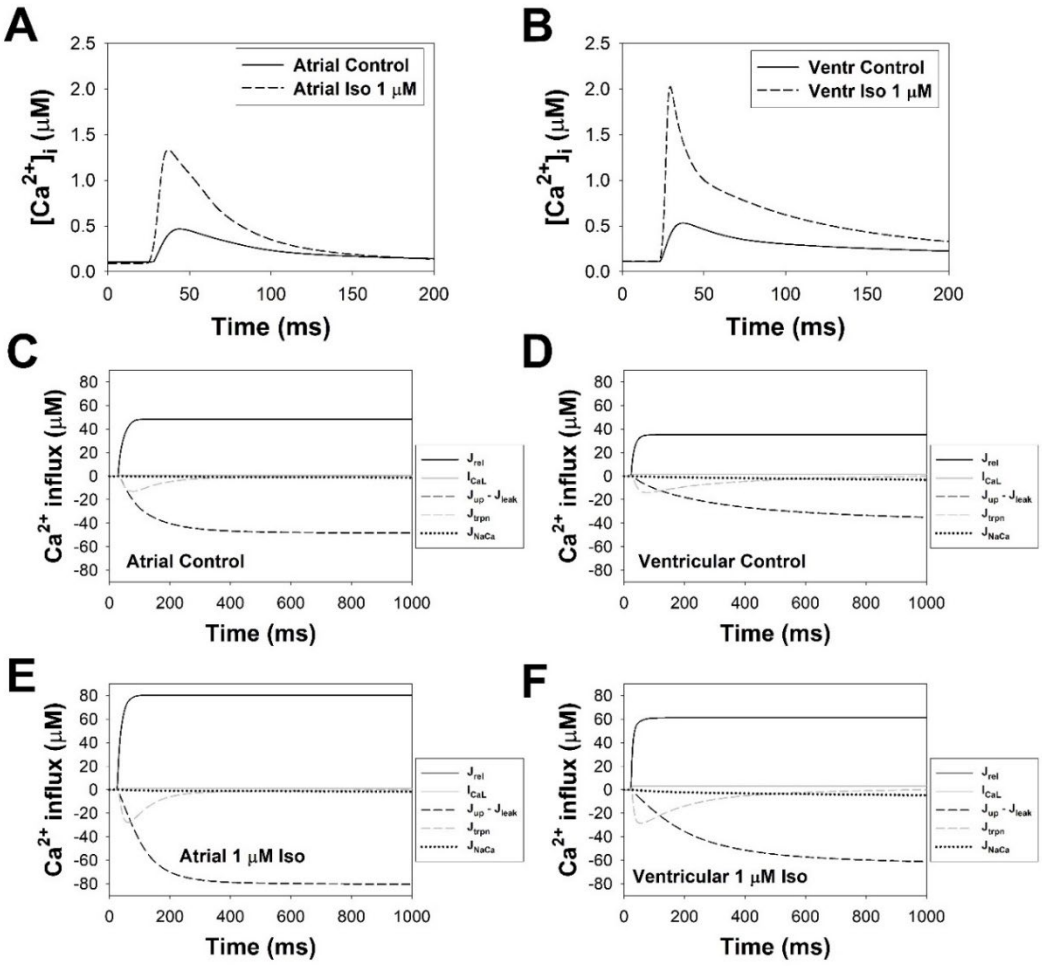

Figure 2.7 *Simulated $[Ca^{2+}]_i$ transients and Ca^{2+} fluxes in mouse atrial and ventricular myocytes under different physiological conditions.*
(A) *Simulated mouse atrial $[Ca^{2+}]_i$ transients for control (solid line) and after application of 1 μM isoproterenol (dashed line).* ***(B)*** *Simulated mouse ventricular $[Ca^{2+}]_i$ transients for control (solid line) and after application of 1 μM isoproterenol (dashed line).* ***(C)*** *Simulated Ca^{2+} influxes in mouse atrial myocytes under control conditions.* ***(D)*** *Simulated Ca^{2+} influxes in mouse ventricular myocytes under control conditions.* ***(E)*** *Simulated Ca^{2+} influxes in mouse atrial myocytes after a*

5-minute exposure to 1 μM isoproterenol. ***(F)*** *Simulated Ca^{2+} influxes in mouse ventricular myocytes after a 5-minute exposure to 1 μM isoproterenol. In (A-F), $[Ca^{2+}]_i$ transients and Ca^{2+} fluxes are obtained after 300 s stimulation with 1 Hz.*

Application of 1 μM isoproterenol increases simulated $[Ca^{2+}]_i$ transients in both atrial (1.33 μM, increase by a factor 2.85) and ventricular (2.03 μM, increase by a factor 3.83) myocytes, with the larger increase in ventricular cells (Figs. 2.7A and 2.7B). This result is qualitatively similar to the data by Babu et al. (2007), where the application of 1 μM isoproterenol increased $[Ca^{2+}]_i$ transients by factors of 1.5 and 1.64, respectively. However, it should be noted that the experimentally observed increase in $[Ca^{2+}]_i$ transients in mouse ventricular myocytes after application of 1 μM isoproterenol, as observed by others, ranges from a factor of 2 to 5 (data collected in (Bondarenko, 2014) and by a factor 3.1 in mouse atrial myocytes (Li et al., 2005). So we adjusted the atrial model parameters until we got an increase by a factor 2.85 in atrial cells, which is slightly less than 3.83 for ventricular cells.

We also simulated integral Ca^{2+} fluxes in atrial and ventricular myocytes. Simulations show a larger integral Ca^{2+} release flux in mouse atrial (48.28 μM) versus ventricular (35.04 μM) myocytes in control (Figs. 2.7C and 2.7D). However, the triggering Ca^{2+} influx by the $I_{Ca,L}$ is larger in mouse ventricular (1.57 μM) as compared to mouse atrial (0.51 μM) cells. Additional Ca^{2+} entry through the T-type Ca^{2+} channels (0.18 μM) increases the total triggering Ca^{2+} influx to 0.69 μM, which is by a factor of 2.3 less than the triggering Ca^{2+} influx in mouse ventricular cells. We suggest that the larger Ca^{2+} release flux in mouse atrial cells is mainly due to the larger SR Ca^{2+} load and smaller atrial myocyte volume (Brandenburg et al., 2016), which create a larger pro-arrhythmic substrate in mouse atrial vs. ventricular cells. Simulated Ca^{2+} extrusion by the Na^+/Ca^{2+} exchanger is larger in mouse ventricular myocytes (3.12 μM) as compared to mouse atrial myocytes (1.27 μM) due to a larger trans-sarcolemmal Ca^{2+} entry. Application of 1 μM

isoproterenol increases Ca^{2+} entry through the L-type Ca^{2+} channels both in mouse atrial (0.94 μM) and ventricular (3.29 μM) myocytes, as well as integral Ca^{2+} release fluxes in mouse atrial (80.32 μM) and ventricular (61.16 μM) myocytes (Figs. 2.7E and 2.7F). The integral Ca^{2+} influxes and Ca^{2+} release fluxes increase by a factor of 2 after isoproterenol application.

2.2.3 The Effects of the T-type Ca^{2+} Current on Atrial Action Potential and Ca^{2+} Dynamics

Experimental measurements of the $I_{Ca,T}$ in cardiac cells is quite difficult due to its significant overlap with the $I_{Ca,L}$. The $I_{Ca,T}$ was found in both atrial and ventricular myocytes of different species and in sino-atrial nodal cells (for a review, see (Vassort et al., 2006)). $I_{Ca,T}$ was also found in mouse atrial myocytes (Curran et al., 2015). Experimental data also demonstrated that the $I_{Ca,T}$ affects pacemaking activity of sinoatrial nodal cells, as well as causes prolongation of the AP in the mouse Purkinje cells (Vaidyanathan et al., 2013) or, if expressed in pathological conditions, in mouse ventricular myocytes (Jaleel et al., 2008). There are different experimental data on the role of the $I_{Ca,T}$ in triggering Ca^{2+}-induced Ca^{2+}-release from the SR. Some experimental data show the minor role of the T-type Ca^{2+} current in triggering Ca^{2+}-releases (Jaleel et al., 2008; Sipido et al., 1998), while other data demonstrates that the $I_{Ca,T}$ can be responsible for a substantial part of Ca^{2+} release (Kitchens et al., 2003).

To investigate the role of the T- and L-type Ca^{2+} currents in shaping the mouse right atrial AP and its effects on $[Ca^{2+}]_i$ transients, we performed simulations under different physiological conditions (Fig. 2.8). Figure 2.8A demonstrates the effects of the $I_{Ca,T}$ block on the APD. Note that despite the small magnitude of the $I_{Ca,T}$, ~0.5 pA/pF, it makes a significant contribution to the shape of the AP. It can be seen from the figure that the effect is mostly on the later stage of repolarization, where the inhibition of I_{CaT} shortens APD_{50}, APD_{75}, and APD_{90} by 2.5%, 18%, and

14%, respectively. A similar effect is seen after $I_{Ca,T}$ block in the presence of 1 μM isoproterenol, where APD_{75} and APD_{90} are shortened by 19% and 15%, respectively. The $I_{Ca,T}$ block also affects peak $[Ca^{2+}]_i$ transient, which decreases by ~13% in control and by ~15% in the presence of 1 μM isoproterenol (Fig. 2.8B). A similar minor effect of the $I_{Ca,T}$ block on $[Ca^{2+}]_i$ transient is observed experimentally by Sipido et al. (1998) in guinea pig ventricular myocytes.

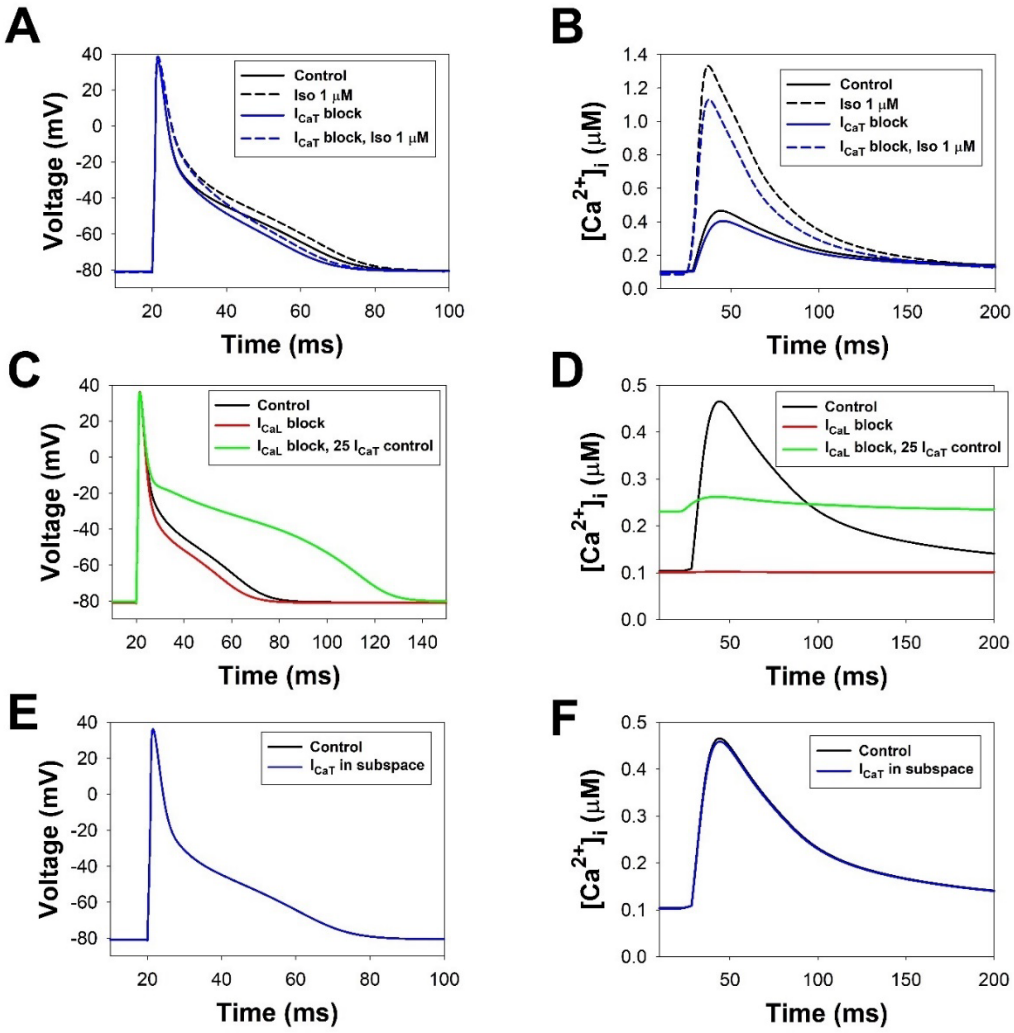

Figure 2.8 *Simulated atrial action potential and $[Ca^{2+}]_i$ transient under different physiological conditions.*
(A) *Simulated action potentials in control (solid black line), after application of 1 μM isoproterenol (dashed black line), upon I_{CaT} block (solid blue lines), upon I_{CaT} block, and after application of 1 μM isoproterenol (dashed blue line).* ***(B)*** *Simulated $[Ca^{2+}]_i$ transient in control (solid black line), after application of 1 μM isoproterenol (dashed black line), upon I_{CaT} block (solid blue lines), upon I_{CaT} block, and after application of 1 μM isoproterenol (dashed blue line).*

(C) *Simulated action potentials in control (solid black line), upon I_{CaL} block (solid red lines), and upon I_{CaL} block and a 25-fold increase of the control I_{CaT} magnitude (solid green line).* ***(D)*** *Simulated $[Ca^{2+}]_i$ transient in control (solid black line), upon I_{CaL} block (solid red lines), and upon I_{CaL} block and a 25-fold increase of the control I_{CaT} magnitude (solid green line).* ***(E)*** *Simulated action potentials in control (solid black line) and after hypothetical movement of I_{CaT} to subspace volume (solid blue line).* ***(F)*** *Simulated $[Ca^{2+}]_i$ transient in control (solid black line) and after hypothetical movement of I_{CaT} to subspace volume (solid blue line).*

It would also be interesting to see how the $I_{Ca,L}$ block affects the shape of the mouse atrial AP. Figure 2.8C shows the effect is stronger than that from the $I_{Ca,T}$ block. The $I_{Ca,L}$ block decreases the APD at 50%, 75%, and 90% repolarization by 17%, 27%, and 16%, respectively. It also essentially eliminates $[Ca^{2+}]_i$ transient (Fig. 2.8D). This simulation demonstrates that the $I_{Ca,L}$ is mostly responsible for the Ca^{2+}-induced Ca^{2+} release in mouse atrial myocytes. A similar effect is observed in the experiments with guinea pig ventricular myocytes, where the $I_{Ca,L}$ block basically eliminated $[Ca^{2+}]_i$ transient (Sipido et al., 1998).

We also simulated the effects of overexpression of I_{CaT} in mouse atrial myocytes when the $I_{Ca,L}$ is blocked (Fig. 2.8C). In this simulation, we increased the magnitude of the $I_{Ca,T}$ by a factor of 25 from its control value. An increase in the magnitude of $I_{Ca,T}$ is then found to dramatically prolong the mouse's atrial AP duration (by about 3-fold for APD_{50} and APD_{75} and by about 2-fold for APD_{90}). Note that a similarly dramatic increase in APDs was observed in mouse ventricular myocytes with similar overexpression of I_{CaT} (Lipp & Niggli, 1994). Our simulations also demonstrated a noticeable but much smaller $[Ca^{2+}]_i$ transient (green line in Fig. 2.8D), which was generated in mouse atrial myocytes overexpressing I_{CaT} and at the $I_{Ca,L}$ block, as compared to the control cells (black line in Fig. 2.8D).

Finally, we tested a hypothesis that the localization of T-type Ca^{2+} channels in the subspace volume (in the extracaveolar domain, Fig. 2.1) can trigger larger $[Ca^{2+}]_i$ transients compared to their natural localization in the caveolar and cytosolic domains. Figures 2.8E and 2.8F show the

results of simulations for control (solid black lines) and for relocated T-type Ca^{2+} channels (solid blue lines), which are virtually identical. We consider that a smaller magnitude of I_{CaT} as compared to I_{CaL} is responsible for this behavior. This results in a significantly smaller Ca^{2+} entry through the T-type Ca^{2+} channels to the subspace volume as compared to the L-type Ca^{2+} channels. Our simulations agree with the findings of Bovo et al. (2011) on the non-linear (threshold-like) dependence of Ca^{2+} exit from the SR through ryanodine receptors. The latter suggests a much smaller or no Ca^{2+} release from the SR at relatively small values of $[Ca^{2+}]_i$, which could be achieved by the Ca^{2+} entry through T-type Ca^{2+} channels as compared to the L-type Ca^{2+} channels.

Thus, our simulations show that both the T- and L-type Ca^{2+} currents significantly affect the shape of the mouse atrial AP. When the T- and L-type Ca^{2+} currents are available, or only the L-type Ca^{2+} current is available, we obtained Ca^{2+}-induced Ca^{2+} release and normal $[Ca^{2+}]_i$ transients. When there is only the T-type Ca^{2+} current, Ca^{2+} release from the SR is not happening.

2.2.4 The Effects of the Small-Conductance K^+ Current on Atrial Action Potential and Ca^{2+} Dynamics

Experimental data demonstrates that the small-conductance K^+ current $I_{Ca,K}$ can play a role in shaping mouse atrial AP (Hancock et al., 2015; Xu et al., 2003; Yi et al., 2015; Zhang et al., 2014). Block of $I_{Ca,K}$ with apamin resulted in AP prolongation. However, a marked impact of $I_{Ca,K}$ was observed in mouse atrial myocytes at relatively high intracellular $[Ca^{2+}]_i$ concentrations equal to 1 μM. On the other hand, experimental observations with atrial myocytes from other species (dog, rat) under normal physiological conditions do not show any noticeable contribution of $I_{Ca,K}$ to AP morphology (Nagy et al., 2009).

Therefore, we simulated the effects of the small-conductance K^+ current $I_{Ca,K}$ on the mouse atrial AP and $[Ca^{2+}]_i$ transients under different physiological conditions. Figure 2.9A shows that the AP under control conditions was not affected by $I_{Ca,K}$, as the block of this current does not

change the shape of AP. The effect is noticeable under stimulation of the β-adrenergic signaling system with 1 μM isoproterenol and only in the later phase of repolarization (Fig. 2.9A). APD_{75} and APD_{90} prolongations upon $I_{Ca,K}$ block was only ~3-4%, which are quite difficult to measure experimentally. The mechanism of this prolongation is shown in Fig. 2.9D, where $I_{Ca,K}$ was much larger upon application of 1 μM isoproterenol (black dashed line) compared to the control conditions (solid black line). In this respect, our simulations confirm the results of Nagy et al. (2009) that there is no effect of $I_{Ca,K}$ block on the atrial AP under normal physiological conditions.

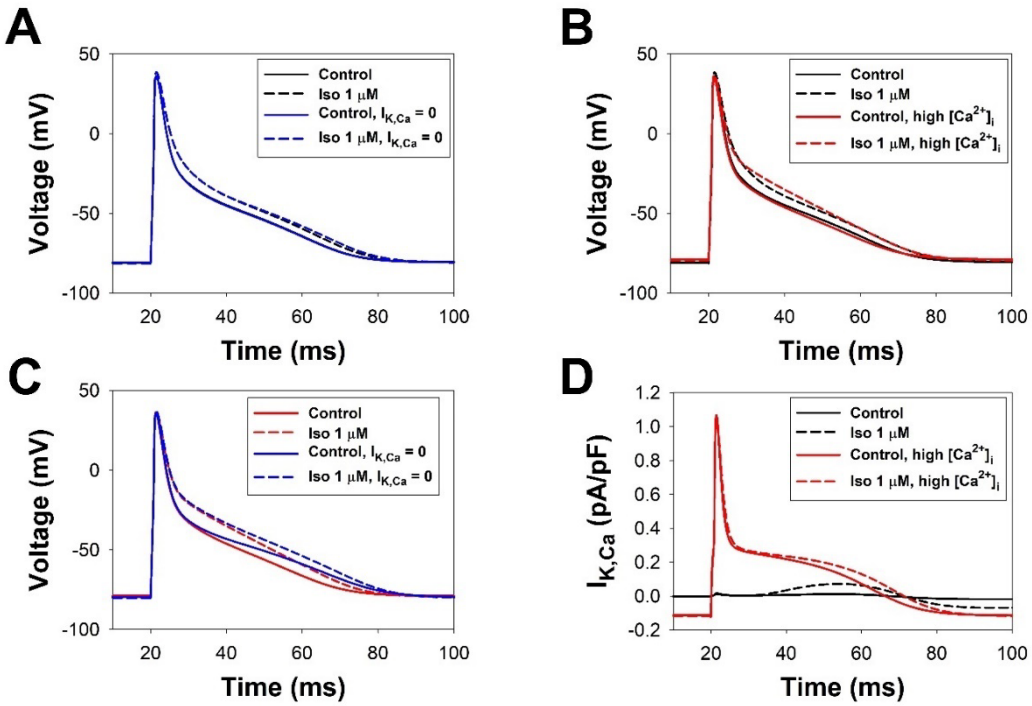

Figure 2.9 *Simulated atrial action potential and Ca^{2+}-activated K^+ current ($I_{K,Ca}$) under different physiological conditions.*
(A) *Simulated action potentials with normal $[Ca^{2+}]_i$ transient in control (solid black line), after application of 1 μM isoproterenol (dashed black line), upon $I_{K,Ca}$ block (solid blue lines), upon $I_{K,Ca}$ block and after application of 1 μM isoproterenol (dashed blue line).* ***(B)*** *Simulated action potentials with normal $[Ca^{2+}]_i$ transient in control (solid black line) and after application of 1 μM isoproterenol (dashed black line); simulated action potentials with high $[Ca^{2+}]_i$ = 1 μM in control (solid red lines) and after application of 1 μM isoproterenol (dashed red line).* ***(C)*** *Simulated action potentials with $[Ca^{2+}]_i$ = 1 μM in control (solid red lines), after application of 1 μM isoproterenol (dashed red line), upon $I_{K,Ca}$ block (solid blue lines), and upon $I_{K,Ca}$ block, and after application of*

1 μM isoproterenol (dashed blue line). ***(D)*** *Simulated $I_{K,Ca}$ currents with normal $[Ca^{2+}]_i$ transient in control (solid black line) and after application of 1 μM isoproterenol (dashed black line); simulated $I_{K,Ca}$ currents with $[Ca^{2+}]_i$ = 1 μM in control (solid red lines) and after application of 1 μM isoproterenol (dashed red line).*

Simulations also demonstrated a slight shortening of the atrial AP under high intercellular calcium transient ($[Ca^{2+}]_i$ = 1 μM) conditions compared to control (Fig. 2.9B). APD_{25} was reduced by 5%, APD_{50} – by 7.4%, and APD_{90} – by 7.6%. The reduction was attributable to the larger magnitude of $I_{Ca,K}$ under high $[Ca^{2+}]_i$ conditions (Fig. 2.9D).

However, the strongest effect of $I_{Ca,K}$ block on the mouse atrial AP was obtained for higher $[Ca^{2+}]_i$ (Fig. 2.9C). Without the application of isoproterenol, the effects were predominantly on APD_{75} and APD_{90}, which were prolonged by 10% and 12%, respectively. The results of simulations are in agreement with the experimental data by Hankock et al. (2015), where APD_{90} was prolonged by 10% after $I_{Ca,K}$ block. They are also in line with the data by Yi et al. (2015), where significant prolongation was observed for APD_{90} (by 22%), but not for APD_{50}. We also obtained a larger prolongation of the APD after applying 1 μM isoproterenol, which enhanced the effect of $I_{Ca,K}$ block, resulting in prolongation of APD_{50}, APD_{75}, and APD_{90} by 14%, 16%, and 10%, respectively. We did not find the corresponding experimental data for comparison.

The effect of $I_{Ca,K}$ block on $[Ca^{2+}]_i$ transients was simulated both in control and after application of 1 μM isoproterenol under normal physiological conditions. In both cases, the effect was negligible, less than 1%.

2.2.5 Frequency Dependences of the AP and $[Ca^{2+}]_i$ Transients

We also investigated the frequency dependences of the APDs at different levels of repolarization and the $[Ca^{2+}]_i$ transients without and with the application of 1 μM isoproterenol. Figure 2.10A shows that APD_{25} and APD_{50} moderately increased and APD_{90} moderately decreased at higher pacing frequencies. These behaviors sustain after the application of 1 μM isoproterenol,

which prolongs APDs at all levels of repolarization. The weak frequency dependence of simulated APDs is in line with the experimental data by Lu et al. (2007), where no significant frequency dependence of APD_{50} and APD_{90} was observed in the range from 0.1 to 10 Hz. Another experimental paper (Hua et al., 2015) also suggests APD prolongation after the application of isoproterenol which supports our simulation result.

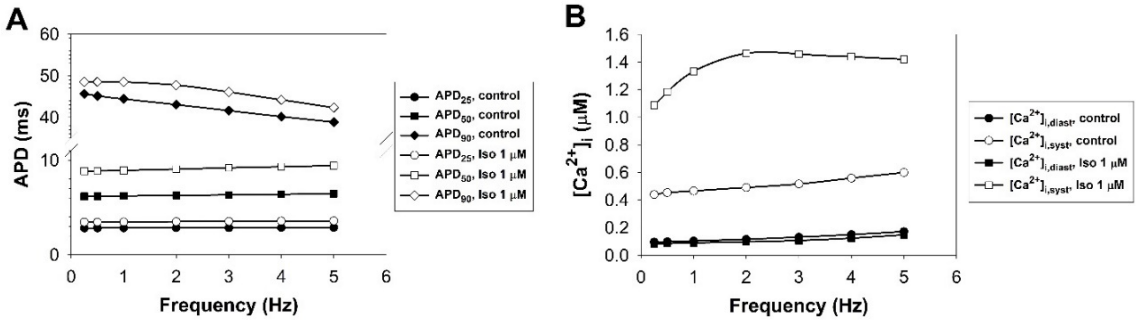

Figure 2.10 *Simulated atrial action potential durations (APDs) and [Ca2+]$_i$ transients as functions of stimulation frequency.*
(A) *Simulated APD_{25} (circles), APD_{50} (squares), and APD_{90} (diamonds) as a function of stimulation frequency in control (closed symbols) and after 5-minute exposure to 1 μM isoproterenol (open symbols).* ***(B)*** *Simulated diastolic (closed symbols) and systolic (open symbols) $[Ca^{2+}]_i$ transients as a function of stimulation frequency in control (circles) and after 5-minute exposure to 1 μM isoproterenol (squares).*

Our simulations show an increase in both diastolic and systolic $[Ca^{2+}]_i$ concentrations with stimulation frequency in control (Fig. 2.10B). We suggest that this increase is due to the larger Ca^{2+} influx mainly through the L-type Ca^{2+} channels with the stimulation frequency per unit time, which Ca^{2+} removal by the Na^+/Ca^{2+} exchanger does not completely compensate. After an application of 1 μM isoproterenol, the dependence becomes biphasic. It includes an increasing part at the lower stimulation frequencies and a weakly decreasing part at the higher frequencies. We suggest the same mechanism of frequency dependence for $[Ca^{2+}]_i$ transients without isoproterenol. However, we need to take into account a quite large increase in the L-type Ca^{2+} current that leads to about a 2-3-fold increase in $[Ca^{2+}]_i$ transient, resulting in the faster Ca^{2+} removal by the Na^+/Ca^{2+}

exchanger at higher frequencies. At smaller stimulation frequencies, the Na^+/Ca^{2+} exchanger cannot compensate Ca^{2+} influx through the L-type Ca^{2+} channels due to a relatively small systolic $[Ca^{2+}]_i$ concentration. As the systolic $[Ca^{2+}]_i$ concentration increases with the stimulation frequency, more Ca^{2+} is extruded by the Na^+/Ca^{2+} exchanger. For example, after the application of 1 μM isoproterenol, the peak I_{CaL} increases by ~4%, and peak I_{NaCa} increases by ~44% when stimulation frequency changes from 0.5 to 4 Hz.

2.2.6 Sensitivity Analysis

In order to define how cell-to-cell variability of the ionic current expression affects the AP and $[Ca^{2+}]_i$ transients in mouse atrial myocytes without and with β-adrenergic stimulation, we performed a sensitivity analysis (Fig. 2.11). For this purpose, we first increased and then decreased the conductance of each of the model currents by 20% as compared to the baseline model (the magnitude of changes was similar to that used by Sobie (2009) and Kernik et al. (2019)). We then stimulated the resulting atrial model cell for 300 s with a basic cycle length 1000 ms (I_{stim} = 80 pA/pF, τ_{stim} = 1 ms) and calculated APD_{25}, APD_{50}, APD_{90}, AP amplitude, and $[Ca^{2+}]_i$ transients in control and after application of 1 μM isoproterenol. The AP and $[Ca^{2+}]_i$ characteristics were compared to the model with baseline parameters in control and after application of 1 μM isoproterenol.

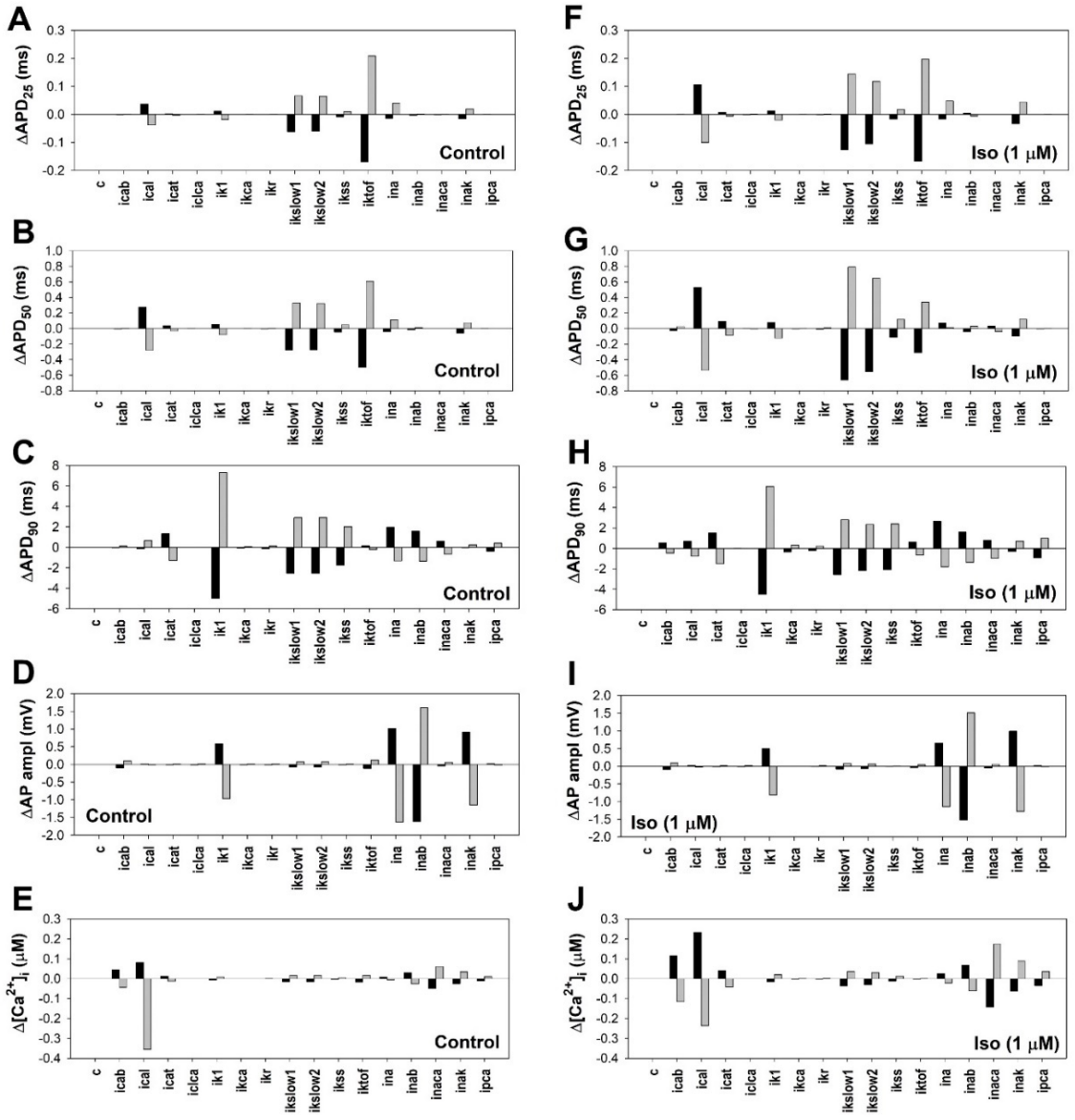

Figure 2.11 *Sensitivity analysis.*
*Changes of action potential (AP) durations at 25% (**Panels A and F**), 50% (**Panels B and G**), and 90% repolarizations (**Panels C and H**), AP amplitude (**Panels D and I**), and $[Ca^{2+}]_i$ transient (**Panels E and J**) between the two consecutive stimuli (the 301st and 300th pacing beats) at 1 Hz. We increased and decreased the magnitude of one of several ionic currents by 20%, and the model cell was paced with 300 stimuli. The changes were calculated as the differences between AP durations, AP amplitudes, and $[Ca^{2+}]_i$ transients during the 301st and 300th beats. Simulations were performed without isoproterenol (Control, **Panels A-E**) and after a 5-minute application of 1 μM isoproterenol (**Panels F-J**). Sensitivity analysis is performed with respect to 20% increase (black bars) and 20% decrease (gray bars) of the L-type Ca^{2+} current (ica,l), the T-type Ca^{2+} current (icat), the sarcolemmal Ca^{2+} pump current (ipca), the Na^+/Ca^{2+} exchanger current (inaca), the Ca^{2+} background current (icab), the fast Na^+ current (ina), the Na^+ background*

current (inab), the Na^+-K^+ pump current (inak), the rapidly recovering transient outward K^+ current (iktof), the time-independent K^+ current (ik1), the rapidly activating, slowly inactivating K^+ current (encoded by $K_v1.5$; 4-aminopyridine-sensitive; ikslow1), the rapidly activating, slowly inactivating K^+ current (encoded by $K_v2.1$; TEA-sensitive; ikslow2), the noninactivating steady-state voltage-activated K^+ current (ikss), the small-conductance Ca^{2+}-activated K^+ current (ikca), the rapid delayed rectifier K^+ current (ikr), and the Ca^{2+}-activated chloride current (iclca). No changes are shown for the simulations without 20% perturbation of the model parameters (c).

In control, the major player for APD_{25} and APD_{50} is the rapidly recovering transient outward K^+ current, $I_{Kto,f}$ (Fig. 2.11, A and B). Three other currents, the L-type Ca^{2+} current, I_{CaL}, and two rapidly activating, slowly inactivating K^+ currents, $I_{K,slow1}$ and $I_{K,slow2}$, also made significant contributions to the change in APD_{25} and APD_{50}. The K^+ currents tend to shorten, while I_{CaL} tends to prolong APD_{25} and APD_{50}. The regulation of APD_{90} is more complex. Eight major ionic currents affect APD_{90} (Fig. 2.11C). An increase in the T-type Ca^{2+} current, I_{CaT}, the fast Na^+ current, I_{Na}, the background Na^+ current, I_{Nab}, and the Na^+/Ca^{2+} exchanger current, I_{NaCa}, tend to prolong APD_{90}, while the time-independent K^+ current, I_{K1}, two rapidly activating, slowly inactivating K^+ currents, $I_{K,slow1}$ and $I_{K,slow2}$, and the noninactivating steady-state voltage-activated K^+ current, I_{Kss}, tend to shorten APD_{90}. In control, AP amplitude is affected by four major currents (Fig. 2.11D). Three currents, I_{Na}, I_{NaK}, and I_{K1}, increase, while I_{Nab} decreases AP amplitude. The major contributing factor to $[Ca^{2+}]_i$ transient is the L-type Ca^{2+} current (Fig. 2.11E). Four other currents, the Na^+/Ca^{2+} exchanger current, I_{NaCa}, the background Ca^{2+} current, I_{Cab}, the Na^+/K^+ pump current, I_{NaK}, and the background Na^+ current, I_{Nab}, also made some noticeable contributions. $[Ca^{2+}]_i$ increased with an increase in I_{Cab} and I_{Nab} and decreased with an increase in I_{NaCa} and I_{NaK}.

Upon application of 1 μM isoproterenol, APD_{25} and APD_{50} were affected by the same four major currents, I_{CaL}, $I_{Kto,f}$, $I_{K,slow1}$, and $I_{K,slow2}$, but in different proportions. For APD_{25}, the effect of $I_{Kto,f}$ was not changed, but the contribution of I_{CaL}, $I_{K,slow1}$, and $I_{K,slow2}$ increased (Fig. 2.11F). In APD_{50}, the role of $I_{Kto,f}$ decreased, but I_{CaL}, $I_{K,slow1}$, and $I_{K,slow2}$ increased their effects (Fig. 2.11G).

Nine currents affect APD_{90} after the application of 1 μM isoproterenol (Fig. 2.11H). Among them, eight currents have similar action as in control, and one additional current, $I_{p(Ca)}$, also increased the tendency to shorten APD_{90}. The major players and their proportional contributions that affect AP amplitude and $[Ca^{2+}]_i$ transient after stimulation of the β-adrenergic signaling system are the same as in control (Fig. 2.11, I and J).

2.3 Discussion

This dissertation introduces a novel and comprehensive compartmentalized mathematical model that simulates APs from the mouse right atrial myocytes with developed TATS. The model includes three compartments (caveolae, extracaveolae, and cytosol) related to β_1- and β_2-adrenergic signaling systems, as well as compartmentalized Ca^{2+} dynamics that describe local control of Ca^{2+}-induced Ca^{2+} release (Fig. 2.1). Using this model, we described several differences in APs and Ca^{2+} dynamics between atrial and ventricular myocytes and the role of atrial-specific currents I_{CaT} and $I_{K,Ca}$ in shaping the AP and $[Ca^{2+}]_i$ transients. Finally, we performed a sensitivity analysis to demonstrate the variability of the AP and $[Ca^{2+}]_i$ transients due to the cell-to-cell variability of ionic currents.

2.3.1 Differences in AP and Ca^{2+} Dynamics Between Atrial and Ventricular Myocytes

Experimental investigations demonstrated significant differences in the mechanism of AP and $[Ca^{2+}]_i$ transient generation between atrial and ventricular myocytes (Ng et al., 2010). Specifically, ventricular myocytes are larger in size, have, in general, a more prolonged AP and a different set of repolarizing currents, and generate larger $[Ca^{2+}]_i$ transients and contraction force. For example, in the rabbit heart, atrial AP has a triangular shape, while ventricular AP has a prominent depolarization plateau (Giles & Imaizumi, 1988). In addition, atrial AP has a shorter duration, a larger transient outward K^+ current, and a larger Ca^{2+}-dependent K^+ current (Giles &

Imaizumi, 1988). In humans, atrial AP also has a larger transient outward K^+ current, smaller Na^+/Ca^{2+} exchanger and Na^+-K^+ pump currents, a smaller I_{K1} current, and a decreased availability of the ultra-rapidly activating K^+ current (which is absent in human ventricular myocytes) (Grandi et al., 2011). Therefore, mathematical models have been developed both for atrial and ventricular myocytes for these and other species to simulate these differences (Lindblad et al., 1996; Nygren et al., 1998; Ramirez et al., 2000; Shannon et al., 2004; ten Tusscher et al., 2004; Winslow et al., 1999).

Similar to other species, there are differences between mouse atrial and ventricular APs due to the differences in the cell size, magnitude of the L-type Ca^{2+} current, expression of Na^+-K^+ and SERCA pumps, calsequestrin, and phospholamban, as well as atrial-specific ionic currents, I_{CaT} and $I_{K,Ca}$ (Curran et al., 2015; Li et al., 2009). As a result, mouse atrial myocytes have a longer APD and possess smaller $[Ca^{2+}]_i$ transients.

Our model incorporates all of the AP differences between atrial and ventricular mouse myocytes mentioned above. The model also considers differences in geometries and expression of Ca^{2+} handling proteins. As a result, the model was able to reproduce the much higher SR Ca^{2+} load found experimentally by Brandenburg et al. (2016) in mouse atrial versus ventricular myocytes. It should be noted that such differences in the SR load between atrial and ventricular myocytes are not unique for mice. Similar differences were found in the rat (Walden et al., 2009) and fish hearts (Haverinen & Vornanen, 2009). Our model also predicted higher Ca^{2+} fluxes inside the atrial myocytes than ventricular cells, which future experiments can verify.

The model also simulated experimental findings on the effects of β-adrenergic stimulation by isoproterenol, including APD prolongation (Fig. 2.6 and Tables 2.2-2.3). Simulated APD_{50} prolongation (~43.5%) was close to that observed experimentally (~53%) (Hua et al., 2015). On

the other hand, simulated APD_{90} prolongation (~9.2%) was somewhat smaller than experimental values (~28%) (Hua et al., 2015). The effect of β-adrenergic stimulation in mouse atrial myocytes was similar to that in ventricular cells, which also led to AP prolongation (Fig. 2.6). Simulations with the application of 1 μM isoproterenol to the mouse atrial myocytes resulted in 2.85 fold larger $[Ca^{2+}]_i$ transients compared to unstimulated cells. This value is within the range that was observed in experiments (1.5 to 3.1-fold increase) (Babu et al., 2007; Li et al., 2005). The model also closely simulated an experimentally found increase in the magnitude of the T-type Ca^{2+} current upon stimulation of β-adrenoceptors (Fig. 2.3; (Li et al., 2012)). It also reproduced the time course of phosphorylation and the fraction of phosphorylated channels of the small-conductance Ca^{2+}-activated K^+ current (Fig. 2.4).

2.3.2 The T-Tubular System in Atrial Myocytes

Our model was designed specifically for right atrial myocytes with developed TATS. The presence and functional role of the atrial t-tubule system has been debatable for a long time. However, recent experimental studies clearly showed the functional presence of both transversal and axial tubules (i.e., TATS) in the atria of various species, including mice, rats, rabbits, sheep, pigs, horses, and humans (Brandenburg et al., 2016; Brandenburg et al., 2018; Dibb et al., 2009; Frisk et al., 2014; Glukhov, Balycheva, et al., 2015; Richards et al., 2011). It was shown that TATS is likely heterogeneously expressed throughout the atria: whole atria TATS staining indicates that myocytes with TATS seem to be localized within the muscle bundles of the atrial appendages (Glukhov, Balycheva, et al., 2015). In general, atrial TATS is sparse and less regular when compared with the well-organized t-tubule system in ventricular myocytes as assessed both *in situ* (Wei et al., 2010) and *in vitro* (Smyrnias et al., 2010). Moreover, a dense network of axial components may significantly contribute to the synchronization of subcellular Ca^{2+} release

compensating for the irregular organization of atrial TATS (Brandenburg et al., 2016; Brandenburg et al., 2018; Yue et al., 2017). As the first step in modeling mouse atrial myocytes, we have chosen myocytes located within the right atrial appendage and possessed a developed TATS. We did not discriminate axial tubules from transversal ones and considered TATS as a part of the sarcolemma membrane with a similar distribution to the three compartments used in the model. Modeling atrial myocytes that do not have TATS and where subcellular Ca^{2+} release relies on Ca^{2+} diffusion from the submembrane regions towards the cell interior would require a different computational approach (Koivumäki et al., 2011).

2.3.3 The Role of the T-type Ca^{2+} Current in Shaping AP and Ca^{2+} Dynamics

The T-type Ca^{2+} current in cardiac cells was found in 1985 (Bean, 1985; Nilius et al., 1985). It was present in the whole heart during the embryonic stage but mainly remained in sinoatrial and atrioventricular nodal cells and in atrial and Purkinje cells in adult hearts (Li et al., 2018; Vassort et al., 2006). The T-type Ca^{2+} current has a smaller amplitude than the L-type Ca^{2+} current and is activated at more hyperpolarized voltages than the L-type Ca^{2+} current. For a long time, it was considered that the T-type Ca^{2+} current plays a minor role in cardiac repolarization and Ca^{2+} dynamics. It was also difficult to study the properties of the T-type Ca^{2+} current due to the difficulty of its separation from the L-type Ca^{2+} current (Vassort et al., 2006).

The T-type Ca^{2+} current plays multiple physiological roles in the heart. It was shown that I_{CaT} is expressed in pacemaker myocytes, including the sino-atrial and atrioventricular nodes and Purkinje fibers, and thus might be involved in heart rhythm regulation in mice and other species (Mesirca et al., 2015). Li et al. (2018) have shown that β-adrenergic stimulation affects the heart rhythm by increasing I_{CaT} magnitude in sino-atrial nodal cells. In embryonic hearts, I_{CaT} may play

a role in sustaining ventricular automaticity together with the hyperpolarization-activated inward current I_f (Niwa et al., 2004).

Our simulations showed that I_{CaT} affects the later phase of the mouse atrial AP repolarization (Fig. 2.8A). We found that the block of I_{CaT} resulted in the shortening of APD_{75} and APD_{90} by 18% and 14%, respectively. Simulation of the overexpression of the T-type Ca^{2+} channels resulted in a dramatic prolongation of APD_{75} and APD_{90} by 3-fold and 2-fold, respectively. These results agree with the experimental observation of APD prolongation in mouse ventricular myocytes overexpressing T-type Ca^{2+} channels (Jaleel et al., 2008).

The late phase of cardiac repolarization is an important phase as it is mostly responsible for the APD and the length and variation of the refractory period in cardiac cells and tissues (Trenor et al., 2017). APD affects the degree of inactivation of the voltage-activated Na^+, Ca^{2+}, and K^+ currents in cardiac cells, as they have different time constants of inactivation. This results in different recovery times of these channels, from inactivation to participation in the generation of subsequent APs. The T-type Ca^{2+} current, affecting this phase, plays a significant role in regulating APD_{75} and APD_{90}. Prolongation of the AP due to the increased magnitude of I_{CaT} provides an antiarrhythmic effect for re-entrant arrhythmias. At the same time, the increased expression of I_{CaT} increases susceptibility to triggered arrhythmias through early afterdepolarizations. For example, I_{CaT}, while absent in healthy adult ventricles, was detected in ventricular cells of several animal models of cardiac hypertrophy with pronounced re-entrant and triggered arrhythmias, where it can play both pro-and antiarrhythmic roles (Martínez et al., 1999; Nerbonne & Kass, 2005).

There are some controversies in the interpretation of the role of the T-type Ca^{2+} current in triggering Ca^{2+}-induced Ca^{2+} release. It was found that I_{CaT} provides an additional Ca^{2+} influx into the cardiac cell (Sipido et al., 1998). However, it is quite unclear whether it triggers Ca^{2+} release

from the SR. Sipido et al. (1998) found that the T-type Ca^{2+} current can trigger Ca^{2+} release in guinea pig ventricular myocytes. However, the T-type Ca^{2+} current is less efficient than the L-type Ca^{2+} current in triggering Ca^{2+} release. On the other hand, the Na^{+}/Ca^{2+} exchanger was proposed as a trigger of Ca^{2+} release (Lipp & Niggli, 1994). In addition, the localization of the T-type Ca^{2+} channels apart from the Ca^{2+} release channels favors a minor role of the T-type Ca^{2+} current in Ca^{2+} release (Jaleel et al., 2008; Markandeya et al., 2011).

Using the presented mathematical model, we investigated the role of I_{CaT} in triggering Ca^{2+} release in mouse atrial myocytes. Although I_{CaT} contributed to $[Ca^{2+}]_i$ transient, we found that it did not produce Ca^{2+}-induced Ca^{2+} release when I_{CaL} was blocked. In addition, we have shown that the hypothetical re-localization of the T-type Ca^{2+} channels to dyadic space did not change significantly $[Ca^{2+}]_i$ transient.

2.3.4 The Role of $I_{K,Ca}$ Current in Generating AP and Ca^{2+} Dynamics

The small conductance Ca^{2+}-dependent K^{+} current, $I_{K,Ca}$, is present in both atrial and ventricular myocytes (Tuteja et al., 2005). Some studies demonstrated that $I_{K,Ca}$ contributes to cardiac repolarization under high Ca^{2+} conditions when the block of $I_{K,Ca}$ prolongs APD (Xu et al., 2003). Other studies demonstrated no effect of this current on the AP shape both in atrial and ventricular myocytes of different species under normal physiological conditions (Nagy et al., 2009).

To address this issue, we simulated the effects of $I_{K,Ca}$ block on repolarization of the mouse atrial AP (mouse ventricular myocytes do not express a significant amount of SK channels) under normal and high Ca^{2+} conditions. Our data indicate that there is no effect of $I_{K,Ca}$ block on mouse atrial AP under normal physiological conditions (Fig. 2.9A). However, some effect was noticed upon stimulation of the β-adrenergic signaling system with 1 μM isoproterenol, where a small

APD prolongation was observed (Fig. 2.9A). Even a larger APD prolongation was obtained in simulations of $I_{K,Ca}$ block at high Ca^{2+} conditions (Fig. 2.9C). This allowed us to conclude that $I_{K,Ca}$ block can prolong APD and potentially be both pro-arrhythmic (for early afterdepolarization-induced arrhythmias) and anti-arrhythmic (for reentrant arrhythmias).

While no significant effects of $I_{K,Ca}$ block were observed in atrial myocytes under normal physiological conditions, a connection between $I_{K,Ca}$ expression, and atrial fibrillation were identified in several species (see review by Diness et al. (2015)). Experimental findings show that both up- and downregulation of $I_{K,Ca}$ can lead to atrial fibrillation. Diness et al. (2015) have shown that inhibition of $I_{K,Ca}$ resulted in the termination of atrial fibrillation in guinea pigs, rabbits, and rat hearts. On the other hand, knock out of $I_{K,Ca}$ has been shown to be pro-arrhythmic (Li et al., 2009). Further studies are necessary to investigate the role of $I_{K,Ca}$ current in mechanisms of atrial arrhythmias.

2.3.5 Sensitivity Analysis: On Mice and Men

To evaluate the model performance for multiple atrial cells, in which the conductance of ionic currents can vary from cell to cell, we performed a sensitivity analysis. In these simulations, we increased and decreased each of the model ionic currents by 20% and investigated the parameters of the resulting APs and $[Ca^{2+}]_i$ transients. A similar analysis was performed by Sobie using the Kurata et al.'s model of the human ventricular myocytes (Kurata et al., 2005; Sobie, 2009) and by Kernik et al. for the human-induced pluripotent stem cell-derived cardiomyocytes (iPSC-CMs) (Kernik et al., 2019). In addition, Grinshpon and Bondarenko (2016) performed a sensitivity analysis with a 5% increase in the conductance of major ionic currents for the model of mouse ventricular myocytes.

Our mouse atrial mathematical model simulations illuminated major players affecting APD_{25} and APD_{50}: $I_{Kto,f}$, I_{Kslow1}, I_{Kslow2}, and I_{CaL}. These currents are also the major contributing factors to APD_{25} and APD_{50} in mouse ventricular myocytes (Grinshpon and Bondarenko, 2016), where I_{Kur} stands for I_{Kslow1} and I_{Kslow2}. For APD_{90}, the major contributing currents only partially overlap between mouse atrial and ventricular myocytes. The similar major players are I_{K1} and I_{Kur} (or sum of I_{Kslow1} and I_{Kslow2} in mouse atrial myocytes) and, to a lesser extent, I_{NaCa}. However, in mouse ventricular myocytes, an additional contribution to APD_{90} comes mostly from I_{CaL} and I_{NaK}, while in mouse atrial myocytes I_{CaT}, I_{Kss}, I_{Na}, and I_{Nab} contribute the most. Interestingly, I_{CaL}, I_{K1}, and I_{Kr} are the major APD_{90} affecting currents in iPSC-CMs, and two of them overlap with mouse ventricular myocytes (Grinshpon and Bondarenko, 2016; Kernik et al., 2019). I_{CaL} and I_{K1} currents were also among the major players in the Kurata et al. (2005) model of human ventricular myocytes, together with I_{Kr}, I_{Ks}, I_{NaCa}, and I_{NaK} currents (Sobie, 2009). Taken together, we can observe similarities in the major role of I_{K1} in APD_{90} both for mice and men, regardless of the myocyte type (atrial, ventricular). In mouse atrial myocytes, the effect of I_{CaL} is replaced by I_{CaT}, but I_{CaL} is still one of the major players in mice and men ventricular myocytes. It can also be suggested that the role of I_{Kr} in the human ventricular myocytes is similar to the role of I_{Kur} in the mouse ventricular myocyte model (or the sum of I_{Kslow1} and I_{Kslow2} in the mouse atrial cell model).

In both mouse's atrial and ventricular myocytes, AP amplitude depends mainly on the four ionic currents, I_{Na}, I_{Nab}, I_{K1}, and I_{NaK} (this study and Grinshpon and Bondarenko (2016)). Two of these currents, I_{Na} and I_{K1}, also provided significant contributions to the changes in AP amplitude for iPSC-CMs (Kernik et al., 2019).

Finally, our sensitivity analysis demonstrated the major contributing currents to the change in $[Ca^{2+}]_i$ in mouse atrial myocytes. The outstanding contributor is the L-type Ca^{2+} current (Fig.

2.11), which is also the outstanding contributor for the models of a mouse (Grinshpon & Bondarenko, 2016) and human (Sobie, 2009) ventricular myocytes. Other major contributing currents for the mouse atrial myocyte model are I_{NaCa}, I_{Cab}, I_{NaK}, and I_{Nab}. When compared to the Kurata et al. human ventricular cell model (Kurata et al., 2005; Sobie, 2009), the currents contributing to $[Ca^{2+}]_i$ change are essentially the same as for the mouse atrial myocytes (i.e., I_{NaCa}, I_{NaK}, and I_{Cab}). This result gives an interesting conclusion about the similarity in the regulation of $[Ca^{2+}]_i$ in the mouse atrial and human ventricular myocytes.

2.3.6 Model Limitations

While we developed a quite comprehensive mathematical model of mouse atrial myocytes that describes a significant amount of experimental data well, it has several limitations. First, the model was developed for right atrial myocytes with the developed TATS and cannot be applicable to atrial myocytes without TATS. Second, the model has a limited number of compartments related to Ca^{2+} dynamics (dyadic space, bulk cytosol, and sarcoplasmic reticulum) and β-adrenergic signaling system (caveolae, extracaveolae, cytosol). Therefore, it does not account for the effects of submembrane Ca^{2+} concentration in detail. At the same time, the model takes them into account through the "effective" parameters of the ionic currents and transporters. Third, not all model parameters were measured directly in experiments and thus were adjusted to fit the experimental data. Fourth, the model consists of several compartments described by ordinary differential equations; it does not include spatial effects that require partial differential equations.

3 MATHEMATICAL MODEL OF MOUSE VENTRICULAR MYOCYTES WITH HEART FAILURE

3.1 Materials and Methods

To develop a mathematical model of the failing ventricular myocytes, we used experimental data from the mouse ventricular myocytes after a procedure of TAC when the heart failure was evident by a significant change in ejection fraction to ~40% or heart fractional shortening to ~20% (Nie et al., 2019; Ljubojevic-Holzer et al., 2020). In most cases, it takes eight weeks or more for the mouse heart to develop heart failure after TAC.

3.1.1 Control Model Modifications

We modified a previously published compartmentalized mathematical model for ventricular myocytes from mice (Rozier & Bondarenko, 2017), which is based on the previously published models of mouse ventricular myocytes (Bondarenko et al., 2004; Petkova-Kirova et al., 2012; Bondarenko, 2014; Rozier & Bondarenko, 2017). The schematic drawing of the model is shown in Fig. 3.1.

First, the ultra-rapidly activating K^+ current, I_{Kur}, was reformulated to include two components, $I_{K,slow1}$ (encoded by $K_v1.5$ channels and also referred to as I_{Kur} component), and $I_{K,slow2}$ (encoded by $K_v2.1$ channels). The currents $I_{K,slow1,}$ and $I_{K,slow2}$ demonstrate a different response to the activation of β_1- and β_2-adrenergic signaling systems (Kodirov et al., 2004**;** Wilson et al., 1994; Zhou et al., 2003; Zhou et al., 2012; Asfaw et al., 2020) (Appendix B). These currents have approximately equal amplitudes in mouse ventricular myocytes (Zhou et al., 2003). The effect of PKA on $K_v2.1$ is quite small, as it was shown experimentally (Wilson et al., 1994; Zhou et al., 2012). Therefore, only $I_{K,slow1}$ is affected by isoproterenol in our revised mathematical model. The response of the model currents $I_{K,slow1,}$ and $I_{K,slow2}$ to a 200 ms depolarization pulse from a holding

potential –80 mV to +40 mV is shown in Fig. 3.2A. In the simulated results, we see an increase in $I_{K,slow1}$ magnitude upon the application of 1 μM isoproterenol, while $I_{K,slow2}$ is unchanged.

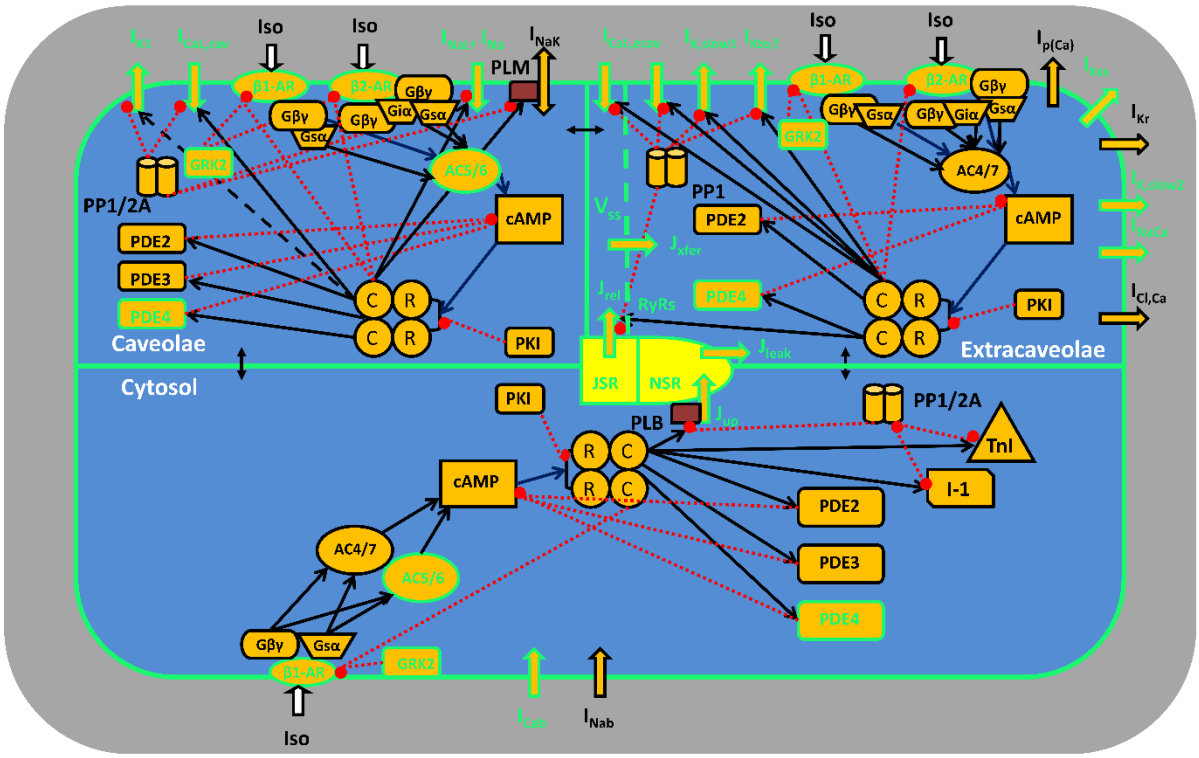

Figure 3.1 *A schematic representation of the mouse ventricular myocyte.*

The cell consists of three compartments (caveolae, extracaveolae, and cytosol) related to the combined β_1- and β_2-adrenergic signaling systems. The subspace volume (V_{ss}) is localized in the extracaveolar compartment. The biochemical portions of the combined β_1- and β_2-adrenergic signaling systems are the β_1-adrenergic receptors (β_1-AR), the β_2-adrenergic receptors (β_2-AR), the α-subunit of stimulatory G-protein ($G_{s\alpha}$), the α-subunit of inhibitory G-protein ($G_{i\alpha}$), the βγ-subunit of G_s and G_i ($G_{\beta\gamma}$), the adenylyl cyclases (AC5/6 or AC4/7, respectively), the phosphodiesterase (PDE2, PDE3, or PDE4, respectively), the cyclic AMP (cAMP), regulatory (R) and catalytic (C) subunits of protein kinase A, the protein kinase A inhibitor (PKI), the G-protein-coupled receptor kinase (GRK2), the protein phosphatases (PP1 and PP2A, respectively), the inhibitor-1 (I-1). Targets of the combined β_1- and β_2-adrenergic signaling systems are in the caveolae (including the fast Na^+ current (I_{Na}), the late Na^+ current (I_{NaL}), the L-type Ca^{2+} current ($I_{Ca,L,cav}$), the Na^+/K^+ pump (I_{NaK}), regulated by phospholemman (PLM), phosphodiesterases PDE2-PDE4, and the time-independent K^+ current (I_{K1})), the extracaveolae (including the L-type Ca^{2+} current ($I_{Ca,L,ecav}$, two equal components, one inside V_{ss}, one outside V_{ss}), the rapidly recovering transient outward K^+ current ($I_{Kto,f}$), the rapidly activating, slowly inactivating K^+ current ($I_{K,slow1}$, encoded by $K_v1.5$; 4-AP-sensitive), the rapidly activating, slowly inactivating K^+ current ($I_{K,slow2}$, encoded by $K_v2.1$; TEA-sensitive), ryanodine receptors (RyRs), and

phosphodiesterases (PDE2, PDE4)), and cytosol (including phospholamban (PLB), troponin I (TnI), and phosphodiesterases PDE2-PDE4). Stimulatory links are shown by black arrows and inhibitory links are shown by red dashed lines with balls of effectors. Other transmembrane currents are the sarcolemmal Ca^{2+} pump ($I_{p(Ca)}$, also known as plasmalemmal Ca^{2+}-ATPase, PMCA), the Na^+/Ca^{2+} exchanger (I_{NaCa}), the rapid delayed rectifier K^+ current (I_{Kr}), the non-inactivating steady-state voltage-activated K^+ current (I_{Kss}), and the Ca^{2+} and Na^+ background currents (I_{Cab} and I_{Nab}), which are not affected by the combined β_1- and β_2-adrenergic signaling systems. The Ca^{2+} fluxes are uptake of Ca^{2+} from the cytosol to the network sarcoplasmic reticulum (NSR) (J_{up}) by the SERCA pump, Ca^{2+} release from the junctional sarcoplasmic reticulum (JSR) (J_{rel}) through the RyRs, Ca^{2+} flux from the subspace volume to the cytosol (J_{xfer}), and Ca^{2+} leak from the SR to the cytosol (J_{leak}). $[Ca^{2+}]_i$, $[Na^+]_i$, and $[K^+]_i$ are the intracellular Ca^{2+}, Na^+, and K^+ concentrations in the caveolae, extracaveolae, and cytosol; $[Ca^{2+}]_o$, $[Na^+]_o$, and $[K^+]_o$ are the extracellular Ca^{2+}, Na^+, and K^+ concentrations. Proteins with characteristics that are modified in the mouse failing ventricular myocyte are shown in green. Modified from (Bondarenko, 2014).

Second, we added a dependence of the sarcoplasmic reticulum Ca^{2+} leak on the stimulation level of the β-adrenergic signaling system (Appendix B). Our simulations showed similar dependences of the concentration of catalytic subunit of PKA in the extracaveolar compartments ($[C]^{ecav}$) and the intracellular $[Ca^{2+}]_i$ transients, which reflects the SR Ca^{2+} load on the isoproterenol concentration. Therefore, we set a linear dependence of the leak rate ν_2 on $[C]^{ecav}$ as

$$\nu_2 = (1.2701 + 3.06045[C]^{ecav}) \cdot 10^{-2}\ (s^{-1}).$$

The numerical coefficients in this dependence were adjusted to fit the experimental data on the SR Ca^{2+} load without and with the application of the saturating isoproterenol concentration of 1 μM (Fig. 3.2B). It can be seen from Fig. 3.2B that the previously published model (Rozier & Bondarenko, 2017) gave a much higher increase in the SR Ca^{2+} load upon application of 1 μM isoproterenol as compared to the modified model, which agrees with the typical experimental data (Kashimura et al., 2010; Liu et al., 2011).

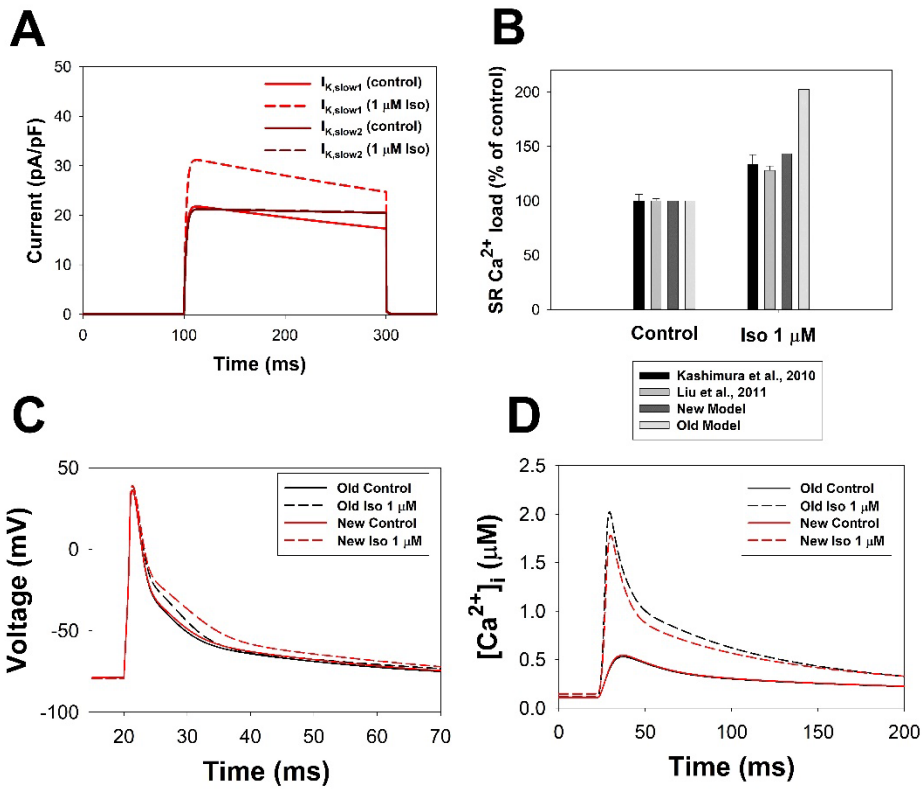

Figure 3.2 *The effect of $I_{K,slow1}$ and $I_{K,slow2}$ on the Ap and $[Ca^{2+}]_i$ under normal conditions and the application of isoproterenol.*
(A) *Current traces of $I_{K,slow1}$ and $I_{K,slow2}$ elicited by a 200-ms depolarization pulse to +40 mV applied to mouse control ventricular myocytes from the holding potential –80 mV at 100 ms. Simulations for control and after 10-minute exposure to 1 μM isoproterenol are shown by solid and dashed lines, respectively.* ***(B)*** *Increase in the SR Ca^{2+} load after 300-s application of 1 μM isoproterenol. Model data are shown for a stimulation frequency of 1 Hz; experimental data by Liu et al. (2011) and Kashimura et al. (2010) were obtained at 1 Hz and 0.5 Hz, respectively.* ***(C)*** *Simulated mouse ventricular action potentials for control (solid line) and after a 5-minute exposure to 1 μM isoproterenol (dashed line). Black lines correspond to the action potentials calculated by the Rozier & Bondarenko (2017) model (old model), red lines correspond to the modified model (new model) used as a control model in this paper.* ***(D)*** *Simulated $[Ca^{2+}]_i$ transients for control (solid line) and after a 5-minute exposure to 1 μM isoproterenol (dashed line). The colors are the same as in panel D.*

Third, we incorporated the late Na^+ current, I_{NaL}, in the model due to its possible important role in the failing ventricular myocytes. We assume that I_{NaL} is produced by the cardiac Na^+ channel isoform ($Na_V1.5$), operating in special gating modes (Maltsev & Undrovinas, 2008). Figure 3.3 demonstrates the experimental normalized current-voltage (Fig. 3.3A) and steady-state

inactivation (Fig. 3.3B) relationships, as well as voltage dependence of normalized conductance G/G_{max} (Fig. 3.3B). We adjusted the Hund-Rudy model of I_{NaL} (Hund & Rudy, 2004) (Table 3.1) to fit the experimental data for mice, which are shown in Fig. 3.3A-B. Because of the low accuracy of the measurements of the magnitude of I_{NaL}, we used the average from five experimental data to define the model conductance of the current in control and the average of two experimental data on the effects of saturating concentrations of isoproterenol (Fig. 3.3C). Finally, our model fits the kinetics of I_{NaL} upon application of isoproterenol, as shown in Fig. 3.3D.

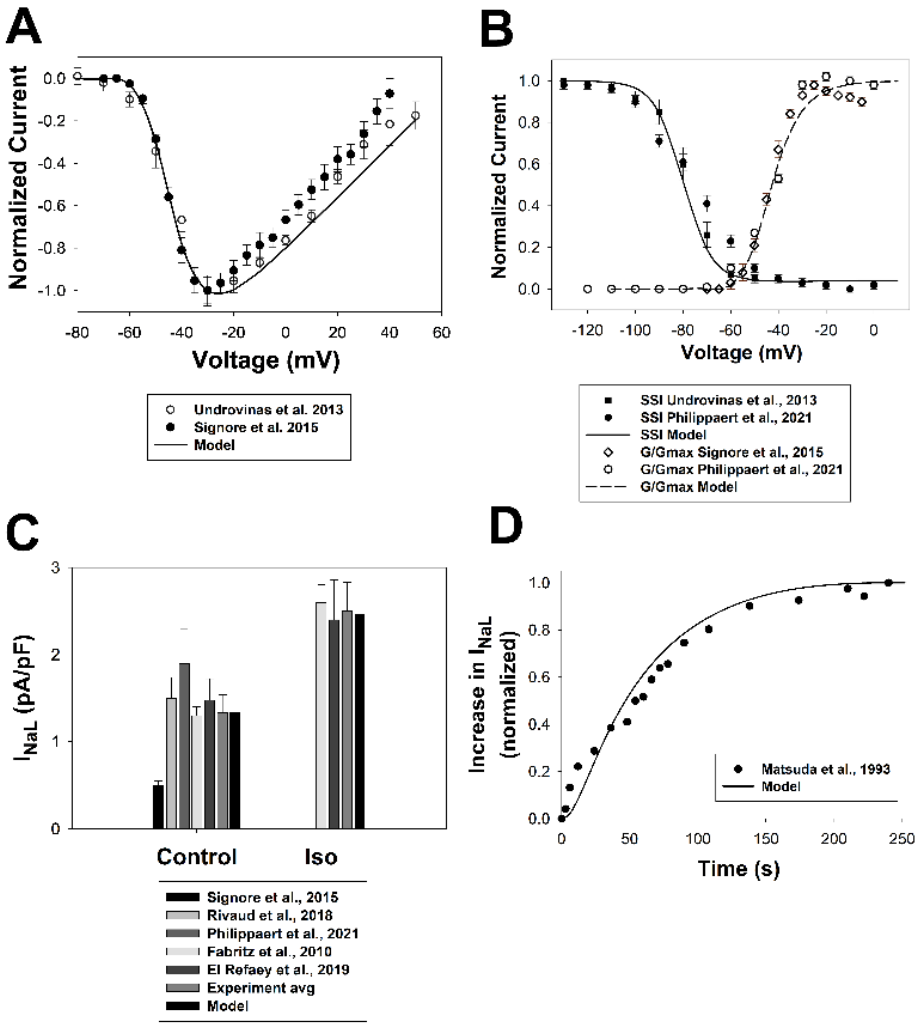

Figure 3.3 *The late Na^+ current I_{NaL} in mouse ventricular myocytes.*

*(**A**) Normalized current-voltage relationships. Experimental data shown by symbols with error bars were obtained by Signore et al. (2015) for mice and by Undrovinas et al. (2013) for dogs. Simulated data are shown by solid lines (data are obtained by two-pulse protocol, holding potential is –140 mV, first pulse duration is 2000 ms for voltages from –140 to +50 mV in 10 mV steps, the second pulse duration is 100 ms at a voltage –30 mV). (**B**) Steady-state inactivation and normalized conductance G/G_{max}. Experimental data shown by symbols with error bars were obtained by Philippaert et al. (2021) and Signore et al. (2015) for mice and by Undrovinas et al. (2013) for dogs. Filled and unfilled symbols plot experimental data for steady-state inactivation and normalized conductance G/G_{max}, respectively. Simulation data for steady-state inactivation and normalized conductance G/G_{max}, are shown by the solid and dashed lines, respectively. (**C**) The maximum amplitudes of the late Na^+ current. Experimental data for control by Signore et al. (2015), Rivaud et al. (2018), Philippaert et al. (2021), Fabritz et al. (2010), El Refaey et al. (2019), and averaged experimental data are shown by error bars; simulation data for control is shown by a bar without errors. Experimental data after the application of isoproterenol (Iso) by Fabritz et al. (2010) (1 μM isoproterenol) and El Refaey et al. (2019) (100 nM isoproterenol) and the averaged experimental data are shown by error bars. Simulation data after the application of 1 μM isoproterenol is shown by a bar without errors bars. (**D**) Time course of the activation of the fast Na^+ current upon application 0.1 μM isoproterenol. Experimental data from Matsuda et al. (1993) obtained for the normalized peak I_{Na} in rabbit ventricular myocytes is shown by closed circles. Data is obtained with 40-ms pulses from a holding potential of –100 mV to –30 mV at a stimulation frequency of 0.2 Hz. A solid line shows the time course of simulated data on relative I_{Na} phosphorylation upon application of 0.1 μM isoproterenol.*

These modifications did not significantly change model action potential and $[Ca^{2+}]_i$ transient in control but significantly changed their response to isoproterenol (Fig. 3.2C-D). The action potential demonstrated larger prolongation by the revised control model, which fits better with the typical experimental data after isoproterenol application (Tong et al., 2006; Wang et al., 2008). The revised model also demonstrates a smaller increase in $[Ca^{2+}]_i$ transient when compared to the previous model by Rozier & Bondarenko (2017) due to the higher Ca^{2+} leak from the SR and smaller SR load after isoproterenol application. These observations are consistent with most experimental findings (see, for example, Kashimura et al., 2010; Liu et al., 2011; Wang et al., 2008).

Table 3.1 *Differences between the models of mouse ventricular myocytes from control (sham) hearts and the hearts with heart failure after TAC.*

Parameter	Definition	Control	Heart failure
V^{cell}	Cell volume	38.00×10^{-6} µl	68.40×10^{-6} µl
V^{cyt}	Cytosolic volume	25.84×10^{-6} µl	47.71×10^{-6} µl
V_{JSR}	Junctional SR volume	0.1200×10^{-6} µl	0.1512×10^{-6} µl
V_{NSR}	Network SR volume	2.098×10^{-6} µl	2.6435×10^{-6} µl
V_{ss}	Subspace volume	1.485×10^{-9} µl	1.8700×10^{-9} µl
A_{cap}	Capacitive membrane area	1.534×10^{-4} cm^2	2.1282×10^{-4} cm^2
v_1	Maximum RyR channel Ca^{2+} permeability	4,500 s^{-1}	5,625 s^{-1}
v_3	SR Ca^{2+}-ATPase maximum pump rate	3.0600×10^{-4} µM s^{-1}	2.3562×10^{-4} µM s^{-1}
τ_{xfer}	The time constant for transfer from subspace to the cytosol	8.0 ms	16.0 ms
k_a^+	RyR $P_{C1} - P_{O1}$ rate constant	6.075 μM^{-4} s^{-1}	1.215 μM^{-4} s^{-1}
k_b^+	RyR $P_{O1} - P_{O2}$ rate constant	4.05 μM^{-3} s^{-1}	0.81 μM^{-3} s^{-1}
k_c^+	RyR $P_{O1} - P_{C2}$ rate constant	9.0 s^{-1}	1.8 s^{-1}
k_{cp}^+	RyR $P_{O1p} - P_{C2p}$ rate constant	$\mathbf{50}k_c^+$	$\mathbf{5}k_c^+$
k_{cp}^-	RyR $P_{C2p} - P_{O1p}$ rate constant	$\mathbf{30}k_c^-$	$\mathbf{3}k_c^-$
G_{Na}	Specific maximum conductivity for the fast Na^+ channel (non-phosphorylated)	14.4 mS/µF	10.08 mS/µF

G_{Nap}	Specific maximum conductivity for the fast Na^+ channel (phosphorylated)	18.0 mS/μF	12.6 mS/μF
$G_{Kto,f}$	Specific maximum conductivity for the rapidly inactivating transient outward K^+ current (non-phosphorylated)	0.3846 pA/pF	0.2115 pA/pF
$G_{Kto,fp}$	Specific maximum conductivity for the rapidly inactivating transient outward K^+ current (phosphorylated)	0.3846 pA/pF	0.2115 pA/pF
$G_{K,slow1}$	Maximum conductance for the rapidly activating, slowly inactivating K^+ current (encoded by Kv1.5, non-phosphorylated)	0.1712 mS/μF	0.0856 mS/μF
$G_{K,slow1p}$	Maximum conductance for the rapidly activating, slowly inactivating K^+ current (encoded by Kv1.5, phosphorylated)	0.26654 mS/μF	0.1333 mS/μF
$G_{K,slow2}$	Maximum conductance for the rapidly activating, slowly inactivating K^+ current (encoded by Kv2.1, non-phosphorylated)	0.1712 mS/μF	0.0856 mS/μF
G_{Kss}	Maximum conductance for the noninactivating steady-state K^+ current	0.0611 mS/μF	0.04583 mS/μF
G_{K1}	Maximum conductance for the time-independent K^+ current	0.27 mS/μF	0.2025 mS/μF
G_{Cab}	Maximum background Ca^{2+} current conductance	0.000284 mS/μF	0.0005112 mS/μF
G_{NaL}	Maximum conductance for the late Na^+ current (non-phosphorylated)	0.01451 mS/μF	0.020314 mS/μF
G_{NaLp}	Maximum conductance for the late Na^+ current (phosphorylated)	0.03101 mS/μF	0.043414 mS/μF

τ_{NaL}	Inactivation time constant for the late Na^+ current	0.6 s	0.6 s
k_{NaCa}	Scaling factor for Na^+/Ca^{2+} exchanger	275 pA/pF	495 pA/pF
$[R_{\beta 1}]_{tot}$	Total β_1-adrenoceptor concentration	0.0103 μM	0.00515 μM
$f_{\beta 2}^{cav}$	Fraction of β_2-adrenoceptors located in caveolae	0.99	0.5
k_{GRK2+}	Rate of GRK2 phosphorylation of β_1- and β_2-adrenoceptors	0.000243 s^{-1}	0.0005589 s^{-1}
k_{GRK2+}	Rate of GRK2 dephosphorylation of β_1- and β_2-adrenoceptors	0.0002025 s^{-1}	0.00046575 s^{-1}
$[AC]_{tot}$	Total cellular AC concentration	0.02622 μM	0.02079 μM
$f_{AC56,AC47}$	Fraction of AC that is of type 5 or 6	0.74	0.672
$[PDE4]_{tot}$	Total cellular concentration of PDE4	0.026687 μM	0.0133435 μM

3.1.2 Myocyte Geometry

Experimental data showed that TAC resulted in a significant change in the cell geometry, specifically, increased myocyte size when the heart progressed to heart failure (Rivaud et al., 2017; Bryant et al., 2018; Tamayo et al., 2020). This increase was measured either directly by confocal microscope (Bryant et al., 2018) or by measurements of the cell capacitance assuming linear dependence between the cell volume and cell capacitance (Rivaud et al., 2017; Tamayo et al., 2020). The average data from these measurements gave the failing myocyte volume increase by a factor of ~1.8 compared to the sham myocyte.

Progression to heart failure also led to myocyte dyadic space structure and content changes. The lengths of junctions in failing ventricular myocytes were decreased by 30%, and the volume

density of junctional SR was reduced by 31.6% (Wu et al., 2012). Similar data were obtained by Li et al. (2013), where the volume density of t-tubules coupled to JSR was decreased by ~30%, and the lengths of junctions in failing ventricular myocytes were decreased by ~25%. However, this decrease is not accompanied by the change in the distance between RyRs and t-tubules (van Oort et al., 2011). The experimental data also demonstrated that the volume density of mitochondria did not change in the failing myocytes compared to the control (LaRocca et al., 2020).

Therefore, in our model, we increased myocyte size by a factor of 1.8, from $38.0 \cdot 10^{-6}$ μl to $68.4 \cdot 10^{-6}$ μl. In this case, the capacitive area, which is twice larger than the geometric area, is increased by a factor of 1.4 only, from $1.534 \cdot 10^{-4}$ cm^2 to $2.1282 \cdot 10^{-4}$ cm^2. As a 30% volume density reduction of junctions occurs in the cells that increase in volume by a factor of 1.8, the volumes of junctional SR and subspace volume V_{ss} were increased by a factor of 1.26 in failing myocytes. We also increased the volume of network SR by a factor of 1.26. While mitochondria volume density did not change in the failing myocytes, its volume increased by a factor of 1.8. This resulted in an increase in cytosolic volume by a factor ~1.84635, from $25.84 \cdot 10^{-6}$ μl to $47.71 \cdot 10^{-6}$ μl. The model geometries for control and failing ventricular myocytes are shown in Table 3.1.

3.1.3 Redistribution in Microdomains

Experimental data demonstrate changes in the myocyte geometry and the redistribution of the cellular proteins, specifically, the L-type Ca^{2+} channels and β_2-adrenergic receptors, in the failing myocytes as compared to control.

Consider first the L-type Ca^{2+} channels. Experimental microstructure and physiological data on the localization of the L-type Ca^{2+} channels in atrial and ventricular myocytes

demonstrated that they moved outside of the dyadic space when heart failure developed (Wu et al., 2012; Glukhov, Balycheva, et al., 2015; Bryant et al., 2018). However, the majority of experiments did not show a decrease in the total cellular I_{CaL} in either rat or mouse failing myocytes (van Oort et al., 2011; Wu et al., 2012; Li et al., 2013; Bryant et al., 2015; Tamayo et al., 2020). They demonstrated mainly the re-distribution of I_{CaL} from t-tubules to the surface. Based on these observations, we did not change the total cellular I_{CaL} in our model for failing myocytes, but we re-distributed I_{CaL} leaving 50% in the dyadic space and moving 50% to extracaveolae domain outside the dyadic space (Fig. 3.1).

Further, we considered the re-distribution of β_2-adrenergic receptors (β_2-ARs). Experimental data (Nikolaev et al., 2010; Wright et al., 2014) with ventricular myocytes demonstrated that most of β_2-ARs in the healthy mouse and rat hearts are localized in the t-tubules (caveolae domain in our model). However, in the failing hearts, β_2-ARs are re-distributed to the cell crest (extracaveolae in our model) with approximately equal densities in t-tubules and cell crest. In addition, the application of PTX did not change cAMP generation from β_2-ARs in the crest region, indicating that G_i proteins are not re-distributed from t-tubules to the crest. Therefore, in our model, we re-distributed β_2-ARs to have 50% in caveolae and 50% in extracaveolae and did not change the distribution of G_i proteins.

3.1.4 Ion Current Modifications

In the model, we reduced the fast Na^+ current (normalized to the cell capacitance) in failing myocytes by 30% compared to control (sham) myocytes, according to the experimental data by Rivaud et al. (2017) in mouse heart failure after 6 weeks TAC. Experimental data also showed that the channel gating (activation, normalized conductance G/G_{max}, steady-state inactivation, and recovery from inactivation) was not changed. In the experiments, the late Na^+ current was

increased by ~40% in failing myocytes compared to sham (Glynn et al., 2015; Philippaert et al., 2021). Therefore, we increased I_{NaL} in the failing myocytes model by 40%.

The L-type Ca^{2+} current I_{CaL} was not changed after TAC in the failing myocytes, but we re-distributed I_{CaL} in the extracaveolae compartment to allow 50% of the current to enter into dyadic space (V_{ss}) and 50% of the current into extracaveolae compartment, but outside the dyadic space (Bryant et al., 2018).

The rapidly recovering transient outward K^+ current $I_{Kto,f}$ was found to be reduced in failing ventricular myocytes by 45% compared to sham cells (Tamayo et al., 2020). Experimental data from sham mice and mice after 9 weeks of TAC demonstrated a decrease in the sum of $I_{K,slow1,}$ and $I_{K,slow2}$ by ~50% (Tamayo et al., 2020). In the model, we decreased the conductance of both currents by 50% as well. According to the experimental data, the steady-state non-inactivating K^+ current I_{Kss} was reduced only by 25% in TAC mice (Tamayo et al., 2020). We also reduced the time-independent K^+ current, I_{K1}, by 25% to fit the experimental data from sham and TAC mouse ventricular myocytes (Marionneau et al., 2008). However, the data on I_{K1} by Marionneau et al. (2008) was obtained only after one week of TAC, and no data is available for the longer time after TAC.

Experimental data showed that the expression of the protein responsible for the Na^+/Ca^{2+} exchanger was increased by ~90±30% after eight weeks of TAC (Lu et al., 2011). We increased I_{NaCa} by 80% in our failing myocyte model to keep the change within the experimental error and to fit the SR Ca^{2+} load data. We also increased the background Ca^{2+} current I_{Cab} by a factor of 1.8 in the failing cells to compensate for the Ca^{2+} loss due to an increased function of I_{NaCa} by the same factor in failing cardiomyocytes and to keep a similar diastolic $[Ca^{2+}]_i$ concentration, as it was observed in most experimental data of the failing hearts with reduced ejection fraction (Eisner et

al., 2020). No significant changes were observed in I_{NaK} pump in the experiments (Wansapura et al., 2011; Correll et al., 2014); therefore, we did not change the current in the failing myocyte model.

3.1.5 Modifications of Ca^{2+} Handling Proteins

Experimental data with mice shows that heart failure leads mostly to modification of the expression of SERCA pump, which is decreased on average to 70.2±8.2% in mice with heart failure as compared to sham mice (Ito et al., 2000; Lu et al., 2011; Vinet et al., 2012; Tamayo et al., 2020). Ventricular myocytes from TAC mice also demonstrate increased Ca^{2+} leak from the SR by ~30% (van Oort, Respress, et al., 2010); however, the author claimed that the change was not significant. The phospholamban, calsequestrin, and ryanodine receptors expressions do not significantly change in TAC mice (Kho et al., 2011; Vinet et al., 2012). Collectively, these changes resulted in a reduction of the SR content on average to 83±16% as compared to sham mice (Bryant et al., 2018; Nie et al., 2019; Tamayo et al., 2020) and decreased $[Ca^{2+}]_i$ transients on average to 72.8±7.0% (experimental data from different sources varied from 65% to 87% decrease) (Li et al., 2013; Nie et al., 2019; Cai et al., 2019; Tamayo et al., 2020; Ljubojevic-Holzer et al., 2020; Chen et al., 2020).

To simulate these changes in Ca^{2+} handling proteins in failing myocytes, we decreased the SR Ca^{2+} maximum pump rate in failing myocytes to 77% of its control value to stay within the experimental range (Ito et al., 2000; Lu et al., 2011; Vinet et al., 2012; Tamayo et al., 2020). Ca^{2+} SR leak rate constant was increased by a factor of 1.15 for the heart failure model to account for the intermediate value between 0% and 30% observed by van Oort, Respress, et al. (2010). We also changed several rate constants responsible for RyR gating and the time constant for Ca^{2+}

transfer from subspace to myoplasm τ_{xfer} to simulate delayed Ca^{2+} release (see Table 3.1), as was observed in the experiments (Ljubojevic-Holzer et al., 2020).

3.1.6 Modifications of β-adrenergic Signaling System

Experimental data on the mouse hearts and the hearts of other species demonstrate a decrease in the expression of β_1-adrenoceptors but no significant change in the expression of β_2-adrenoceptors in the failing hearts (Pelá et al., 1990; Ungerer et al., 1993; Yoo et al., 2009; Norman, 2016). We used the data by (Esposito et al., 2002; Nienaber et al., 2003; Tachibana et al., 2005) to evaluate a decrease in the expression of β_1-adrenoceptors in the failing mouse hearts after TAC. However, these data presented only a decrease in the total β_1- and β_2-adrenoceptor densities. Therefore, for estimation purposes, we assumed that the density of β_1-adrenoceptors is two-fold higher than the β_2-adrenoceptor density in control (Hilal-Dandan et al., 2000), and heart failure does not change the density of β_2-adrenoceptors. Our estimations from the data by (Esposito et al., 2002; Nienaber et al., 2003; Tachibana et al., 2005) showed that the density of β_1-adrenoceptors should decrease to 51.5% of the control value, which is consistent with a percentage of decrease in other species (Pelá et al., 1990; Ungerer et al., 1993). Therefore, in the failing mouse ventricular myocytes model, we decreased the density of β_1-adrenoceptors by 2-fold and did not change the density of β_2-adrenoceptors. We also did not change the density of G_s and G_i proteins following the data by (Feldman et al., 1988) for humans and by (Norman 2016) for mice.

Experimental data on adenylyl cyclase activity in mice showed a decrease in the activities of AC5/6 in the failing hearts to 72±13% without application of isoproterenol and to 60±12% after application of 1 μM isoproterenol as compared to control myocytes (Esposito et al., 2002; Nienaber et al., 2003; Tachibana et al., 2005). Experimental data on PDE activities showed that only PDE4 decreased activity in the mouse failing hearts by 2-fold after eight weeks of TAC (Sprenger et al.,

2015). The activities of PDE2 and PDE3 did not change significantly. In addition, the activity of GRK2 increased in the failing mouse hearts by 2.3-fold as compared to control (Esposito et al., 2002). The activities of PKA, PP1 and PP2A did not change after TAC (Perino et al., 2011; Grote-Wessels et al., 2008). We used these numbers for the model development.

First, we reduced AC5/6 activity in failing myocytes to 72% of its control value, which reduced total AC activity and fraction of AC5/6 (see Table 3.1). We also reduced PDE4 concentration by 2-fold and increased GRK2 activity by 2.3-fold.

The following differential equation describes the resulting model for the AP:

$$\frac{dV}{dt} = -\frac{1}{C_m}(I_{CaL} + I_{p(Ca)} + I_{NaCa} + I_{Cab} + I_{Na} + I_{NaL} + I_{Nab} + I_{NaK} + I_{Kto,f} + I_{K1} + I_{K,slow1} + I_{K,slow2} + I_{Kss} + I_{Kr} + I_{Cl,Ca} - I_{stim})$$

where I_{CaL} is the L-type Ca^{2+} current, $I_{p(Ca)}$ is the sarcolemmal Ca^{2+} pump, I_{NaCa} is the current from the Na^+/Ca^{2+} exchanger, I_{Cab} is the Ca^{2+} background current, I_{Na} is the fast Na^+ current, I_{NaL} is the late Na^+ current, I_{Nab} is the Na^+ background current, I_{NaK} is the current of the Na^+-K^+ pump, $I_{Kto,f}$ is the rapidly recovering transient outward K^+ current, I_{K1} is the time-independent K^+ current, $I_{K,slow1}$ is the rapidly activating, slowly inactivating K^+ current (encoded by $K_v1.5$; 4-aminopyridine-sensitive; also named as I_{Kur}, the ultra-rapidly activating delayed rectifier K^+ current), $I_{K,slow2}$ is the rapidly activating, slowly inactivating K^+ current (encoded by $K_v2.1$; TEA-sensitive), I_{Kss} is the non-inactivating steady-state voltage-activated K^+ current, I_{Kr} is the rapid delayed rectifier K^+ current, $I_{Cl,Ca}$ is the Ca^{2+}-activated chloride current, and I_{stim} is the stimulus current.

3.1.7 Simulation Methods

The model equations were solved by a fourth-order Runge-Kutta method, with two different time steps. A relatively small time step of 0.000002 ms was used during a 15-millisecond interval after the initiation of the stimulus current; for all other times, we used the time step 0.0001 ms. Simulation of the cellular behavior without electrical stimulation was performed with a time step of 0.1 ms. The model equations were implemented in FORTRAN 90. All simulations were performed on a single processor under SUSE Linux 11 on a Dell Precision Workstation T3500 with a six-core Intel Xeon CPU W3670 (3.2 GHz, 12 GB RAM) or on the ARCTIC supercomputer cluster at Georgia State University. The model was developed for a room temperature of 25ºC (T = 298ºK). Initial conditions were obtained by running the program code without electrical stimulations for about 10,000 seconds to ensure quasi-steady-state. APs and $[Ca^{2+}]_i$ transients were initiated by a stimulus current (I_{stim} = 80 pA/pF, τ_{stim} = 1 ms) with different frequencies from 0.25 to 5 Hz (electrical stimulation).

3.2 Results

In this part of the dissertation, we developed a new compartmentalized mathematical model of failing mouse ventricular myocytes after TAC and compared model behavior with the corresponding model for control conditions.

3.2.1 Adenylyl Cyclase Activity in Control and Failing Mouse Ventricular Myocytes

First, we simulated adenylyl cyclase activities in control and failing mouse ventricular myocytes (Fig. 3.4). It is seen from Fig. 3.4A that the failing myocytes demonstrate a decrease in the cellular AC activity as compared to control at all isoproterenol concentrations, from 0.1 nM to 10 μM. We also compared the ratio of the cellular AC activities for failing to control myocytes ($AC_{HF}/AC_{Control}$) without and with isoproterenol application. Without isoproterenol, the ratio

$AC_{HF}/AC_{Control}$ was 0.67 and decreased to ~0.48 at 10-100 μM isoproterenol. Comparison of the simulated ratio $AC_{HF}/AC_{Control}$ with the experimental data for control and after application of 100 μM isoproterenol in Fig. 3.4B shows a good agreement within the experimental errors. We need to notice that the stimulation of the combined β_1- and β_2-adrenergic systems in failing myocytes demonstrate a reduced response to the adrenergic stimulation, as compared to control myocytes, which can also reduce the effects on different protein kinase A targets.

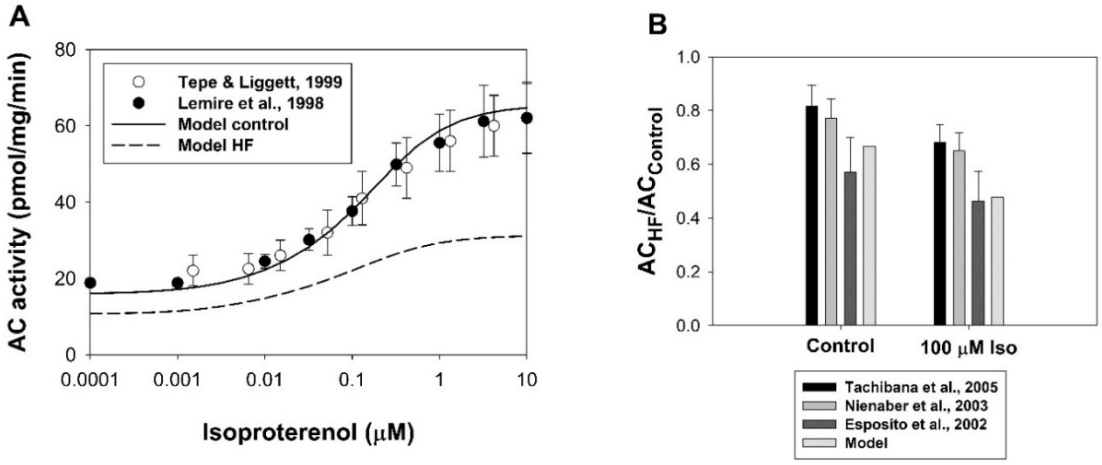

Figure 3.4 *Adenylyl cyclase dependency on* isoproterenol.
(A) *Adenylyl cyclase activity as a function of isoproterenol. Experimental data on AC activity (in pmol/mg/min) in mouse hearts and ventricular myocytes obtained after 10-minutes exposure to isoproterenol are shown by unfilled circles (Tepe & Liggett, 1999) and filled circles (Lemire et al., 1998). The solid and dashed lines show corresponding simulated AC activity at different concentrations of isoproterenol upon activation of both β_1-ARs and β_2-ARs in control and failing ventricular myocytes, respectively.* ***(B)*** *The effects of isoproterenol on adenylyl cyclase activity in control and failing myocytes. Experimental data on the ratio of AC activity in myocardial membranes from failing to control myocytes are obtained after exposure to 100 μM isoproterenol and are shown by bars with error bars (Tachibana, 2005; Nienaber, 2003; Esposito, 2002). The corresponding simulated data are shown by light gray bars when both β_1-ARs and β_2-ARs are activated.*

3.2.2 Compartmentalized cAMP and PKA Dynamics

One of the interesting results of our mathematical model is an increased role of β_2-adrenoceptors in the failing ventricular myocytes. To demonstrate the differences in the roles of β-adrenergic signaling systems in control and failing myocytes, we simulated compartmentalized

cAMP and PKA dynamics (Figs. 3.5 and 3.6). The β_1- and β_2-adrenergic systems were stimulated with 1 μM isoproterenol together and individually.

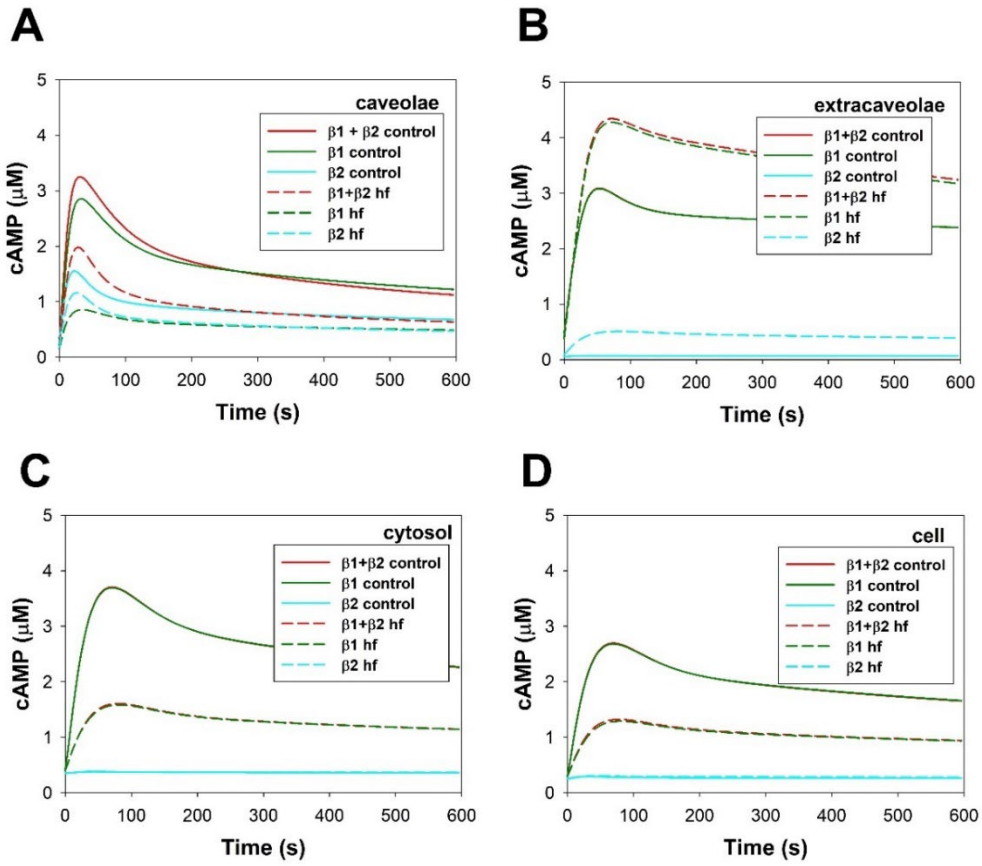

Figure 3.5 *cAMP dynamics in mouse ventricular myocytes.*
Simulated cAMP concentrations are shown as functions of time in the caveolar ***(A)*** *extracaveolar* ***(B)****, and cytosolic compartments* ***(C)****, as well as in the whole cell* ***(D)****. Simulations were performed for six cases: activation of both β_1-ARs and β_2-ARs in control, activation of β_1-ARs alone in control, activation of β_2-ARs alone in control, activation of both β_1-ARs and β_2-ARs in heart failure (hf), activation of β_1-ARs alone in heart failure (hf), activation of β_2-ARs alone in heart failure (hf). Data in (A-D) are obtained upon application of 1 μM isoproterenol.*

In the caveolar compartment, stimulation of the combined β_1- and β_2-adrenergic systems in the failing myocytes resulted in a smaller cAMP transient compared to control (Fig. 3.5A). Stimulation of only the β_1-adrenergic system in the failing myocytes led to a dramatic decrease in cAMP production due to the reduction in β_1-AR concentration. In contrast, a similar decrease in

β_2-ARs in the caveolar compartment due to their translocation to the extracaveolae compartment demonstrated a smaller decline. In the extracaveolar compartment, stimulation of the combined β_1- and β_2-adrenergic systems and β_1-adrenergic system alone does not show a remarkable difference in cAMP production both in failing and control myocytes (Fig. 3.5B). However, cAMP production in failing myocytes is greater than in control for both cases. There is also a difference in cAMP production between the failing and control myocytes upon stimulation of the β_2-adrenergic system alone. Figure 3.5B shows that the failing myocytes produced a significantly larger cAMP transient than control myocytes due to a much weaker connection of β_2-ARs to inhibitory G protein, G_i, in the extracaveolar compartment. Therefore, translocation of β_2-ARs to the extracaveolar compartment increases their contribution to β-adrenergic signaling in failing myocytes. Finally, in the cytosolic compartment, the cAMP transient is shown to be much smaller in the failing myocytes compared to control upon stimulation of the combined β_1- and β_2-adrenergic system or β_1-adrenergic system alone (Fig. 3.5C). Stimulating the β_2-adrenergic system alone does not produce a marked cAMP increase in the cytosolic compartment. Similar data were obtained for the whole-cell model (Fig. 3.5D).

The behavior of the catalytic subunit of PKA is similar to that of cAMP (Fig. 3.6). Stimulation of the combined β_1- and β_2-adrenergic signaling systems or β_1-adrenergic signaling system alone in the control cell leads to a similar, large increase of PKA activity in the caveolar and extracaveolar compartments but a smaller increase in the cytosol and whole cardiac cell (Fig. 3.6A-D, red and blue solid lines). However, in failing ventricular myocytes, stimulation of the combined β_1- and β_2-adrenergic signaling systems in the caveolae resulted in a larger PKA activity than the stimulation of the β_1-adrenergic signaling system alone (Fig. 3.6A). Stimulation of β_2-ARs alone in the failing myocytes demonstrated a smaller decrease in PKA activity than in control (Fig.

3.6A). In the extracaveolar compartment, a higher PKA activity was obtained upon stimulation of the combined β_1- and β_2-adrenergic signaling systems or β_1-adrenergic signaling system alone in the failing myocytes compared to control cells (Fig. 3.6B). Stimulation of β_2-ARs alone produces quite a significant effect on PKA activity in the extracaveolar compartment of the failing cell. In contrast, the control myocytes did not show a considerable change in their PKA activity (Fig. 3.6B, cyan lines). Stimulation of the combined β_1- and β_2-adrenergic signaling systems or β_1-adrenergic signaling system alone in the cytosol and the whole cell of control myocytes show higher PKA activities than those for the failing myocytes. In contrast, stimulation of β_2-ARs alone does not markedly affect the background PKA activity in both failing and control cells (Fig. 3.6C, D).

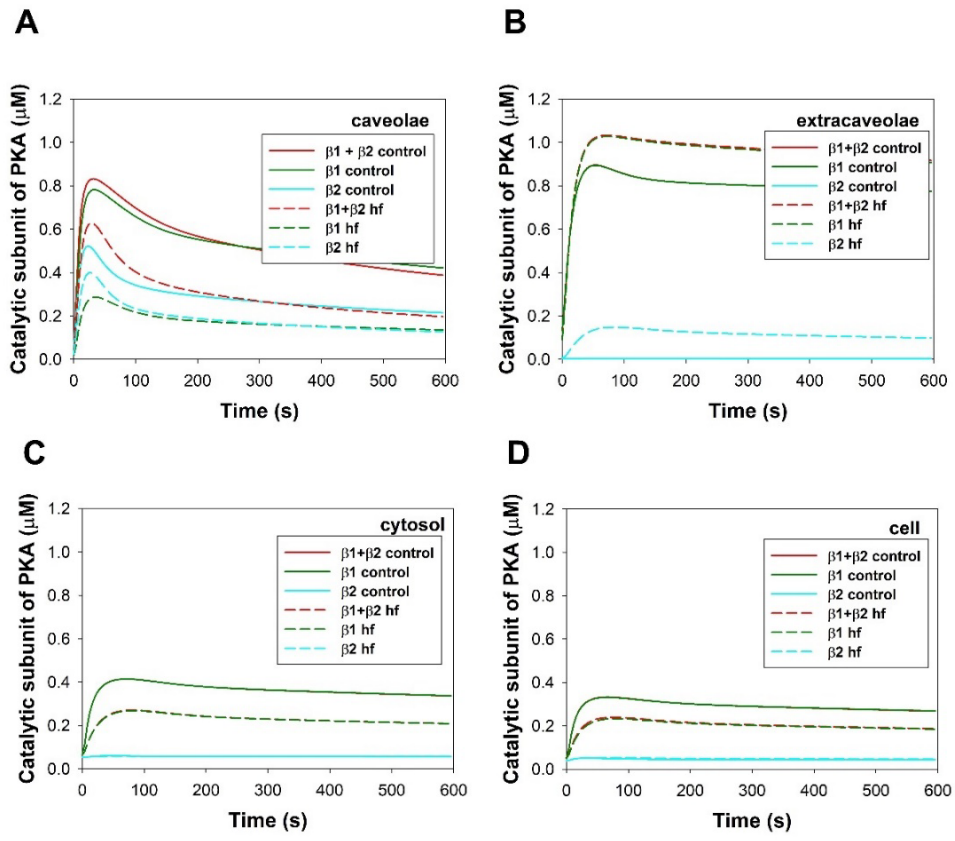

Figure 3.6 *PKA catalytic subunit dynamics in mouse ventricular myocytes.*
Simulated PKA catalytic subunit concentrations are shown as functions of time in the caveolar ***(A)****, extracaveolar* ***(B)****, and cytosolic compartments* ***(C)****, as well as in the whole cell* ***(D)****. Simulations were performed for six cases: activation of both β_1-ARs and β_2-ARs in control,*

activation of β_1-ARs alone in control, activation of β_2-ARs alone in control, activation of both β_1-ARs and β_2-ARs in heart failure (hf), activation of β_1-ARs alone in heart failure (hf), activation of β_2-ARs alone in heart failure (hf). Data in (A-D) are obtained upon application of 1 μM isoproterenol.

3.2.3 Mouse Failing and Control Ventricular Action Potentials, Ca^{2+} Dynamics, and Ionic Currents

Experimental data shows that the APs in mouse control and failing ventricular myocytes have different durations due to the differences in the magnitudes of repolarization currents (Toischer et al., 2013; Glynn et al., 2015; Mohamed et al., 2018; Bartoli et al., 2020). Some of the experimental data for APD_{20}, APD_{50}, APD_{75}, and APD_{90} are shown in Table 3.2. This data shows that the APs from the failing myocytes are more prolonged than those from control cells.

Our mathematical model reproduced the experimentally found AP durations at different levels of repolarization in control and failing mouse myocytes. Simulated APD_{25} for control myocytes is 1.71 ms which is slightly longer than the APD_{20} = 1.44±0.08 ms from the experimental data by Bartoli et al. (Bartoli et al., 2020). Simulated APD_{50} is 3.25 ms, which is comparable to the experimental data ~4.0-5.0 ms (Glynn et al., 2015; Bartoli et al., 2020) for control cells. Simulated APD_{90} = 28.86 ms is also close to the experimental values of 28.0 ms (range from 20 to 47 ms) (Glynn et al., 2015) and 34.5±6.0 ms (Bartoli et al., 2020) but somewhat shorter than the data by Toischer et al. (58±9 ms (Toischer et al., 2013)) and Mohamed et al. (60±5 ms (Mohamed et al., 2018)). Simulated APD_{25} for failing myocytes is equal to 2.44 ms, which is similar to APD_{20} = 2.89±1.0 ms from the experimental data by Bartoli et al. (Bartoli et al., 2020). Simulated APD_{50} is 5.65 ms, slightly less than the experimental data ~8-38 ms (Glynn et al., 2015; Bartoli et al., 2020) for the failing cells. Simulated APD_{90} = 86.82 ms is also within the experimental range from 55 ms to 138 ms (Toischer et al., 2013; Glynn et al., 2015; Mohamed et al., 2018; Bartoli et al., 2020) (See Table 3.2).

Table 3.2 *Experimental data on APDs in mouse control and failing ventricular myocytes (ms).*

	APD_{20}	**APD_{50}**	**APD_{75}**	**APD_{90}**
Control				
Toischer et al. (2013) 1 Hz				58±9
Mohamed et al. (2018)				60±5
Glynn et al. (2015)		4.0 (2.5-10)		28.0 (20-47)
Bartoli et al., (2020)	1.44±0.08	5.02±0.47		34.5±6.0
Heart Failure				
Toischer et al. (2013)				138±28
Mohamed et al. (2018)				130±15
Glynn et al. (2015)		22.0 (8-38)	50.0 (18-112)	55.0 (30-110)
Bartoli et al., (2020)	2.89±1.0	11.89±4.26		76.77±9.84

If we compare APD_{25}, APD_{50}, APD_{75}, and APD_{90} for simulated control and failing ventricular myocytes, we see that the AP durations at all levels of repolarizations are longer for the failing myocytes (Table 3.3). The difference ranges between 42.9% for APD_{25} and 200.9% for APD_{90}. These differences are explained by the differences in the major repolarization currents for control and failing ventricular myocytes obtained from the simulations (Figs. 3.7C and 3.7D). Failing myocytes have about twice smaller repolarizing rapidly recovering transient outward K^+ current, $I_{Kto,f}$, than control ventricular myocytes. The magnitudes of $I_{K,slow,}$ and I_{Kslow2} in failing cells are also much smaller compared to those in control myocytes. The difference in outward K^+ currents is partially compensated by the difference in the inward fast Na^+ current, which is smaller in the failing myocytes due to a larger inactivation at more depolarized resting potential, but this current affects only the initial stage of repolarization. The later repolarization stage is mainly affected by the precise balance of the time-independent K^+ current I_{K1}, the Na^+/Ca^{2+} exchanger current I_{NaCa}, the Na^+-K^+ pump current I_{NaK}, the late Na^+ current I_{NaL}, and the background currents I_{Cab} and I_{Nab} (Fig. 3.7E and 3.7F). The major differences between control and failing myocytes are

that the outward phase of I_{K1} is activated at later times, and the I_{NaL} is more prolonged in the failing cells.

Table 3.3 *Comparison of the simulated mouse ventricular action potential durations from control and failing hearts (ms).*

	Control myocyte	**Failing myocyte**	**APD prolongation (%) Failing vs. Control**
No Iso			
APD_{25}	1.71	2.44	42.7
APD_{50}	3.25	5.65	73.8
APD_{75}	10.06	19.48	93.6
APD_{90}	28.86	86.82	200.8
1 µM Iso			
APD_{25}	1.93	2.94	52.3
APD_{50}	4.40	8.50	93.2
APD_{75}	14.16	25.55	80.4
APD_{90}	37.32	88.73	137.8

Simulations also show that the magnitude of $[Ca^{2+}]_i$ transient is greater in control myocytes as compared to failing cells (Fig. 3.7B), which is also observed experimentally (Tamayo et al., 2020; Bartoli et al., 2020; Li et al., 2013). The simulated ratio of the peak $[Ca^{2+}]_i$ for the failing and control myocytes is equal to 0.68, which compares well to the experimentally obtained average data of 0.73±0.07 (Tamayo et al., 2020; Li et al., 2013; Ljubojevic-Holzer et al., 2020; Cai et al., 2019; Chen et al., 2020; Nie et al., 2019).

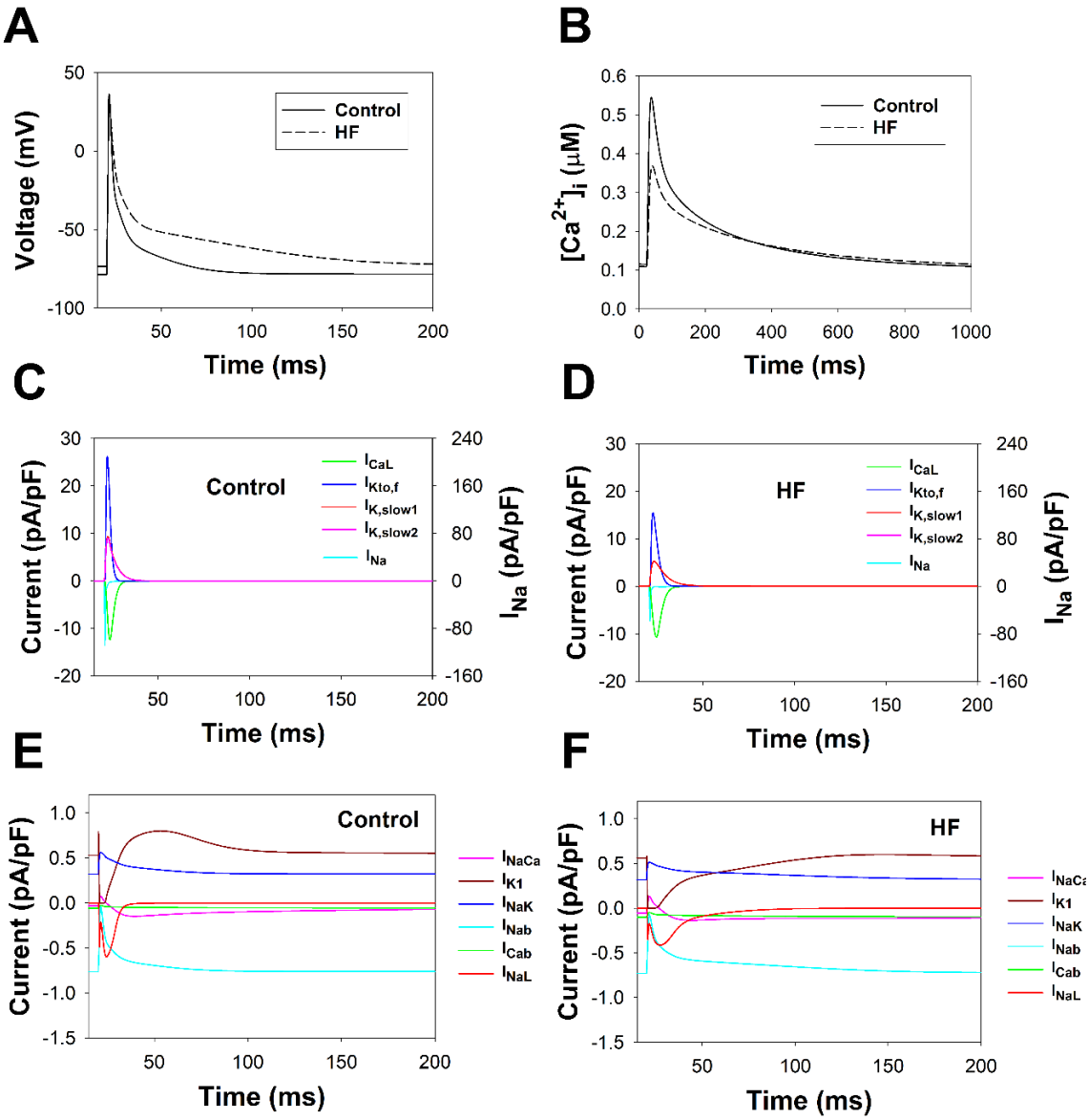

Figure 3.7 *Mouse action potentials, $[Ca^{2+}]_i$ transients, and underlying major ionic currents for control and failing mouse ventricular myocytes.*
(A) *Simulated mouse action potentials for control (solid line) and failing (dashed line) ventricular myocytes.* ***(B)*** *Simulated $[Ca^{2+}]_i$ transients for control (solid line) and failing (dashed line) ventricular myocytes.* ***(C, E)*** *Simulated major ionic currents underlying control mouse action potential.* ***(D, F)*** *Simulated major ionic currents underlying failing mouse action potential. In all panels, action potentials, $[Ca^{2+}]_i$ transients, and ionic currents are shown after 300 s stimulation with 1 Hz.*

The application of 1 μM isoproterenol (a 5-minute exposure) resulted in the prolongation of both control and failing APs in simulations (Figs. 3.7A and 3.8A). The failing myocytes APD_{25}

prolonged from 2.44 to 2.94 ms (20.8% lengthening), APD_{50} - from 5.65 to 8.50 ms (50.4%), and APD_{90} - from 86.82 to 88.73 ms (2.2%) (Table 3.3). After the application of 1 μM isoproterenol, significantly smaller APD prolongations were observed in control ventricular myocytes at earlier stages of repolarization (Table 3.3). However, the later stages of repolarization were more significantly affected by isoproterenol in control myocytes than in the failing. In control myocytes, APD_{25} prolonged from 1.71 to 1.93 ms (by 12.9%), APD_{50} - from 3.25 to 4.40 ms (by 35.4%), and APD_{90} - from 28.86 to 37.32 ms (by 29.3%). APDs of failing myocytes, at all levels of repolarization, are more prolonged than in control after exposure to 1 μM isoproterenol. The role of underlying ionic currents in the repolarization of the control and failing myocytes is similar to that without the application of isoproterenol (Fig. 3.8C-3.8F).

Simulations demonstrate an increase in the magnitude of $[Ca^{2+}]_i$ transient both in control and failing myocytes after the application of 1 μM isoproterenol (Fig. 3.7B and 3.8B), which is also observed experimentally (Ginsburg & Bers 2004; Bing et al., 1991). In control cells, $[Ca^{2+}]_i$ transient increased by 3.27 fold, while in failing cells, the increase was only by 1.93 fold. A smaller increase of $[Ca^{2+}]_i$ in the failing cells demonstrates a reduced response to β-adrenergic stimulation than the control myocytes.

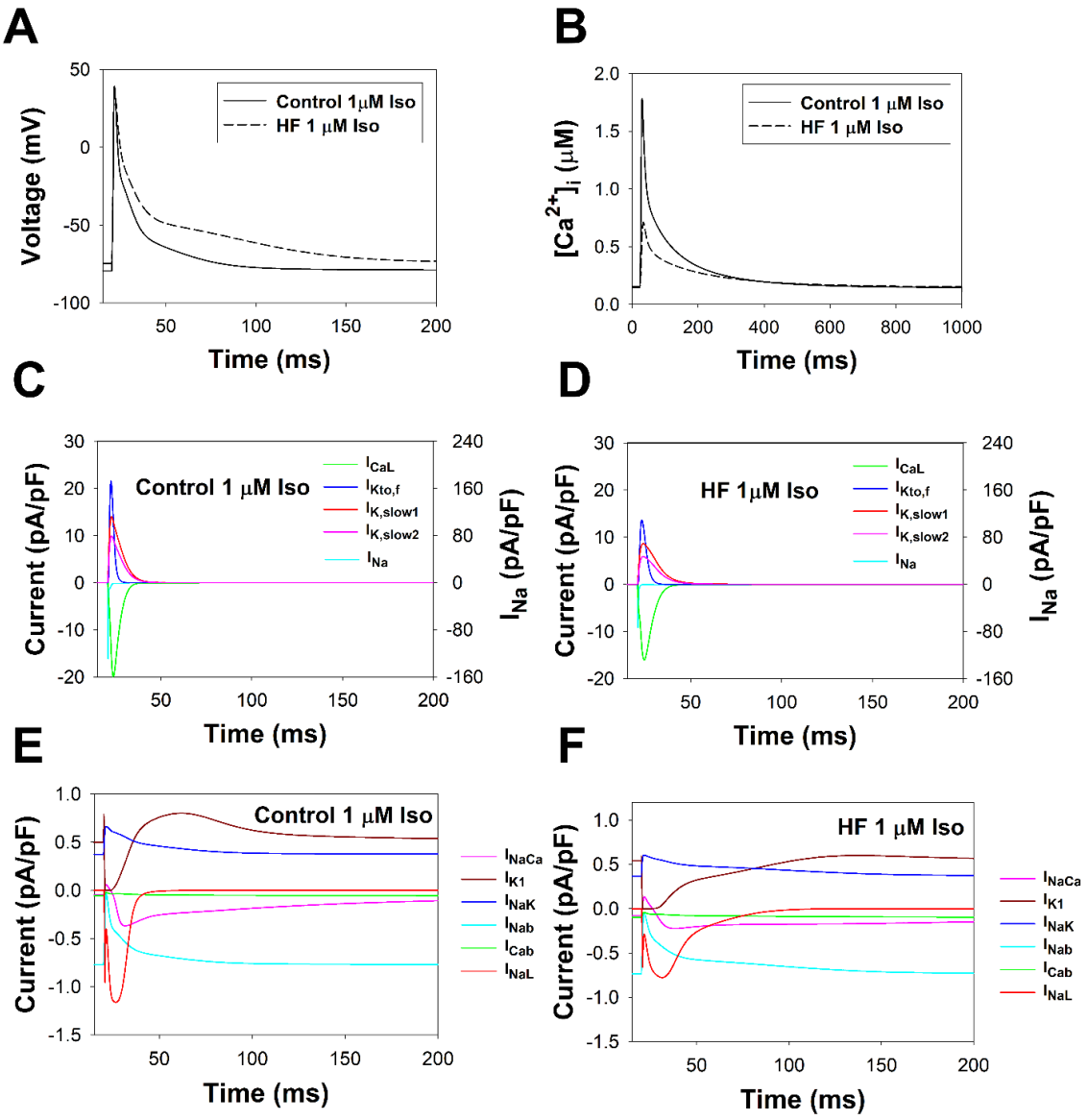

Figure 3.8 *Mouse action potentials, $[Ca^{2+}]_i$ transients, and underlying major ionic currents for control and failing mouse ventricular myocytes after application of 1 μM isoproterenol.* ***(A)*** *Simulated mouse action potentials for control (solid line) and failing (dashed line) ventricular myocytes.* ***(B)*** *Simulated $[Ca^{2+}]_i$ transients for control (solid line) and failing (dashed line) ventricular myocytes.* ***(C, E)*** *Simulated major ionic currents underlying control mouse action potential.* ***(D, F)*** *Simulated major ionic currents underlying failing mouse action potential. In all panels, action potentials, $[Ca^{2+}]_i$ transients, and ionic currents are shown after 300 s stimulation with 1 Hz. 1 μM isoproterenol is applied at time t = 0 s.*

3.2.4 Integrated Ca^{2+} and Na^{+} Fluxes in Mouse Failing and Control Myocytes

Simulated integral Ca^{2+} fluxes in mouse control and failing ventricular myocytes without and with the application of 1 μM isoproterenol are shown in Fig. 3.9 and Table 3.4. Without isoproterenol, simulations show larger integral Ca^{2+} release flux in control (35.63 μM) versus failing (24.30 μM) myocytes (Figs. 3.9A and 3.9B). However, the triggering Ca^{2+} influx by the $I_{Ca,L}$ is only 12% larger in control (1.60 μM) as compared to failing (1.41 μM) cells. We suggest that the larger Ca^{2+} release flux in mouse control cells is mainly due to the larger SR Ca^{2+} load compared to the failing myocytes (894 μM and 599 μM for control and failing myocytes, respectively). Simulated Ca^{2+} extrusion by Na^{+}/Ca^{2+} exchanger is higher in failing mouse ventricular myocytes (3.54 μM) than in control myocytes (3.15 μM). However, this difference is quite small, considering that the expression of the Na^{+}/Ca^{2+} exchanger has increased by 1.8-fold (in the model, parameter k_{NaCa} was increased from 275 pA/pF to 495 pA/pF). Application of 1 μM isoproterenol increases Ca^{2+} entry through the L-type Ca^{2+} channels both in mouse control (3.47 μM) and failing (2.87 μM) myocytes, as well as integral Ca^{2+} release fluxes in control (50.82 μM) and failing (30.03 μM) myocytes (Figs. 3.9C and 3.9D). It is apparent that the failing myocytes demonstrate a weaker response to β-adrenergic stimulation in terms of the released Ca^{2+} from the SR. The amount of Ca^{2+} released from the SR was increased by 1.43-fold and 1.24-fold for control and failing cells, respectively. Nevertheless, we need to note that the difference is not dramatically large, suggesting that our mathematical model simulated a relatively early stage of heart failure after 6-8 weeks of TAC.

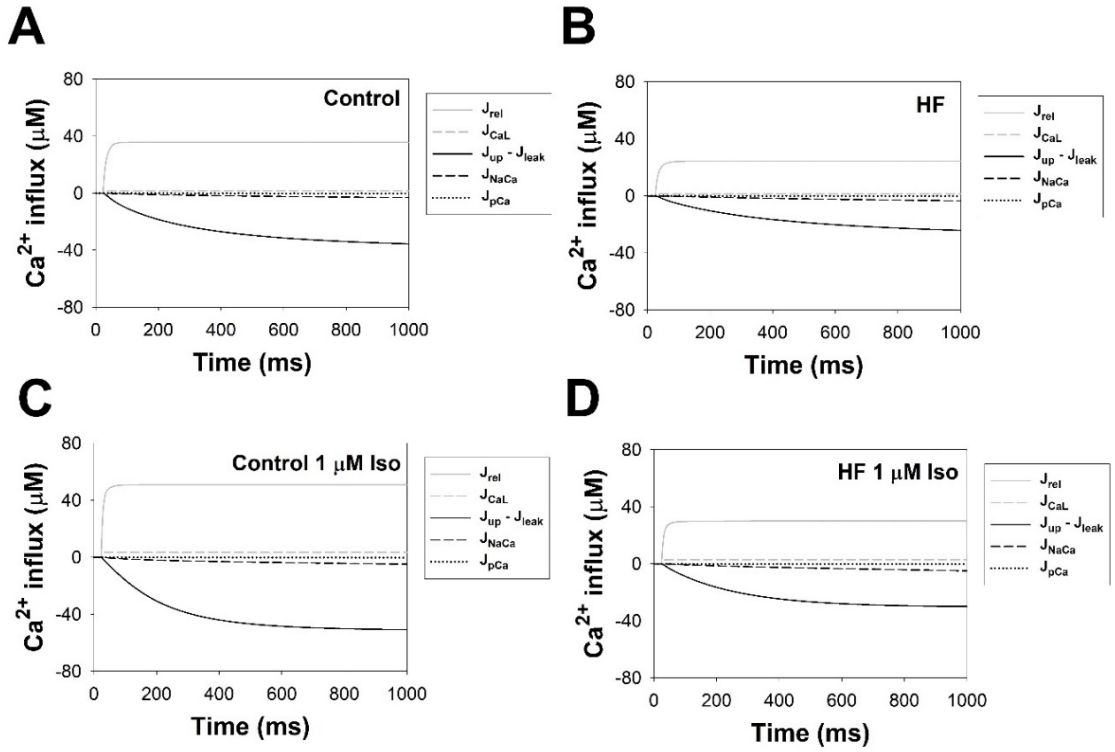

Figure 3.9 *Simulations of the integrated Ca^{2+} fluxes (influxes) in isolated control and failing mouse ventricular myocytes during one cardiac cycle.*
(A, C) *Simulated Ca^{2+} influxes for control myocytes.* ***(B, D)*** *Simulated Ca^{2+} influxes for the failing myocytes. Simulations without and with 1 μM isoproterenol are shown in (A, B) and (C, D), respectively. Here, J_{rel} is the Ca^{2+} release from the SR; J_{CaL} is the Ca^{2+} entering the cell through the L-type Ca^{2+} channels; $J_{up} – J_{leak}$ is the uptake of Ca^{2+} from the cytosol to the network SR with subtracted Ca^{2+} leak from the SR to the cytosol; J_{NaCa} is the Ca^{2+} outflux from the cytosol through the Na^{+}/Ca^{2+} exchanger, and J_{pCa} is the Ca^{2+} outflux through the sarcolemmal Ca^{2+} pump. Ca^{2+} fluxes are shown after 300 s of stimulation with 1 Hz. 1 μM isoproterenol is applied at time t = 0 s.*

Table 3.4 *Integrated Ca^{2+} fluxes in mouse control and failing ventricular myocytes*

Flux (μM)	Control	HF
No Iso		
J_{rel}	35.63	24.30
J_{CaL}	1.60	1.41
J_{up} - J_{Leak}	35.63	24.30
J_{NaCa}	3.15	3.54
J_{pCa}	0.177	0.1204
1 μM Iso		
J_{rel}	50.82	30.03
J_{CaL}	3.47	2.87
J_{up} - J_{Leak}	50.8185	30.0271
J_{NaCa}	4.8594	4.9174
J_{pCa}	0.301	0.189

We also simulated integrated Na^+ fluxes in mouse control and failing ventricular myocytes (Fig. 3.10). Simulations showed that the integrated Na^+ influx through the fast Na^+ channels is much larger in control myocytes (3.89 μM) versus failing myocytes (2.05 μM) due to a smaller I_{Na} in the failing cells. This difference is compensated in parts by the larger integrated Na^+ influx by the Na^+/Ca^{2+} exchanger (10.62 μM vs. 9.45 μM in failing vs. control cells, respectively) and the late Na^+ current (0.42 μM vs. 0.29 μM in failing vs. control cells, respectively) in the failing myocytes. However, the major competitive fluxes in both control and failing cells are the Na^+ influx by the Na^+ background current and the Na^+ outflux by the Na^+-K^+ pump. Simulated Na^+ entries by the background Na^+ currents are 46.54 μM and 32.90 μM for control and failing myocytes, respectively; Na^+ outfluxes by the Na^+-K^+ pump are 60.00 μM and 45.63 μM for control and failing myocytes, respectively.

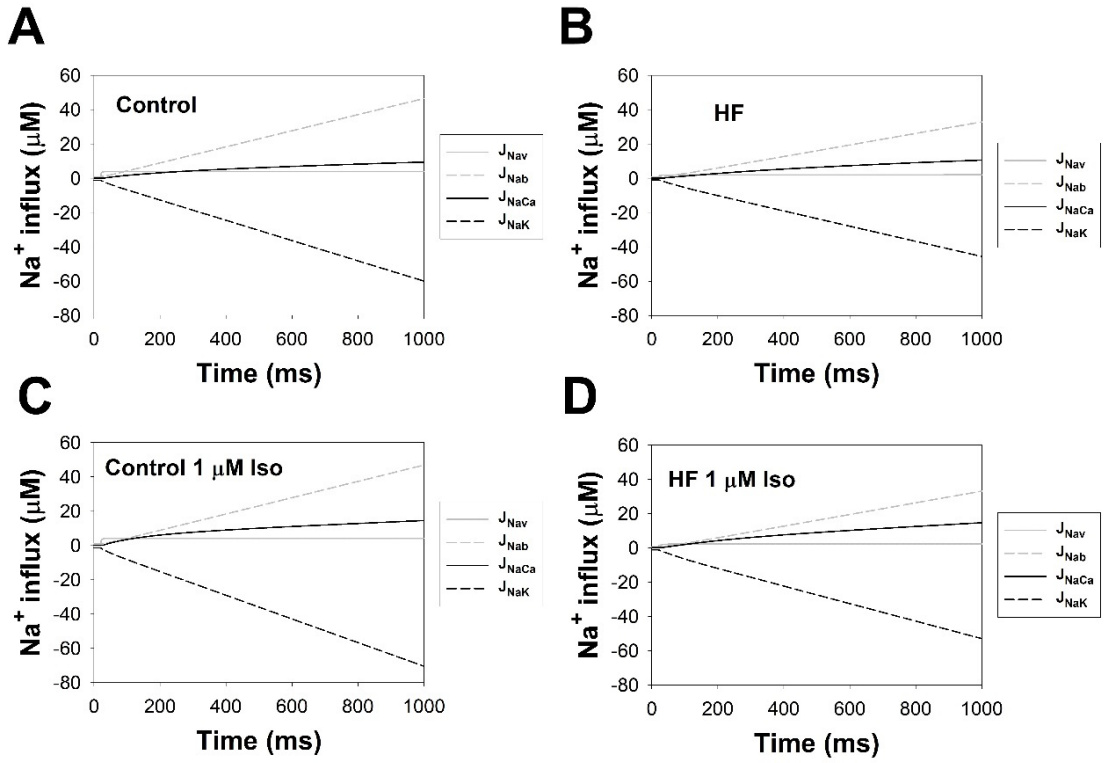

Figure 3.10 *Simulations of the integrated Na^+ fluxes (influxes) in isolated control and failing mouse ventricular myocytes during one cardiac cycle.*
(A, C) *Simulated Na^+ influxes for control myocytes.* ***(B, D)*** *Simulated Na^+ influxes for the failing myocytes. Simulations without and with 1 μM isoproterenol are shown in (A, B) and (C, D), respectively. Here, J_{Nav} is the Na^+ influx through the channels responsible for the fast Na^+ current; J_{Nab} is the background Na^+ influx; J_{NaCa} is the Na^+ influx through the Na^+/Ca^{2+} exchanger; J_{NaK} is the Na^+ outflux through the Na^+-K^+ pump. Na^+ fluxes are shown after 300 s of stimulation with 1 Hz. 1 μM isoproterenol is applied at time t = 0 s.*

Stimulation of β-adrenergic receptors increased the integrated Na^+ influx through the fast Na^+ channels to 4.21 μM in control versus 2.39 μM in failing myocytes; by the Na^+/Ca^{2+} exchanger to 14.58 μM in control versus 14.75 μM in failing myocytes; by the late Na^+ current to 0.84 μM in control versus to 0.99 μM in failing myocytes. In addition, the Na^+ entry by the background Na^+ currents for control and failing myocytes did not change significantly and are equal to 46.92 μM and 33.17 μM, respectively. However, Na^+ outfluxes by the Na^+-K^+ pump increased appreciably to 70.39 μM and 52.85 μM for control and failing myocytes, respectively, due to a larger Na^+-K^+ pump activity upon β-adrenergic stimulation (Bondarenko, 2014).

Table 3.5 *Integrated Na^+ fluxes in mouse control and failing ventricular myocytes*

Na^+ Flux (μM)	Control	HF
No Iso		
J_{Nav}	3.89	2.05
J_{Nab}	46.54	32.90
J_{NaCa}	9.45	10.62
J_{NaK}	60.00	45.63
J_{NaL}	0.29	0.42
1 μM Iso		
J_{Nav}	4.21	2.39
J_{Nab}	46.92	33.17
J_{NaCa}	14.58	14.75
J_{NaK}	70.39	52.85
J_{NaL}	0.84	0.99

3.2.5 Frequency Dependences of $[Ca^{2+}]_i$ Transients in Failing and Control Myocytes

We also investigated frequency dependences of the $[Ca^{2+}]_i$ transients without and with the application of 1 μM isoproterenol. Our simulations show an increase in diastolic $[Ca^{2+}]_i$ concentrations with stimulation frequency in both control and failing myocytes (Fig. 3.11A and 3.11 B). Without isoproterenol, both control and failing myocytes demonstrate biphasic frequency dependence of the peak $[Ca^{2+}]_i$, which has been observed experimentally (see, for example (Ito et al., 2000). However, the peak $[Ca^{2+}]_i$ concentrations are greater in control as compared to failing myocytes. Comparison of the decrease in normalized $[Ca^{2+}]_i$ transients in failing versus control myocytes between experimental and simulations shows good agreement (Fig. 3.11C). After the application of 1 μM isoproterenol, the dependence becomes different. It includes an increasing part at the lower stimulation frequencies and a weakly decreasing part at the higher frequencies.

We also obtained a much larger increase in the peak $[Ca^{2+}]_i$ concentrations in control myocytes, which indicated a blunted response to β-adrenergic stimulation in the failing cells.

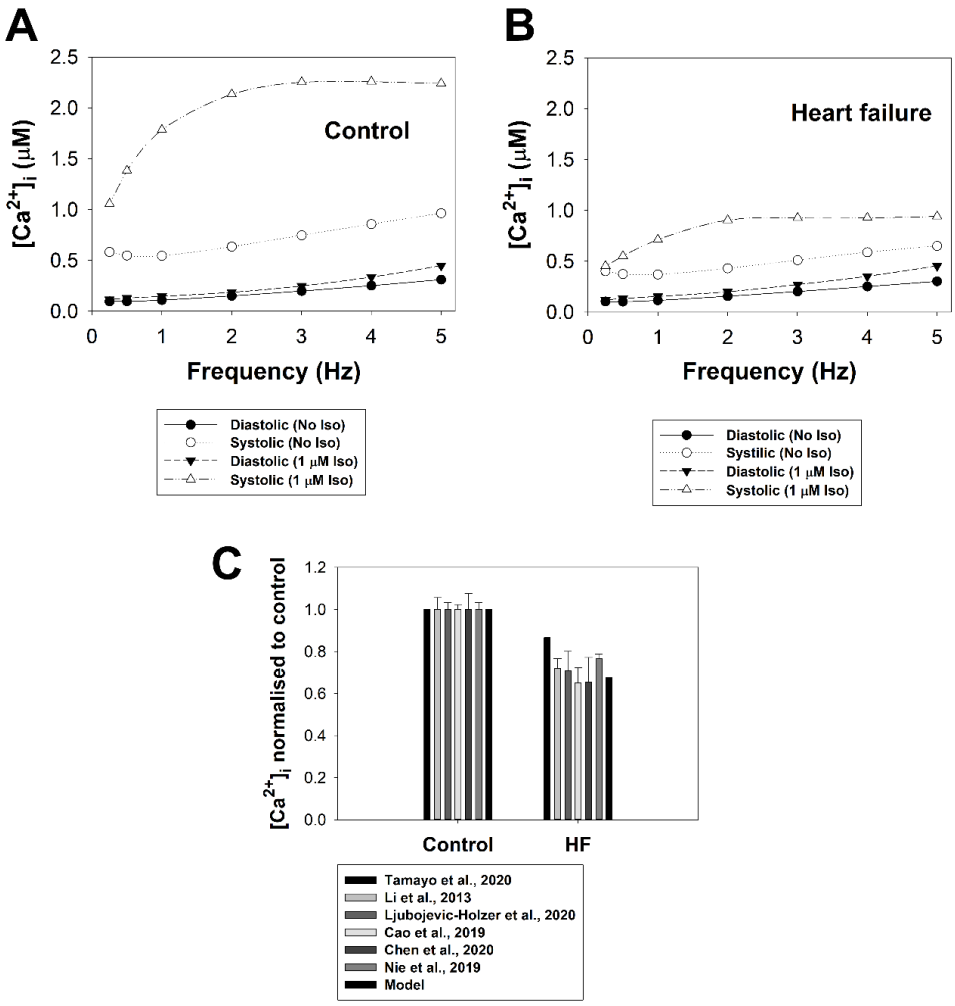

Figure 3.11 Simulations of the frequency dependence of $[Ca^{2+}]_i$ transients in control and failing mouse ventricular myocytes.
(A) *Simulated diastolic (filled symbols) and systolic (unfilled symbols) $[Ca^{2+}]_i$ magnitudes without isoproterenol (circles) and after 1 μM isoproterenol application (triangles) as functions of stimulation frequency for control myocytes.* ***(B)*** *Simulated diastolic (filled symbols) and systolic (unfilled symbols) $[Ca^{2+}]_i$ magnitudes without isoproterenol (circles) and after 1 μM isoproterenol application (triangles) as functions of stimulation frequency for failing myocytes.* ***(C)*** *Comparison of the experimental and simulated $[Ca^{2+}]_i$ transients for control and failing ventricular myocytes. Experimental data are from Li et al.(2013); Nie et al. (2019), Cai et al. (2019), Tamayo et al. (2020), Ljubojevic-Holzer et al. (2020), and Chen et al. (2020). Simulated data are shown after 300 s of stimulation with 1 Hz.*

3.2.6 Sensitivity Analysis

In order to define the major contributing ionic currents to the changes in AP and $[Ca^{2+}]_i$ transients in control and failing mouse ventricular myocytes, we performed a sensitivity analysis (Fig. 3.12). For this purpose, we first stimulated the ventricular model cell for 300 s with a basic cycle length 1000 ms (I_{stim} = 80 pA/pF, τ_{stim} = 1 ms) and then abruptly increased one of the current conductance by 5% at the beginning of the 301st beat. Then the effect of this abrupt change was estimated on APD_{25}, APD_{50}, APD_{90}, AP amplitude, and $[Ca^{2+}]_i$ transient in both control and failing ventricular myocytes.

In control, the major player for APD_{25} and APD_{50} is the rapidly recovering transient outward K^+ current, $I_{Kto,f}$ (Fig. 3.12, A and B). Three other currents, the L-type Ca^{2+} current, I_{CaL}, and two rapidly activating, slowly inactivating K^+ currents, $I_{K,slow1}$ and $I_{K,slow2}$, also made significant contributions to the change in APD_{25} and APD_{50}. The K^+ currents tend to shorten, while I_{CaL} tends to prolong APD_{25} and APD_{50}. The regulation of APD_{90} is more complex. Eight major ionic currents affect APD_{90} (Fig. 3.12C). The L-type Ca^{2+} current, I_{CaL}, the Na^+/Ca^{2+} exchanger current I_{NaCa}, and the background Na^+ current, I_{Nab}, tend to prolong APD_{90}. In contrast, the Na^+-K^+ pump current, I_{NaK}, the time-independent K^+ current, I_{K1}, two rapidly activating, slowly inactivating K^+ currents, $I_{K,slow1}$ and $I_{K,slow2}$, and the noninactivating steady-state voltage-activated K^+ current, I_{Kss}, tend to shorten APD_{90}. In control, AP amplitude is affected by four major currents (Fig. 3.12D). Three currents, I_{Na}, I_{NaK}, and I_{K1}, increase, while I_{Nab} decreases AP amplitude. The major contributing factor to $[Ca^{2+}]_i$ transient is the L-type Ca^{2+} current (Fig. 3.12E), which increases $[Ca^{2+}]_i$. Two rapidly activating, slowly inactivating K^+ currents, $I_{K,slow1}$ and $I_{K,slow2}$, and the rapidly recovering transient outward K^+ current, $I_{Kto,f}$ also made some contribution, probably, through the shortening APDs.

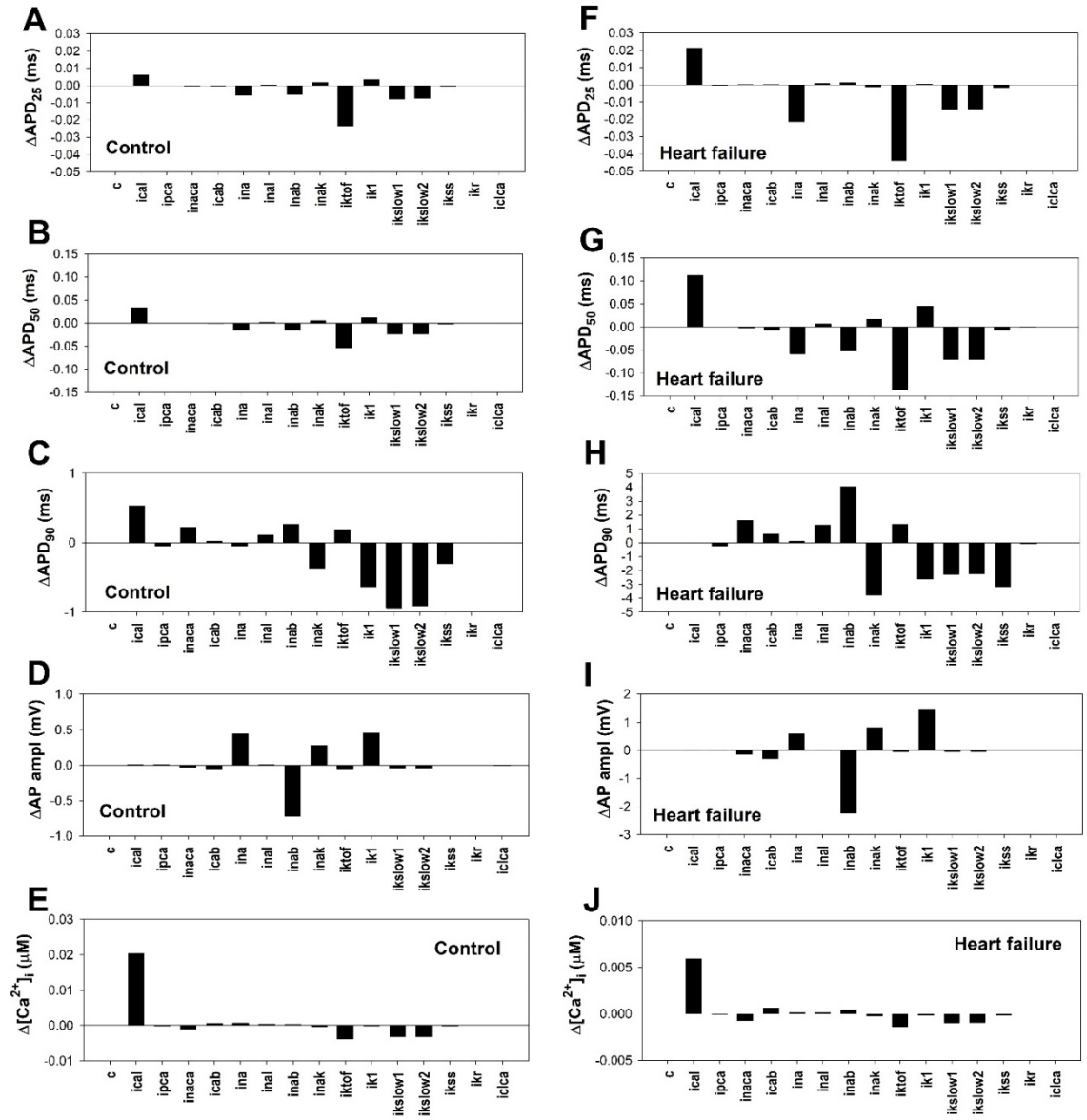

Figure 3.12 *Sensitivity analysis.*
*Changes of action potential (AP) duration at 25% (**Panels A and F**), 50% (**Panels B and G**), and 90% repolarization (**Panels C and H**), AP amplitude (**Panels D and I**), and $[Ca^{2+}]_i$ transient (**Panels E and J**) between the two consecutive stimuli (the 301st and 300th pacing beats) at 1 Hz. We increased the magnitude of one of several ionic currents by 5% during the 301st pacing beat. The changes were calculated as the differences between AP durations, AP amplitudes, and $[Ca^{2+}]_i$ transients during the 301st and 300th beats. Simulations were performed for control (Control, **Panels A-E**) and failing (Heart failure, **Panels F-J**) myocytes. Sensitivity analysis is performed with respect to 5% increase of the L-type Ca^{2+} current (I_{CaL}), the sarcolemmal Ca^{2+} pump current (I_{pCa}), the Na^+/Ca^{2+} exchanger current (I_{NaCa}), the Ca^{2+} background current (I_{Cab}), the fast Na^+*

current (ina), the late Na^+ current (I_{NaL}), the Na^+ background current (I_{Nab}), the Na^+-K^+ pump current (I_{NaK}), the rapidly recovering transient outward K^+ current (I_{Ktof}), the time-independent K^+ current (I_{K1}), the rapidly activating, slowly inactivating K^+ current (encoded by $K_v1.5$; 4-aminopyridine-sensitive; ikslow1), the rapidly activating, slowly inactivating K^+ current (encoded by $K_v2.1$; TEA-sensitive; I_{Kslow2}), the noninactivating steady-state voltage-activated K^+ current (I_{Kss}), the rapid delayed rectifier K^+ current (I_{Kr}), and the Ca^{2+}-activated chloride current (I_{ClCa}). No changes are shown for the simulations without 5% perturbation of the model parameters (c).

In the failing ventricular myocytes, APD_{25} and APD_{50} were affected by the six major currents, I_{CaL}, I_{Na}, I_{Nab}, $I_{Kto,f}$, $I_{K,slow1}$, and $I_{K,slow2}$, but in different proportions. For APD_{25}, the effect of $I_{Kto,f}$ and the contributions of I_{CaL}, I_{Na}, $I_{K,slow1}$, and $I_{K,slow2}$ have increased compared to control cells (Fig. 3.12F). For APD_{50}, the role of $I_{Kto,f}$ was also increased along with I_{CaL}, I_{Na}, $I_{K,slow1}$, and $I_{K,slow2}$, which increased their effects (Fig. 3.12G). Nine currents affect APD_{90} of failing myocytes (Fig. 3.12H). The major role was played by the background Na^+ current I_{Nab}, which prolonged APD_{90}, and the Na^+-K^+ pump current I_{NaK}, which shortened APD_{90}. Seven other currents, I_{NaCa}, I_{NaL}, $I_{Kto,f}$, I_{K1}, $I_{K,slow1}$, $I_{K,slow2}$, and I_{Kss}, have a smaller but still significant contribution to APD_{90}. The major players and their proportional contributions that affect AP amplitude and $[Ca^{2+}]_i$ transient in the failing myocytes are the same as in control (Fig. 3.12, I and J). However, the AP amplitude of the failing myocytes is much more sensitive to these currents than the control (Fig. 3.12, D and I). In contrast, $[Ca^{2+}]_i$ transient is less sensitive to the changes in the major contributing currents as compared to control (Fig. 3.12, E and J).

3.2.7 Sarcoplasmic Reticulum Ca^{2+} Load Regulation in Control and Failing Ventricular Myocytes

It is believed that the major factor that regulates myocyte contraction and $[Ca^{2+}]_i$ transient is the SR Ca^{2+} load (Eisner et al., 2017; Eisner et al., 2020). In control myocytes, the SR load is defined by a delicate balance between the SERCA pump function, the ryanodine receptors release and leak, the Na^+/Ca^{2+} exchanger function, the Ca^{2+} influx through the L-type Ca^{2+} channels, the

Ca^{2+} buffering, the sarcolemmal Ca^{2+} pump, and the background Ca^{2+} influx mechanism. In failing hearts, dysregulation of one or several of these factors results in a smaller SR Ca^{2+} load and $[Ca^{2+}]_i$ transient, as observed experimentally (Bartoli et al., 2020; Chen et al., 2020; Li et al., 2013; Bryant et al., 2018). However, the mechanism of the dysfunction is quite complicated and is different for different heart failure phenotypes (Eisner et al., 2020).

To demonstrate the role of different Ca^{2+} handling proteins in the SR Ca^{2+} load in failing mouse ventricular myocytes, we used the base failing myocyte model described above and changed some Ca^{2+} handling protein functions to their control model values. We did not change the magnitudes of the L-type Ca^{2+} current, Ca^{2+} buffering, and the sarcolemmal Ca^{2+} pump, as they did not change too much in heart failure or did not make a significant contribution; therefore, they were excluded from this investigation.

Figure 3.13 shows the action potentials, the $[Ca^{2+}]_i$ transients, and the junctional SR Ca^{2+} concentrations $[Ca^{2+}]_{JSR}$ as functions of time for the base failing myocyte model (red lines) and for the failing myocyte models where one of the Ca^{2+} handling protein's model parameters (the SERCA pump, the Na^+/Ca^{2+} exchanger, the background Ca^{2+} current, Ca^{2+} leak from the SR, and Ca^{2+} release from the SR) was replaced by the corresponding equivalent control model value. Simulation results show that among those Ca^{2+} handling proteins, the major effect on the action potential in failing myocytes is caused by the background Ca^{2+} current I_{Cab} that has increased and prolonged the action potential in the failing heart (Fig. 3.13A). Other Ca^{2+} handling proteins do not significantly affect the AP.

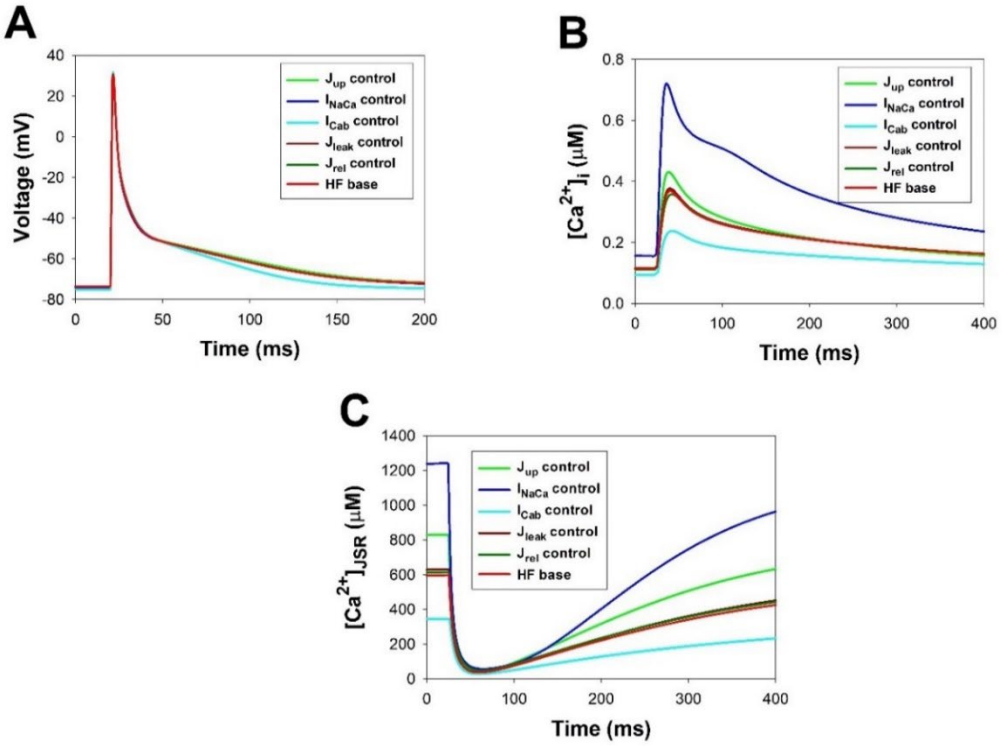

Figure 3.13 *The role of Ca^{2+} handling proteins in the SR Ca^{2+} load in failing ventricular myocytes. Action potentials **(A)**, $[Ca^{2+}]_i$ transients **(B)**, and the SR Ca^{2+} load **(C)** as functions of time for the base failing myocyte model (HF base, red lines), as well as for the models in which the base model parameters were replaced by the control model parameters for the SERCA pump (J_{up} control, green lines), the Na^+/Ca^{2+} exchanger (I_{NaCa} control, blue lines), the background Ca^{2+} current (I_{Cab} control, cyan lines), Ca^{2+} leak from the SR (J_{leak} control, dark red lines), and Ca^{2+} release from the SR (J_{rel} control, dark green lines). Simulated data are shown after 300 s of stimulation with 1 Hz.*

The result is quite different for $[Ca^{2+}]_i$ transients and the JSR Ca^{2+} concentration (Fig. 3.13B and C). The most dramatic changes in $[Ca^{2+}]_i$ and $[Ca^{2+}]_{JSR}$ concentrations are caused by the Na^+/Ca^{2+} exchanger and the background Ca^{2+} current when inverted to their control values. The heart failure myocyte model with control I_{NaCa} demonstrates a dramatically increased $[Ca^{2+}]_i$ transient and the JSR Ca^{2+} concentration. This means that the adaptive increase in I_{NaCa} in the failing myocyte prevents the cell from Ca^{2+} overload, reduces $[Ca^{2+}]_i$ transient, and, as a consequence, reduces energy consumption during contraction. On the other hand, a reversion of the background Ca^{2+} current I_{Cab} to its control value resulted in a dramatic decrease of $[Ca^{2+}]_i$

transient and JSR Ca^{2+} concentration, leading to impaired cell (heart) contraction. Therefore, the failing myocytes require more Ca^{2+} entry to maintain proper cardiac output. A less dramatic but quite significant role is seen for the SERCA pump. The reversion of J_{up} to its control value increases $[Ca^{2+}]_i$ transient by 17% and $[Ca^{2+}]_{JSR}$ by 39%; therefore, adaptation of the SERCA pump function serves to prevent Ca^{2+} overload in the failing myocytes. As seen from the simulations, the sole action of two other Ca^{2+} handling mechanisms, Ca^{2+} leak, and Ca^{2+} release, does not significantly affect $[Ca^{2+}]_i$ transient and $[Ca^{2+}]_{JSR}$.

3.2.8 Mechanism of Proarrhythmic $[Ca^{2+}]_i$ Transient in Failing Ventricular Myocytes upon Activation of β-adrenergic Signaling

Experimental data showed that the application of isoproterenol to failing mouse hearts made them more susceptible to pro-arrhythmic events and ventricular tachycardia (Cerrone et al., 2007; van Oort, McCauley, et al., 2010; Liu et al., 2011). It was also shown that the proarrhythmic events were related to the dysfunction of genetically modified ryanodine receptors (van Oort, McCauley, et al., 2010; Liu et al., 2011).

To investigate whether a similar mechanism is possible in the failing mouse ventricular myocytes after TAC, we studied the myocyte behavior at a relatively fast 5-Hz pacing without and with the application of 1 μM isoproterenol (Fig. 3.14). In addition, we also studied the effects of I_{NaL} and β_1-AR blocks on the myocyte's activity. Without isoproterenol in control, $[Ca^{2+}]_i$ transients show clear rising (due to Ca^{2+} release from the SR and Ca^{2+} movement from the dyadic space to the cytosol) and decaying (predominantly due to the SERCA pump and I_{NaCa} function) phases (Fig. 3.14C). A block of β_1-ARs reduces $[Ca^{2+}]_i$ transient predominantly due to a reduction of the L-type Ca^{2+} current and the corresponding Ca^{2+} entry into the cell; however, block of I_{NaL} does not affect $[Ca^{2+}]_i$ transient. Both the block of β_1-ARs and I_{NaL} does not affect action potential

shape (Fig. 3.14A). Upon application of 1 μM isoproterenol in control, $[Ca^{2+}]_i$ transient demonstrates a perturbation of the decaying phase, which leads to a prolongation of $[Ca^{2+}]_i$ (Fig. 3.14F). Block of I_{NaL} does not affect perturbed $[Ca^{2+}]_i$ transient; however, block of β_1-ARs improves $[Ca^{2+}]_i$ transient shape (Fig. 3.14F). In addition, the block of β_1-ARs shows a stronger effect on the action potential than the block of I_{NaL} (Fig. 3.14E). Thus, our simulations demonstrate that the block of β_1-ARs prevents pro-arrhythmic $[Ca^{2+}]_i$ transient, while the block of I_{NaL} does not show significant effects.

To reveal the mechanism of pro-arrhythmic $[Ca^{2+}]_i$ transient upon application of isoproterenol in the failing mouse ventricular myocytes, we investigated the behavior of Ca^{2+} concentration in the dyadic space $[Ca^{2+}]_{ss}$ and the opening probability of ryanodine receptors (Fig. 3.14). Without isoproterenol in control, $[Ca^{2+}]_{ss}$ demonstrates a relatively sharp raising phase, which is defined by the rate of the RyR opening, and a somewhat slower decaying phase, which is determined by the diffusion of Ca^{2+} from the dyadic space to bulk cytosol (Fig. 3.14C). The block of I_{NaL} does not affect $[Ca^{2+}]_{ss}$; however, the block of β_1-ARs slightly reduces the peak value of $[Ca^{2+}]_{ss}$. Upon the application of 1 μM isoproterenol in control (I_{NaL} blocked), $[Ca^{2+}]_{ss}$ shows two maxima that prolong the high Ca^{2+} concentration phase in the dyadic space (Fig. 3.14G), with a significantly smaller first maximum as compared to $[Ca^{2+}]_{ss}$ without isoproterenol. The block of I_{NaL} does not affect perturbed $[Ca^{2+}]_{ss}$; however, the block of β_1-ARs restores normal behavior of $[Ca^{2+}]_{ss}$. It seems like the delayed Ca^{2+} release from the SR plays a significant role in the pro-arrhythmic activity.

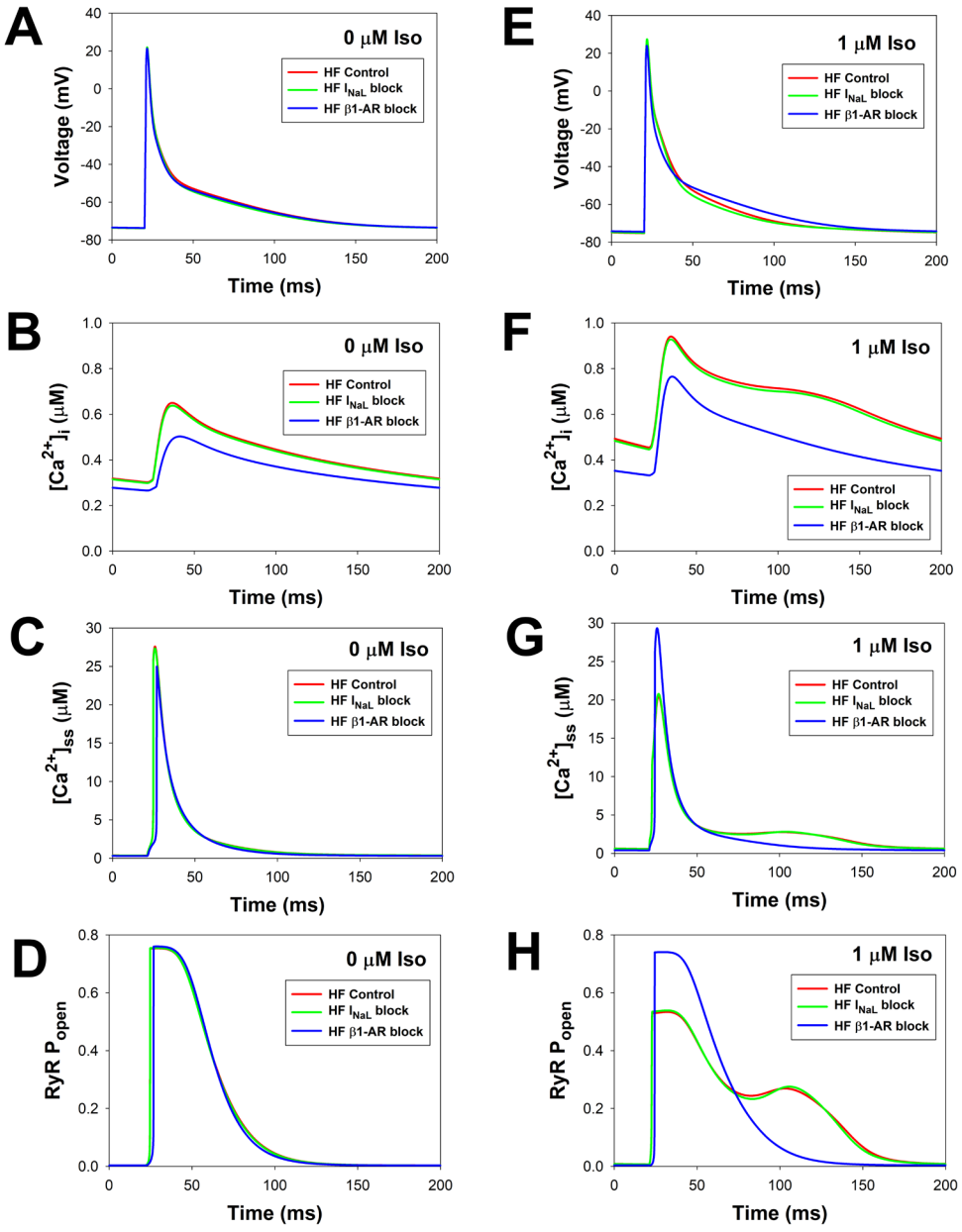

Figure 3.14 *Mechanism of proarrhythmic $[Ca^{2+}]_i$ transient and its suppression in mouse failing ventricular myocytes.*
*Action potential (**A, E**), $[Ca^{2+}]i$ transient (B, F), dyadic space Ca^{2+} concentration $[Ca^{2+}]ss$ (**C, G**), and opening probability of RyRs (**D, H**) as functions of time. Data without and with the application of 1 μM isoproterenol are shown in (**A-D**) and (**E-H**), respectively. Simulation for control failing myocytes are shown by red lines, after I_{NaL} block – by green lines, and after β_1-ARs block – by blue lines. Simulated data are shown after 300 s of electrical stimulation with 5 Hz.*

Indeed, the analysis of the behavior of the RyRs opening probability in these simulations provided a clear explanation of the obtained results. Without isoproterenol in control, ryanodine receptors open very rapidly due to their strong (3rd and 4th power) dependence on $[Ca^{2+}]_{ss}$ (Keizer and Levine, 1996) and then decay slower after a plateau phase (Fig. 14D). Neither block of β_1-ARs nor I_{NaL} affect the time behavior of RyR opening. After the application of 1 μM isoproterenol in control, ryanodine receptors do not reach the same opening probability as that without isoproterenol due to different gating properties of phosphorylated and non-phosphorylated fractions of RyRs (Fig. 3.14H), which results in a slower receptor closing and subsequent reactivation of the open state. This ultimately prolongs Ca^{2+} release and distorts $[Ca^{2+}]_i$ transient. A block of β_1-ARs, which dramatically reduces the phosphorylated fraction of RyRs, restores their normal gating and normal Ca^{2+} release.

3.3 Discussion

3.3.1 Compartmentalization, β-adrenergic Regulation, and Action Potential in Normal and Failing Ventricular Myocytes

Experimental data showed that the development of heart failure resulted in a reduction of the concentration of β_1-adrenergic receptors in multiple species; however, the concentration of β_2-adrenergic receptors was preserved (Baker, 2014). Experimental data also showed that the overexpression of β_1-adrenergic receptors led to accelerated heart failure development (Engelhardt et al., 1999), while a moderate overexpression of β_2-adrenergic receptors improved cardiac function (Milano et al., 1994). Therefore, it is considered that a reduction of β_1-AR concentration is an adaptive mode in the failing hearts to slow down further development of heart failure. In addition, a decrease in adenylyl cyclase activity was also observed in the failing hearts (Tachibana, 2005; Nienaber, 2003; Esposito, 2002). Finally, the failing ventricular myocytes demonstrated re-distribution of β_2-ARs from the t-tubules to the rest of the cell (Nikolaev et al., 2010).

Reviewing the available experimental data, we concluded that in failing mouse ventricular myocytes obtained after TAC procedure, the reduction of β_1-AR concentration is also ~50%. We also reduced adenylyl cyclase activity to fit the experimental data and moved 50% of β_2-ARs from the caveolar to the extracaveolar compartment. The resulting model reproduced adenylyl cyclase activity observed in the mouse failing ventricular myocytes after TAC procedure (Tachibana, 2005; Nienaber, 2003; Esposito, 2002). In addition, our compartmentalized model allowed us to simulate the time behavior of cAMP and PKA with and without the simultaneous stimulation of both β_1-and β_2-ARs. Simulations using the failing ventricular myocyte model were compared to those for the control model. Simulations reproduced the experimentally observed reduction of adenylyl cyclase activity increase in failing cells upon stimulation with isoproterenol compared to

control (Fig. 3.4). We also found that redistribution of β_2-ARs resulted in increased cAMP production and PKA activity in the extracaveolar compartment, leading to more phosphorylation of the ion channels, including the L-type Ca^{2+} channel, that its conductance was moderately increased. This outcome supports the notion that redistribution of β_2-ARs plays a significant role in maintaining β-adrenergic function in failing ventricular myocytes.

Experimental investigations also demonstrated significant differences in the AP between normal and failing ventricular myocytes in different species (Tomaselli & Marban, 1999; Nattel et al., 2007). Specifically, failing ventricular myocytes have, in general, more prolonged AP and reduced K^+ repolarization currents and generate smaller $[Ca^{2+}]_i$ transient and contraction force than the normal cells. In most species, failing ventricular myocytes possess reduced transient outward K^+ currents, $I_{Kto,f}$ and $I_{Kto,s}$, and time-independent inward-rectifier current I_{K1} (Tomaselli & Marban, 1999; Nattel et al., 2007). However, the reduction of the transient outward K^+ currents more significantly affects rodent myocytes where $I_{Kto,f}$ and $I_{Kto,s}$ are among the primary repolarization currents (Tamayo et al., 2020). In addition, the downregulation of $I_{K,slow}$ current make remarkable contributions to AP prolongation in rodents (Tamayo et al., 2020). In the larger species, a downregulation of the slow delayed rectifier K^+ current I_{Ks} is the most prominent and consistent change that causes AP prolongation in heart failure (Nattel et al., 2007). Our simulations confirm the experimental findings on AP prolongation in failing mouse ventricular myocytes as compared to the normal cells. We also found that a reduction of $I_{Kto,f}$, $I_{K,slow1}$, and $I_{K,slow2}$ are the major contributing factors to the AP prolongation that can be potentially pro-arrhythmic.

3.3.2 Ca^{2+} Dynamics and Mechanisms of the SR Ca^{2+} Load in Normal and Failing Ventricular Myocytes

In addition to APs, differences in $[Ca^{2+}]_i$ transients were observed between normal and failing ventricular myocytes (Janse, 2004; Li et al., 2013; Nie et al., 2019). $[Ca^{2+}]_i$ transients were also observed to be smaller in the failing myocytes compared to the normal cells. In addition, $[Ca^{2+}]_i$ transients in failing myocytes demonstrate a weaker response to β-adrenergic stimulation (O'Rourke et al., 1999). These differences result from the complex remodeling effects of several Ca^{2+} handling proteins involved in $[Ca^{2+}]_i$ production and their regulation by the β-adrenergic signaling system. However, the mechanism of the downregulation of the $[Ca^{2+}]_i$ transients in failing hearts is still a subject of debate (Bers et al., 2003).

It is considered that a reduction of $[Ca^{2+}]_i$ transients in the failing myocytes is mainly due to a reduction of the SR Ca^{2+} load (Bers et al., 2003). Multiple factors affect the SR Ca^{2+} load, including the SERCA pump, ryanodine receptors, the Na^+/Ca^{2+} exchanger, the background Ca^{2+} influx mechanisms, and the sarcolemmal Ca^{2+} pump. There is a balance between these mechanisms in healthy myocytes that maintains a relatively constant SR Ca^{2+} load under normal physiological conditions. However, the progress to a maladaptive change in one or several of these Ca^{2+} handling mechanisms leads to a reduction in the SR Ca^{2+} load. It was found experimentally that heart failure manifests in a decrease in the SERCA pump function (Piacentino et al., 2003; O'Rourke et al., 1999; Pieske et al., 1999), an increase in ryanodine receptor leak (Marx et al., 2000), an increase in the Na^+/Ca^{2+} exchanger function (Reinecke et al., 1996; O'Rourke et al., 1999), as well as the background Ca^{2+} influx (Hutchings et al., 2022).

Using our model, we investigated, numerically, the contribution of these major factors to the reduced SR Ca^{2+} load. Our simulations show that one of the major factors is an increased

Na^+/Ca^{2+} exchanger function (Fig. 3.13). If we keep the normal magnitude of Na^+/Ca^{2+} exchanger outflux in the model of failing myocyte, we obtain a dramatic increase in the SR Ca^{2+} load and $[Ca^{2+}]_i$ transient. Therefore, our simulation results support the importance of a dramatic rise in Na^+/Ca^{2+} exchanger function in the failing myocytes to prevent them from Ca^{2+} overload, and such dramatic upregulation of I_{NaCa} is consistently observed experimentally in the failing hearts of mice and other species (Bers, Pogwizd, & Schlotthauer, 2002; O'Rourke et al., 1999; Pott et al., 2012). Further, our simulations of failing myocytes also show a significant reduction in $[Ca^{2+}]_i$ transient when we used the normal magnitude of the background Ca^{2+} current. Therefore, an increase in the background Ca^{2+} influx is an important mechanism to maintain proper $[Ca^{2+}]_i$ transient in the failing myocyte. Our simulations also demonstrated that a reversal of the SERCA pump function to its normal magnitude in the failing myocytes resulted in a relatively modest increase in $[Ca^{2+}]_i$ transient and the SR Ca^{2+} content (Fig. 3.13). While most of the experimental data showed a decrease in function of the SERCA pump in failing hearts, some data showed no change in its function, which points to its somewhat smaller role in the myocyte adaptation in heart failure (Schwinger et al., 1995). Finally, our simulations do not support a significant contribution of the SR Ca^{2+} leak or the rate of Ca^{2+} release from the SR into the failing $[Ca^{2+}]_i$ transient in mice. However, such mechanisms can be important in other species or in combination with other adaptations of Ca^{2+} handling protein functions.

3.3.3 Pro-arrhythmic Activity in Failing Mouse Ventricular Myocytes

Arrhythmogenic changes in the failing hearts are caused by multiple cardiovascular diseases that include myocardial infarction, congenital heart disease, hypertension, dilated cardiomyopathy, hypertrophic cardiomyopathy, and others (Coronel et al., 2013). These cardiovascular diseases are characterized by electrophysiological remodeling, changes in Ca^{2+}

dynamics, remodeling of the extracellular matrix, and alteration of the signaling systems, including β-adrenergic signaling. Therefore, it is required to reveal a specific cause of heart failure to treat it efficiently.

It is considered that the triggered activity in the failing myocytes due to the altered Ca^{2+} dynamics and ionic currents are among the leading causes of ventricular tachycardia at the cellular level in different species (Pogwizd & Bers, 2004; Coronel et al., 2013; Marks, 2013). Specifically, an increased function of I_{NaCa}, increased ryanodine receptor leak, decreased I_{K1} current, and increased I_{NaL} current are shown to trigger pro-arrhythmic events (EADs, DADs). In addition, it is suggested, to some extent, that the preserved function of β-adrenergic signaling can also contribute to an increased arrhythmogenesis in heart failure (Pogwizd & Bers, 2004).

This work is focused on heart failure with reduced ejection fraction in mice after TAC, which represents a relatively early stage of heart failure. As an example of the application of our mathematical model, we investigated the role of the late Na^+ current, ryanodine receptor gating, and β-adrenergic signaling in the proarrhythmic events in the failing myocytes. Our simulations showed that the activation of β-adrenergic signaling by 1 μM isoproterenol prolonged AP duration and increased and prolonged $[Ca^{2+}]_i$ transients (Fig. 3.14). Investigation of dyadic space Ca^{2+} concentration, $[Ca^{2+}]_{ss}$, and ryanodine receptor gating behavior demonstrated the prolongation of Ca^{2+} release from the SR and a more prolonged time for ryanodine receptors to be in open states. Inhibition of I_{NaL} did not reverse this maladaptive change. However, β_1-AR block restored relatively normal $[Ca^{2+}]_i$ transient, Ca^{2+} release, and ryanodine receptor gating (Fig. 3.14). These simulations suggest that in the mouse model of the early stage of heart failure after TAC, one of the major pro-arrhythmic factors is the instability of the closed state and prolongation of the open states of ryanodine receptors, and the major antiarrhythmic factor is the block of β_1-adrenergic

receptors. These simulation results are in line with the experimental data, which suggest that increased phosphorylation and destabilization of the closed state of ryanodine receptors are among the major causes of pro-arrhythmic events in heart failure (Marks, 2013).

4 CONCLUSION

The results of this dissertation allow for the following major conclusions:

1. A new comprehensive model for mouse atrial myocytes that accurately described mouse atrial action potential, Ca^{2+} dynamics, and β_1- and β_2-adrenergic signaling systems was developed and investigated.
2. The model showed that the T-type Ca^{2+} current significantly affects the later stage of the action potential with a little effect on $[Ca^{2+}]_i$ transients.
3. The block of the small-conductance Ca^{2+}-activated K^+ current leads to a prolongation of the action potential at high intracellular Ca^{2+} concentration.
4. A new comprehensive model for the action potential, Ca^{2+} dynamics, and β_1- and β_2-adrenergic signaling systems in failing mouse ventricular myocytes was developed, investigated, and compared to the normal mouse ventricular myocytes.
5. The mathematical model revealed the mechanisms of the SR Ca^{2+} load in failing mouse ventricular myocytes.
6. The mathematical model also disclosed the mechanisms of pro-arrhythmic events in the failing mouse ventricular myocytes and the mechanisms of the pro-arrhythmic event suppression.

The results of the second chapter of the dissertation have been published in (Asfaw et al., 2020). The results of the third chapter of the dissertation are included in the paper that will be submitted to the physiological journal (Asfaw & Bondarenko, pending publication). The related topic of modeling human cardiac sodium channel was a subject of investigation for MS Thesis by Tesfaye Asfaw and has been published in the journal of membrane biology (Asfaw & Bondarenko, 2019).

REFERENCES

Agarwal, S. R., Gratwohl, J., Cozad, M., Yang, P. C., Clancy, C. E., & Harvey, R. D. (2018). Compartmentalized cAMP Signaling Associated With Lipid Raft and Non-raft Membrane Domains in Adult Ventricular Myocytes. *Frontiers in pharmacology*, *9*, 332.

Asfaw, T. N., & Bondarenko, V. E. (2019). A Mathematical Model of the Human Cardiac Na^+ Channel. *The Journal of membrane biology*, *252*(1), 77–103.

Asfaw, T. N., Tyan, L., Glukhov, A. V., & Bondarenko, V. E. (2020). A compartmentalized mathematical model of mouse atrial myocytes. *American journal of physiology. Heart and circulatory physiology*, *318*(3), H485–H507.

Babu, G. J., Bhupathy, P., Timofeyev, V., Petrashevskaya, N. N., Reiser, P. J., Chiamvimonvat, N., & Periasamy, M. (2007). Ablation of sarcolipin enhances sarcoplasmic reticulum calcium transport and atrial contractility. *Proceedings of the National Academy of Sciences of the United States of America*, *104*(45), 17867–17872.

Baker A. J. (2014). Adrenergic signaling in heart failure: a balance of toxic and protective effects. *Pflugers Archiv : European journal of physiology*, *466*(6), 1139–1150.

Balut, C. M., Hamilton, K. L., & Devor, D. C. (2012). Trafficking of intermediate (KCa3.1) and small (KCa2.x) conductance, Ca(2+)-activated K(+) channels: a novel target for medicinal chemistry efforts?. *ChemMedChem*, *7*(10), 1741–1755.

Bao, Y., Willis, B. C., Frasier, C. R., Lopez-Santiago, L. F., Lin, X., Ramos-Mondragón, R., Auerbach, D. S., Chen, C., Wang, Z., Anumonwo, J., Valdivia, H. H., Delmar, M., Jalife, J., & Isom, L. L. (2016). Scn2b Deletion in Mice Results in Ventricular and Atrial Arrhythmias. *Circulation. Arrhythmia and electrophysiology*, *9*(12), e003923.

Baranchuk, A., Glover, B.M., Ho, S.Y., Sanchez-Quintana, D., Brugada, P. (2021). Cardiac Anatomy and Electrophysiology. In: Glover B.M., Brugada P. (eds) Clinical Handbook of Cardiac Electrophysiology. *Springer, Cham*.

Bartoli, F., Bailey, M. A., Rode, B., Mateo, P., Antigny, F., Bedouet, K., Gerbaud, P., Gosain, R., Plante, J., Norman, K., Gomez, S., Lefebvre, F., Rucker-Martin, C., Ainscough, J., Kearney, M. T., Bruns, A. F., Shi, J., Appleby, H. L., Young, R. S., Shawer, H. M., … Sabourin, J. (2020). Orai1 Channel Inhibition Preserves Left Ventricular Systolic Function and Normal Ca^{2+} Handling After Pressure Overload. *Circulation, 141*(3), 199–216.

Bartos, D. C., Grandi, E., & Ripplinger, C. M. (2015). Ion Channels in the Heart. *Comprehensive Physiology, 5*(3), 1423–1464.

Bean B. P. (1985). Two kinds of calcium channels in canine atrial cells. Differences in kinetics, selectivity, and pharmacology. *The Journal of general physiology*, *86*(1), 1–30.

Berecki, G., Zegers, J. G., Bhuiyan, Z. A., Verkerk, A. O., Wilders, R., & van Ginneken, A. C. (2006). Long-QT syndrome-related sodium channel mutations probed by the dynamic action potential clamp technique. *The Journal of physiology, 570*(Pt 2), 237–250.

Bers D. M. (2002). Cardiac excitation-contraction coupling. *Nature, 415*(6868), 198–205.

Bers D. M. (2000). Calcium fluxes involved in control of cardiac myocyte contraction. *Circ Res. 87*(4): 275-281.

Bers, D. M., Eisner, D. A., & Valdivia, H. H. (2003). Sarcoplasmic reticulum Ca2+ and heart failure: roles of diastolic leak and Ca^{2+} transport. *Circulation research, 93*(6), 487–490.

Bers, D. M., Pogwizd, S. M., & Schlotthauer, K. (2002). Upregulated Na/Ca exchange is involved in both contractile dysfunction and arrhythmogenesis in heart failure. *Basic research in cardiology*, *97 Suppl 1*, I36–I42.

Beuckelmann, D. J., Näbauer, M., & Erdmann, E. (1992). Intracellular calcium handling in isolated ventricular myocytes from patients with terminal heart failure. *Circulation*, *85*(3), 1046–1055.

Bing, O. H., Brooks, W. W., Conrad, C. H., Sen, S., Perreault, C. L., & Morgan, J. P. (1991). Intracellular calcium transients in myocardium from spontaneously hypertensive rats during the transition to heart failure. *Circulation research*, *68*(5), 1390–1400.

Bondarenko V. E. (2014). A compartmentalized mathematical model of the β1-adrenergic signaling system in mouse ventricular myocytes. *PloS one*, *9*(2), e89113.

Bondarenko, V. E., Szigeti, G. P., Bett, G. C., Kim, S. J., & Rasmusson, R. L. (2004). Computer model of action potential of mouse ventricular myocytes. *American journal of physiology. Heart and circulatory physiology*, *287*(3), H1378–H1403.

Bovo, E., Mazurek, S. R., Blatter, L. A., & Zima, A. V. (2011). Regulation of sarcoplasmic reticulum Ca^{2+} leak by cytosolic Ca^{2+} in rabbit ventricular myocytes. *The Journal of physiology*, *589*(Pt 24), 6039–6050.

Brandenburg, S., Kohl, T., Williams, G. S., Gusev, K., Wagner, E., Rog-Zielinska, E. A., Hebisch, E., Dura, M., Didié, M., Gotthardt, M., Nikolaev, V. O., Hasenfuss, G., Kohl, P., Ward, C. W., Lederer, W. J., & Lehnart, S. E. (2016). Axial tubule junctions control rapid calcium signaling in atria. *The Journal of clinical investigation*, *126*(10), 3999–4015.

Brandenburg, S., Pawlowitz, J., Fakuade, F. E., Kownatzki-Danger, D., Kohl, T., Mitronova, G. Y., Scardigli, M., Neef, J., Schmidt, C., Wiedmann, F., Pavone, F. S., Sacconi, L., Kutschka, I., Sossalla, S., Moser, T., Voigt, N., & Lehnart, S. E. (2018). Axial Tubule Junctions Activate Atrial Ca^{2+} Release Across Species. *Frontiers in physiology*, *9*, 1227.

Brandt, M. C., Priebe, L., Böhle, T., Südkamp, M., & Beuckelmann, D. J. (2000). The ultrarapid and the transient outward K(+) current in human atrial fibrillation. Their possible role in postoperative atrial fibrillation. *Journal of molecular and cellular cardiology*, *32*(10), 1885–1896.

Bristow, M. R., Hershberger, R. E., Port, J. D., Minobe, W., & Rasmussen, R. (1989). Beta 1- and beta 2-adrenergic receptor-mediated adenylate cyclase stimulation in nonfailing and failing human ventricular myocardium. *Molecular pharmacology, 35*(3), 295–303.

Brodde O. E. (1991). Beta 1- and beta 2-adrenoceptors in the human heart: properties, function, and alterations in chronic heart failure. *Pharmacological reviews*, *43*(2), 203–242.

Bryant, S. M., Kong, C. H., Watson, J., Cannell, M. B., James, A. F., & Orchard, C. H. (2015). Altered distribution of ICa impairs Ca release at the t-tubules of ventricular myocytes from failing hearts. *Journal of molecular and cellular cardiology, 86*, 23–31.

Bryant, S. M., Kong, C., Watson, J. J., Gadeberg, H. C., James, A. F., Cannell, M. B., & Orchard, C. H. (2018). Caveolin 3-dependent loss of t-tubular ICa during hypertrophy and heart failure in mice. *Experimental physiology, 103*(5), 652–665.

Cai, B., Zhang, Y., Zhao, Y., Wang, J., Li, T., Zhang, Y., Jiang, Y., Jin, X., Xue, G., Li, P., Sun, Y., Huang, Q., Zhang, X., Su, W., Yang, Y., Sun, Y., Shi, L., Li, X., Lu, Y., Yang, B., … Pan, Z. (2019). Long Noncoding RNA-DACH1 (Dachshund Homolog 1) Regulates Cardiac Function by Inhibiting SERCA2a (Sarcoplasmic Reticulum Calcium ATPase 2a). *Hypertension (Dallas, Tex. : 1979), 74*(4), 833–842.

Cerrone, M., Noujaim, S. F., Tolkacheva, E. G., Talkachou, A., O'Connell, R., Berenfeld, O., Anumonwo, J., Pandit, S. V., Vikstrom, K., Napolitano, C., Priori, S. G., & Jalife, J. (2007).

Arrhythmogenic mechanisms in a mouse model of catecholaminergic polymorphic ventricular tachycardia. *Circulation research*, *101*(10), 1039–1048.

Chen, H. H., Wang, S. N., Cao, T. T., Zheng, J. L., Tian, J., Shan, X. L., Zhao, P., Guo, W., Xu, M., Zhang, C., & Lu, R. (2020). Stachydrine hydrochloride alleviates pressure overload-induced heart failure and calcium mishandling on mice. *Journal of ethnopharmacology*, *248*, 112306.

Coronel, R., Wilders, R., Verkerk, A. O., Wiegerinck, R. F., Benoist, D., & Bernus, O. (2013). Electrophysiological changes in heart failure and their implications for arrhythmogenesis. *Biochimica et biophysica acta, 1832*(12), 2432–2441.

Correll, R. N., Eder, P., Burr, A. R., Despa, S., Davis, J., Bers, D. M., & Molkentin, J. D. (2014). Overexpression of the Na+/K+ ATPase α2 but not α1 isoform attenuates pathological cardiac hypertrophy and remodeling. *Circulation research, 114*(2), 249–256.

Courtemanche, M., Ramirez, R. J., & Nattel, S. (1998). Ionic mechanisms underlying human atrial action potential properties: insights from a mathematical model. *The American journal of physiology*, *275*(1), H301–H321.

Curran, J., Musa, H., Kline, C. F., Makara, M. A., Little, S. C., Higgins, J. D., Hund, T. J., Band, H., & Mohler, P. J. (2015). Eps15 Homology Domain-containing Protein 3 Regulates Cardiac T-type Ca^{2+} Channel Targeting and Function in the Atria. *The Journal of biological chemistry*, *290*(19), 12210–12221.

Danik, S., Cabo, C., Chiello, C., Kang, S., Wit, A. L., & Coromilas, J. (2002). Correlation of repolarization of ventricular monophasic action potential with ECG in the murine heart. *American journal of physiology. Heart and circulatory physiology*, *283*(1), H372–H381.

Davies, L., Jin, J., Shen, W., Tsui, H., Shi, Y., Wang, Y., Zhang, Y., Hao, G., Wu, J., Chen, S., Fraser, J. A., Dong, N., Christoffels, V., Ravens, U., Huang, C. L., Zhang, H., Cartwright, E. J., Wang, X., & Lei, M. (2014). Mkk4 is a negative regulator of the transforming growth factor beta 1 signaling associated with atrial remodeling and arrhythmogenesis with age. *Journal of the American Heart Association*, *3*(2), e000340.

de Lucia, C., Eguchi, A., & Koch, W. J. (2018). New Insights in Cardiac β-Adrenergic Signaling During Heart Failure and Aging. *Frontiers in pharmacology, 9,* 904.

del Monte, F., Hajjar, R.J. (2008). Intracellular devastation in heart failure. *Heart Fail Rev 13:* 151–162.

Demir, S. S., Clark, J. W., Murphey, C. R., & Giles, W. R. (1994). A mathematical model of a rabbit sinoatrial node cell. *The American journal of physiology*, *266*(3 Pt 1), C832–C852.

Dibb, K. M., Clarke, J. D., Horn, M. A., Richards, M. A., Graham, H. K., Eisner, D. A., & Trafford, A. W. (2009). Characterization of an extensive transverse tubular network in sheep atrial myocytes and its depletion in heart failure. *Circulation. Heart failure*, *2*(5), 482–489.

Diness, J. G., Bentzen, B. H., Sørensen, U. S., & Grunnet, M. (2015). Role of Calcium-activated Potassium Channels in Atrial Fibrillation Pathophysiology and Therapy. *Journal of cardiovascular pharmacology*, *66*(5), 441–448.

Diness, J. G., Sørensen, U. S., Nissen, J. D., Al-Shahib, B., Jespersen, T., Grunnet, M., & Hansen, R. S. (2010). Inhibition of small-conductance Ca2+-activated K+ channels terminates and protects against atrial fibrillation. *Circulation. Arrhythmia and electrophysiology*, *3*(4), 380–390.

Dong, C., Wang, Y., Ma, A., & Wang, T. (2020). Life Cycle of the Cardiac Voltage-Gated Sodium Channel NaV1.5. *Frontiers in physiology, 11,* 609733.

Edvardsson, N., Hirsch, I., & Olsson, S. B. (1984). Right ventricular monophasic action potentials in healthy young men. Pacing and clinical electrophysiology : *PACE, 7*(5), 813–821.

Eisner, D. A., Caldwell, J. L., Kistamás, K., & Trafford, A. W. (2017). Calcium and Excitation-Contraction Coupling in the Heart. *Circulation research*, *121*(2), 181–195.

Eisner, D. A., Caldwell, J. L., Trafford, A. W., & Hutchings, D. C. (2020). The Control of Diastolic Calcium in the Heart: Basic Mechanisms and Functional Implications. *Circulation research, 126*(3), 395–412.

El Refaey, M., Musa, H., Murphy, N. P., Lubbers, E. R., Skaf, M., Han, M., Cavus, O., Koenig, S. N., Wallace, M. J., Gratz, D., Bradley, E., Alsina, K. M., Wehrens, X., Hund, T. J., & Mohler, P. J. (2019). Protein Phosphatase 2A Regulates Cardiac Na^+ Channels. *Circulation research, 124*(5), 737–746.

Engelhardt, S., Hein, L., Wiesmann, F., & Lohse, M. J. (1999). Progressive hypertrophy and heart failure in beta1-adrenergic receptor transgenic mice. *Proceedings of the National Academy of Sciences of the United States of America*, *96*(12), 7059–7064.

Esposito, G., Rapacciuolo, A., Naga Prasad, S. V., Takaoka, H., Thomas, S. A., Koch, W. J., & Rockman, H. A. (2002). Genetic alterations that inhibit in vivo pressure-overload hypertrophy prevent cardiac dysfunction despite increased wall stress. *Circulation, 105*(1), 85–92.

Fabritz, L., Damke, D., Emmerich, M., Kaufmann, S. G., Theis, K., Blana, A., Fortmüller, L., Laakmann, S., Hermann, S., Aleynichenko, E., Steinfurt, J., Volkery, D., Riemann, B., Kirchhefer, U., Franz, M. R., Breithardt, G., Carmeliet, E., Schäfers, M., Maier, S. K., Carmeliet, P., … Kirchhof, P. (2010) Autonomic modulation and antiarrhythmic therapy in a model of long QT syndrome type 3. *Cardiovascular research, 87*(1), 60–72.

Feldman, A. M., Cates, A. E., Veazey, W. B., Hershberger, R. E., Bristow, M. R., Baughman, K. L., Baumgartner, W. A., & Van Dop, C. (1988). Increase of the 40,000-mol wt pertussis toxin substrate (G protein) in the failing human heart. *The Journal of clinical investigation, 82*(1), 189–197.

Forbes, M. S., Van Niel, E. E., & Purdy-Ramos, S. I. (1990). The atrial myocardial cells of mouse heart: a structural and stereological study. *Journal of structural biology*, *103*(3), 266–279.

Frank, K. F., Bölck, B., Erdmann, E., & Schwinger, R. H. (2003). Sarcoplasmic reticulum Ca2+-ATPase modulates cardiac contraction and relaxation. *Cardiovascular research, 57*(1), 20–27.

Frank, K., & Kranias, E. G. (2000). Phospholamban and cardiac contractility. *Annals of medicine, 32*(8), 572–578.

Frisk, M., Koivumäki, J. T., Norseng, P. A., Maleckar, M. M., Sejersted, O. M., & Louch, W. E. (2014). Variable t-tubule organization and Ca2+ homeostasis across the atria. *American journal of physiology. Heart and circulatory physiology*, *307*(4), H609–H620.

Gaborit, N., Le Bouter, S., Szuts, V., Varro, A., Escande, D., Nattel, S., & Demolombe, S. (2007). Regional and tissue specific transcript signatures of ion channel genes in the non-diseased human heart. *The Journal of physiology*, *582*(Pt 2), 675–693.

Giles, W. R., & Imaizumi, Y. (1988). Comparison of potassium currents in rabbit atrial and ventricular cells. *The Journal of physiology*, *405*, 123–145.

Ginsburg, K. S., & Bers, D. M. (2004). Modulation of excitation-contraction coupling by isoproterenol in cardiomyocytes with controlled SR Ca2+ load and Ca2+ current trigger. *The Journal of physiology*, *556*(Pt 2), 463–480.

Glukhov, A. V., Balycheva, M., Sanchez-Alonso, J. L., Ilkan, Z., Alvarez-Laviada, A., Bhogal, N., Diakonov, I., Schobesberger, S., Sikkel, M. B., Bhargava, A., Faggian, G., Punjabi, P. P., Houser, S. R., & Gorelik, J. (2015). Direct Evidence for Microdomain-Specific Localization and Remodeling of Functional L-Type Calcium Channels in Rat and Human Atrial Myocytes. *Circulation, 132*(25), 2372–2384.

Glukhov, A. V., Kalyanasundaram, A., Lou, Q., Hage, L. T., Hansen, B. J., Belevych, A. E., Mohler, P. J., Knollmann, B. C., Periasamy, M., Györke, S., & Fedorov, V. V. (2015). Calsequestrin 2 deletion causes sinoatrial node dysfunction and atrial arrhythmias associated with altered sarcoplasmic reticulum calcium cycling and degenerative fibrosis within the mouse atrial pacemaker complex1. *European heart journal*, *36*(11), 686–697.

Glynn, P., Musa, H., Wu, X., Unudurthi, S. D., Little, S., Qian, L., Wright, P. J., Radwanski, P. B., Gyorke, S., Mohler, P. J., & Hund, T. J. (2015). Voltage-Gated Sodium Channel Phosphorylation at Ser571 Regulates Late Current, Arrhythmia, and Cardiac Function In Vivo. *Circulation, 132*(7), 567–577.

Gomez J. F., Cardona K., Trenor B. (2015). Lessons learned from multi-scale modeling of the failing heart. *J Mol Cell Cardiol. 89*(Pt B): 146-59.

Grandi, E., Pandit, S. V., Voigt, N., Workman, A. J., Dobrev, D., Jalife, J., & Bers, D. M. (2011). Human atrial action potential and Ca2+ model: sinus rhythm and chronic atrial fibrillation. *Circulation research*, *109*(9), 1055–1066.

Grandi, E., Pasqualini, F. S., & Bers, D. M. (2010). A novel computational model of the human ventricular action potential and Ca transient. *Journal of molecular and cellular cardiology*, *48*(1), 112–121.

Grandi, E., Sanguinetti, M. C., Bartos, D. C., Bers, D. M., Chen-Izu, Y., Chiamvimonvat, N., Colecraft, H. M., Delisle, B. P., Heijman, J., Navedo, M. F., Noskov, S., Proenza, C., Vandenberg, J. I., & Yarov-Yarovoy, V. (2017). Potassium channels in the heart: structure, function and regulation. *The Journal of physiology, 595*(7), 2209–2228.

Grant A. O. (2009). Cardiac ion channels. *Circ Arrhythm Electrophysiol 2(2):* 185-194.

Grinshpon, M., & Bondarenko, V. E. (2016). Simulation of the effects of moderate stimulation/inhibition of the β1-adrenergic signaling system and its components in mouse ventricular myocytes. *American journal of physiology. Cell physiology*, *310*(11), C844–C856.

Groenke, S., Larson, E. D., Alber, S., Zhang, R., Lamp, S. T., Ren, X., Nakano, H., Jordan, M. C., Karagueuzian, H. S., Roos, K. P., Nakano, A., Proenza, C., Philipson, K. D., & Goldhaber, J. I. (2013). Complete atrial-specific knockout of sodium-calcium exchange eliminates sinoatrial node pacemaker activity. *PloS one*, *8*(11), e81633.

Grote-Wessels, S., Baba, H. A., Boknik, P., El-Armouche, A., Fabritz, L., Gillmann, H. J., Kucerova, D., Matus, M., Müller, F. U., Neumann, J., Schmitz, M., Stümpel, F., Theilmeier, G., Wohlschlaeger, J., Schmitz, W., & Kirchhefer, U. (2008). Inhibition of protein phosphatase 1 by inhibitor-2 exacerbates progression of cardiac failure in a model with pressure overload. *Cardiovascular research, 79*(3), 464–471.

Györke, I., & Györke, S. (1998). Regulation of the cardiac ryanodine receptor channel by luminal Ca2+ involves luminal Ca^{2+} sensing sites. *Biophysical journal, 75(6), 2801–2810.*

Györke, S., Stevens, S. C., & Terentyev, D. (2009). Cardiac calsequestrin: quest inside the SR. *The Journal of physiology, 587*(Pt 13), 3091–3094.

Hancock, J. M., Weatherall, K. L., Choisy, S. C., James, A. F., Hancox, J. C., & Marrion, N. V. (2015). Selective activation of heteromeric SK channels contributes to action potential repolarization in mouse atrial myocytes. *Heart rhythm*, *12*(5), 1003–1015.

Harmrell B. B. (2018). Cardiovascular Physiology, 1st ed. *Taylor and Francis, New York.*

Haverinen, J., & Vornanen, M. (2009). Comparison of sarcoplasmic reticulum calcium content in atrial and ventricular myocytes of three fish species. *American journal of physiology. Regulatory, integrative and comparative physiology*, *297*(4), R1180–R1187.

Heijman, J., Erfanian Abdoust, P., Voigt, N., Nattel, S., & Dobrev, D. (2016). Computational models of atrial cellular electrophysiology and calcium handling, and their role in atrial fibrillation. *The Journal of physiology*, *594*(3), 537–553.

Hilal-Dandan, R., Kanter, J. R., & Brunton, L. L. (2000). Characterization of G-protein signaling in ventricular myocytes from the adult mouse heart: differences from the rat. *Journal of molecular and cellular cardiology, 32*(7), 1211–1221.

Hilgemann, D. W., & Noble, D. (1987). Excitation-contraction coupling and extracellular calcium transients in rabbit atrium: reconstruction of basic cellular mechanisms. *Proceedings of the Royal Society of London. Series B, Biological sciences*, *230*(1259), 163–205.

Hirschberg, B., Maylie, J., Adelman, J. P., & Marrion, N. V. (1998). Gating of recombinant small-conductance Ca-activated K^+ channels by calcium. *The Journal of general physiology*, *111*(4), 565–581.

Hobai, I. A., & O'Rourke, B. (2001). Decreased sarcoplasmic reticulum calcium content is responsible for defective excitation-contraction coupling in canine heart failure. *Circulation, 103*(11), 1577–1584.

Hoeflich K. P, Ikura M. (2002). Calmodulin in action: diversity in target recognition and activation mechanisms. *Cell. 108*(6), 739-42.

Horvath, B., & Bers, D. M. (2014). The late sodium current in heart failure: pathophysiology and clinical relevance. *ESC heart failure, 1*(1), 26–40.

Houser, S. R., Margulies, K. B., Murphy, A. M., Spinale, F. G., Francis, G. S., Prabhu, S. D., Rockman, H. A., Kass, D. A., Molkentin, J. D., Sussman, M. A., Koch, W. J., & American Heart Association Council on Basic Cardiovascular Sciences, Council on Clinical Cardiology, and Council on Functional Genomics and Translational Biology (2012). Animal models of heart failure: a scientific statement from the American Heart Association. *Circulation research, 111*(1), 131–150.

Hua, R., Adamczyk, A., Robbins, C., Ray, G., & Rose, R. A. (2012). Distinct patterns of constitutive phosphodiesterase activity in mouse sinoatrial node and atrial myocardium. *PloS one*, *7*(10), e47652.

Hua, R., MacLeod, S. L., Polina, I., Moghtadaei, M., Jansen, H. J., Bogachev, O., O'Blenes, S. B., Sapp, J. L., Legare, J. F., & Rose, R. A. (2015). Effects of Wild-Type and Mutant Forms of Atrial Natriuretic Peptide on Atrial Electrophysiology and Arrhythmogenesis. *Circulation. Arrhythmia and electrophysiology*, *8*(5), 1240–1254.

Hume, J. R., & Uehara, A. (1985). Ionic basis of the different action potential configurations of single guinea-pig atrial and ventricular myocytes. *The Journal of physiology*, *368*, 525–544.

Hund, T. J., & Rudy, Y. (2004). Rate dependence and regulation of action potential and calcium transient in a canine cardiac ventricular cell model. *Circulation, 110*(20), 3168–3174.

Hutchings, D. C., Madders, G., Niort, B. C., Bode, E. F., Waddell, C. A., Woods, L. S., Dibb, K. M., Eisner, D. A., & Trafford, A. W. (2022). Interaction of background Ca^{2+} influx, sarcoplasmic reticulum threshold and heart failure in determining propensity for Ca^{2+} waves in sheep heart. *The Journal of physiology*, 10.1113/JP282168.

Iancu, R. V., Jones, S. W., & Harvey, R. D. (2007). Compartmentation of cAMP signaling in cardiac myocytes: a computational study. *Biophysical journal*, *92*(9), 3317–3331.

Ito, K., Yan, X., Tajima, M., Su, Z., Barry, W. H., & Lorell, B. H. (2000). Contractile reserve and intracellular calcium regulation in mouse myocytes from normal and hypertrophied failing hearts. *Circulation research, 87*(7), 588–595.

Jafri, M. S., Rice, J. J., & Winslow, R. L. (1998). Cardiac Ca2+ dynamics: the roles of ryanodine receptor adaptation and sarcoplasmic reticulum load. *Biophysical journal*, *74*(3), 1149–1168.

Jaleel, N., Nakayama, H., Chen, X., Kubo, H., MacDonnell, S., Zhang, H., Berretta, R., Robbins, J., Cribbs, L., Molkentin, J. D., & Houser, S. R. (2008). Ca^{2+} influx through T- and L-type Ca^{2+} channels have different effects on myocyte contractility and induce unique cardiac phenotypes. *Circulation research*, *103*(10), 1109–1119.

Janse M. J. (2004). Electrophysiological changes in heart failure and their relationship to arrhythmogenesis. *Cardiovascular research*, *61*(2), 208–217.

Jansen, H. J., Mackasey, M., Moghtadaei, M., Belke, D. D., Egom, E. E., Tuomi, J. M., Rafferty, S. A., Kirkby, A. W., & Rose, R. A. (2018). Distinct patterns of atrial electrical and structural remodeling in angiotensin II mediated atrial fibrillation. *Journal of molecular and cellular cardiology*, *124*, 12–25.

Kaese S., Verheule S. (2012). Cardiac electrophysiology in mice: a matter of size. *Front Physiol. 3,* 345.

Kamp, T. J., & He, J. Q. (2002). L-type Ca^{2+} channels gaining respect in heart failure. *Circulation research, 91*(6), 451–453.

Kashimura, T., Briston, S. J., Trafford, A. W., Napolitano, C., Priori, S. G., Eisner, D. A., & Venetucci, L. A. (2010). In the RyR2(R4496C) mouse model of CPVT, β-adrenergic stimulation induces Ca waves by increasing SR Ca content and not by decreasing the threshold for Ca waves. *Circulation research, 107*(12), 1483–1489.

Keizer, J., & Levine, L. (1996). Ryanodine receptor adaptation and Ca^{2+}(-)induced Ca^{2+} release-dependent Ca^{2+} oscillations. *Biophysical journal*, *71*(6), 3477–3487.

Kennedy, M., Bers, D. M., Chiamvimonvat, N., & Sato, D. (2017). Dynamical effects of calcium-sensitive potassium currents on voltage and calcium alternans. *The Journal of physiology*, *595*(7), 2285–2297.

Kernik, D. C., Morotti, S., Wu, H., Garg, P., Duff, H. J., Kurokawa, J., Jalife, J., Wu, J. C., Grandi, E., & Clancy, C. E. (2019). A computational model of induced pluripotent stem-cell derived cardiomyocytes incorporating experimental variability from multiple data sources. *The Journal of physiology*, *597*(17), 4533–4564.

Kho, C., Lee, A., Jeong, D., Oh, J. G., Chaanine, A. H., Kizana, E., Park, W. J., & Hajjar, R. J. (2011). SUMO1-dependent modulation of SERCA2a in heart failure. *Nature, 477*(7366), 601–605.

Kistamás, K., Hézső, T., Horváth, B., & Nánási, P. P. (2021). Late sodium current and calcium homeostasis in arrhythmogenesis. *Channels (Austin, Tex.), 15*(1), 1–19.

Kitchens, S. A., Burch, J., & Creazzo, T. L. (2003). T-type Ca^{2+} current contribution to Ca^{2+}-induced Ca^{2+} release in developing myocardium. *Journal of molecular and cellular cardiology*, *35*(5), 515–523.

Klabunde R. E. (2012). Cardiovascular Physiology Concepts. 2nd ed. *Lippincott Williams & Wilkins, New York.* https://www.cvphysiology.com/

Kneller, J., Ramirez, R. J., Chartier, D., Courtemanche, M., & Nattel, S. (2002). Time-dependent transients in an ionically based mathematical model of the canine atrial action potential. *American journal of physiology. Heart and circulatory physiology*, *282*(4), H1437–H1451.

Kociol, R. D., Pang, P. S., Gheorghiade, M., Fonarow, G. C., O'Connor, C. M., & Felker, G. M. (2010). Troponin elevation in heart failure prevalence, mechanisms, and clinical implications. *Journal of the American College of Cardiology, 56*(14), 1071–1078.

Kodirov, S. A., Brunner, M., Nerbonne, J. M., Buckett, P., Mitchell, G. F., & Koren, G. (2004). Attenuation of $I_{K,slow1}$ and $I_{K,slow2}$ in Kv1/Kv2DN mice prolongs APD and QT intervals but does not suppress spontaneous or inducible arrhythmias. *American journal of physiology. Heart and circulatory physiology*, *286*(1), H368–H374.

Koivumäki, J. T., Korhonen, T., & Tavi, P. (2011). Impact of sarcoplasmic reticulum calcium release on calcium dynamics and action potential morphology in human atrial myocytes: a computational study. *PLoS computational biology*, *7*(1), e1001067.

Konstam, M. A., Kramer, D. G., Patel, A. R., Maron, M. S., & Udelson, J. E. (2011). Left ventricular remodeling in heart failure: current concepts in clinical significance and assessment. JACC. *Cardiovascular imaging, 4*(1), 98–108.

Kranias EG, Hajjar R. J. (2012). Modulation of cardiac contractility by the phospholamban/SERCA2a regulatome. *Circ Res. 110*(12), 1646–1660.

Kurata, Y., Hisatome, I., Matsuda, H., & Shibamoto, T. (2005). Dynamical mechanisms of pacemaker generation in IK1-downregulated human ventricular myocytes: insights from bifurcation analyses of a mathematical model. *Biophysical journal*, *89*(4), 2865–2887.

LaRocca, T. J., Seeger, T., Prado, M., Perea-Gil, I., Neofytou, E., Mecham, B. H., Ameen, M., Chang, A., Pandey, G., Wu, J. C., & Karakikes, I. (2020). Pharmacological Silencing of MicroRNA-152 Prevents Pressure Overload-Induced Heart Failure. *Circulation. Heart failure, 13*(3), e006298.

Lemire, I., Allen, B. G., Rindt, H., & Hebert, T. E. (1998). Cardiac-specific overexpression of alpha1BAR regulates betaAR activity via molecular crosstalk. *Journal of molecular and cellular cardiology*, *30*(9), 1827–1839.

Lenaerts, I., Bito, V., Heinzel, F. R., Driesen, R. B., Holemans, P., D'hooge, J., Heidbüchel, H., Sipido, K. R., & Willems, R. (2009). Ultrastructural and functional remodeling of the coupling between Ca2+ influx and sarcoplasmic reticulum Ca2+ release in right atrial myocytes from experimental persistent atrial fibrillation. *Circulation research*, *105*(9), 876–885.

Li, G. R., Feng, J., Wang, Z., Fermini, B., & Nattel, S. (1996). Adrenergic modulation of ultrarapid delayed rectifier K+ current in human atrial myocytes. *Circulation research*, *78*(5), 903–915.

Li, M. X., Hwang P. M. (2015). Structure and function of cardiac troponin C (TNNC1): Implications for heart failure, cardiomyopathies, and troponin modulating drugs. *Gene. 571*(2), 153-166.

Li, N., Timofeyev, V., Tuteja, D., Xu, D., Lu, L., Zhang, Q., Zhang, Z., Singapuri, A., Albert, T. R., Rajagopal, A. V., Bond, C. T., Periasamy, M., Adelman, J., & Chiamvimonvat, N. (2009). Ablation of a Ca^{2+}-activated K+ channel (SK2 channel) results in action potential prolongation in atrial myocytes and atrial fibrillation. *The Journal of physiology*, *587*(Pt 5), 1087–1100.

Li, R. C., Tao, J., Guo, Y. B., Wu, H. D., Liu, R. F., Bai, Y., Lv, Z. Z., Luo, G. Z., Li, L. L., Wang, M., Yang, H. Q., Gao, W., Han, Q. D., Zhang, Y. Y., Wang, X. J., Xu, M., & Wang, S. Q. (2013). In vivo suppression of microRNA-24 prevents the transition toward decompensated hypertrophy in aortic-constricted mice. *Circulation research, 112*(4), 601–605.

Li, X., Zima, A. V., Sheikh, F., Blatter, L. A., & Chen, J. (2005). Endothelin-1-induced arrhythmogenic Ca2+ signaling is abolished in atrial myocytes of inositol-1,4,5-trisphosphate(IP3)-receptor type 2-deficient mice. *Circulation research*, *96*(12), 1274–1281.

Li, Y., Wang, F., Zhang, X., Qi, Z., Tang, M., Szeto, C., Li, Y., Zhang, H., & Chen, X. (2012). β-Adrenergic stimulation increases Cav3.1 activity in cardiac myocytes through protein kinase A. *PloS one*, *7*(7), e39965.

Li, Y., Zhang, X., Zhang, C., Zhang, X., Li, Y., Qi, Z., Szeto, C., Tang, M., Peng, Y., Molkentin, J. D., Houser, S. R., Xie, M., & Chen, X. (2018). Increasing T-type calcium channel activity by β-adrenergic stimulation contributes to β-adrenergic regulation of heart rates. *The Journal of physiology*, *596*(7), 1137–1151.

Lindblad, D. S., Murphey, C. R., Clark, J. W., & Giles, W. R. (1996). A model of the action potential and underlying membrane currents in a rabbit atrial cell. *The American journal of physiology*, *271*(4 Pt 2), H1666–H1696.

Lindner, M., Erdmann, E., & Beuckelmann, D. J. (1998). Calcium content of the sarcoplasmic reticulum in isolated ventricular myocytes from patients with terminal heart failure. *Journal of molecular and cellular cardiology*, *30*(4), 743–749.

Lipp, P., & Niggli, E. (1994). Sodium current-induced calcium signals in isolated guinea-pig ventricular myocytes. *The Journal of physiology*, *474*(3), 439–446.

Lipskaia, L., Hadri, L., Le Prince, P., Esposito, B., Atassi, F., Liang, L., Glorian, M., Limon, I., Lompre, A. M., Lehoux, S., & Hajjar, R. J. (2013). SERCA2a gene transfer prevents intimal proliferation in an organ culture of human internal mammary artery. *Gene therapy, 20*(4), 396–406.

Liu, J., Laksman, Z., & Backx, P. H. (2016). The electrophysiological development of cardiomyocytes. *Advanced drug delivery reviews, 96*, 253–273.

Liu, N., Denegri, M., Ruan, Y., Avelino-Cruz, J. E., Perissi, A., Negri, S., Napolitano, C., Coetzee, W. A., Boyden, P. A., & Priori, S. G. (2011). Short communication: flecainide exerts an antiarrhythmic effect in a mouse model of catecholaminergic polymorphic ventricular tachycardia by increasing the threshold for triggered activity. *Circulation research, 109*(3), 291–295.

Ljubojevic-Holzer, S., Herren, A. W., Djalinac, N., Voglhuber, J., Morotti, S., Holzer, M., Wood, B. M., Abdellatif, M., Matzer, I., Sacherer, M., Radulovic, S., Wallner, M., Ivanov, M., Wagner, S., Sossalla, S., von Lewinski, D., Pieske, B., Brown, J. H., Sedej, S., Bossuyt, J.,

… Bers, D. M. (2020). CaMKIIδC Drives Early Adaptive Ca2+ Change and Late Eccentric Cardiac Hypertrophy. *Circulation research, 127*(9), 1159–1178.

Lohse, M. J., Engelhardt S., & Eschenhagen T. (2003). What is the role of beta-adrenergic signaling in heart failure? *Circ Res. 93*(10), 896-906.

Lomax, A. E., Kondo, C. S., & Giles, W. R. (2003). Comparison of time- and voltage-dependent K+ currents in myocytes from left and right atria of adult mice. *American journal of physiology. Heart and circulatory physiology*, *285*(5), H1837–H1848.

London, B., Guo, W., Pan Xh, Lee, J. S., Shusterman, V., Rocco, C. J., Logothetis, D. A., Nerbonne, J. M., & Hill, J. A. (2001). Targeted replacement of KV1.5 in the mouse leads to loss of the 4-aminopyridine-sensitive component of I(K,slow) and resistance to drug-induced qt prolongation. *Circulation research*, *88*(9), 940–946.

Lu, L., Zhang, Q., Timofeyev, V., Zhang, Z., Young, J. N., Shin, H. S., Knowlton, A. A., & Chiamvimonvat, N. (2007). Molecular coupling of a Ca^{2+}-activated K+ channel to L-type Ca^{2+} channels via alpha-actinin2. *Circulation research*, *100*(1), 112–120.

Lu, Y. M., Huang, J., Shioda, N., Fukunaga, K., Shirasaki, Y., Li, X. M., & Han, F. (2011). CaMKIIδB mediates aberrant NCX1 expression and the imbalance of NCX1/SERCA in transverse aortic constriction-induced failing heart. *PloS one, 6*(9), e24724.

Lukyanenko, V., Györke, I., & Györke, S. (1996). Regulation of calcium release by calcium inside the sarcoplasmic reticulum in ventricular myocytes. Pflugers Archiv : *European journal of physiology, 432*(6), 1047–1054.

Luo, C. H., & Rudy, Y. (1994). A dynamic model of the cardiac ventricular action potential. I. Simulations of ionic currents and concentration changes. *Circulation research*, *74*(6), 1071–1096.

Lüss, I., Boknik, P., Jones, L. R., Kirchhefer, U., Knapp, J., Linck, B., Lüss, H., Meissner, A., Müller, F. U., Schmitz, W., Vahlensieck, U., & Neumann, J. (1999). Expression of cardiac calcium regulatory proteins in atrium v ventricle in different species. *Journal of molecular and cellular cardiology*, *31*(6), 1299–1314.

Madamanchi, A. (2007). Beta-adrenergic receptor signaling in cardiac function and heart failure. *Mcgill J Med. 10(2), 99-104.*

Maier, L. S. & Bers, D. M. (2007). Role of Ca^{2+}/calmodulin-dependent protein kinase (CaMK) in excitation-contraction coupling in the heart. *Cardiovasc Res. 73*(4): 631-40.

Maltsev, V. A., & Undrovinas, A. (2008). Late sodium current in failing heart: friend or foe?. *Progress in biophysics and molecular biology*, *96*(1-3), 421–451.

Mancarella, S., Yue, Y., Karnabi, E., Qu, Y., El-Sherif, N., & Boutjdir, M. (2008). Impaired Ca2+ homeostasis is associated with atrial fibrillation in the alpha1D L-type Ca2+ channel KO mouse. *American journal of physiology. Heart and circulatory physiology*, *295*(5), H2017–H2024.

Marionneau, C., Brunet, S., Flagg, T. P., Pilgram, T. K., Demolombe, S., & Nerbonne, J. M. (2008). Distinct cellular and molecular mechanisms underlie functional remodeling of repolarizing K+ currents with left ventricular hypertrophy. *Circulation research, 102*(11), 1406–1415.

Markandeya, Y. S., Fahey, J. M., Pluteanu, F., Cribbs, L. L., & Balijepalli, R. C. (2011). Caveolin-3 regulates protein kinase A modulation of the Ca(V)3.2 (alpha1H) T-type Ca2+ channels. *The Journal of biological chemistry*, *286*(4), 2433–2444.

Marks, A. R. (2013). Calcium cycling proteins and heart failure: mechanisms and therapeutics. J *Clin Invest. 123*(1), 46-52.

Martínez, M. L., Heredia, M. P., & Delgado, C. (1999). Expression of T-type Ca(2+) channels in ventricular cells from hypertrophied rat hearts. *Journal of molecular and cellular cardiology*, *31*(9), 1617–1625.

Marx, S. O., Reiken, S., Hisamatsu, Y., Jayaraman, T., Burkhoff, D., Rosemblit, N., & Marks, A. R. (2000). PKA phosphorylation dissociates FKBP12.6 from the calcium release channel (ryanodine receptor): defective regulation in failing hearts. *Cell*, *101*(4), 365–376.

Matsuda, J. J., Lee, H. C., & Shibata, E. F. (1993). Acetylcholine reversal of isoproterenol-stimulated sodium currents in rabbit ventricular myocytes. *Circulation research*, *72*(3), 517–525.

McCabe, K. J., & Rangamani, P. (2021). Computational modeling approaches to cAMP/PKA signaling in cardiomyocytes. *Journal of molecular and cellular cardiology, 154,* 32–40.

McDonald, R. L., Colyer, J., & Harrison, S. M. (2000). Quantitative analysis of Na^{+}-Ca^{2+} exchanger expression in guinea-pig heart. *European journal of biochemistry*, *267*(16), 5142–5148.

Mesirca, P., Torrente, A. G., & Mangoni, M. E. (2015). Functional role of voltage gated Ca^{2+} channels in heart automaticity. *Frontiers in physiology*, *6*, 19.

Messer, A. E., & Marston, S. B. (2014). Investigating the role of uncoupling of troponin I phosphorylation from changes in myofibrillar Ca(2+)-sensitivity in the pathogenesis of cardiomyopathy. *Frontiers in physiology, 5,* 315.

Milano, C. A., Allen, L. F., Rockman, H. A., Dolber, P. C., McMinn, T. R., Chien, K. R., Johnson, T. D., Bond, R. A., & Lefkowitz, R. J. (1994). Enhanced myocardial function in transgenic mice overexpressing the beta 2-adrenergic receptor. *Science (New York, N.Y.)*, *264*(5158), 582–586.

Mohamed, B. A., Hartmann, N., Tirilomis, P., Sekeres, K., Li, W., Neef, S., Richter, C., Zeisberg, E. M., Kattner, L., Didié, M., Guan, K., Schmitto, J. D., Lehnart, S. E., Luther, S., Voigt, N., Seidler, T., Sossalla, S., Hasenfuss, G., & Toischer, K. (2018). Sarcoplasmic reticulum calcium leak contributes to arrhythmia but not to heart failure progression. *Science translational medicine, 10*(458), eaan0724.

Mora, M. T., Ferrero, J. M., Romero, L., & Trenor, B. (2017). Sensitivity analysis revealing the effect of modulating ionic mechanisms on calcium dynamics in simulated human heart failure. *PloS one, 12*(11), e0187739.

Mora, M. T., Gong, J., Sobie, E. A., & Trenor, B. (2021). The role of β-adrenergic system remodeling in human heart failure: A mechanistic investigation. *Journal of molecular and cellular cardiology, 153*, 14–25.

Näbauer, M., & Kääb, S. (1998). Potassium channel down-regulation in heart failure. *Cardiovascular research, 37*(2), 324–334.

Nagy, N., Szuts, V., Horváth, Z., Seprényi, G., Farkas, A. S., Acsai, K., Prorok, J., Bitay, M., Kun, A., Pataricza, J., Papp, J. G., Nánási, P. P., Varró, A., & Tóth, A. (2009). Does small-conductance calcium-activated potassium channel contribute to cardiac repolarization?. *Journal of molecular and cellular cardiology*, *47*(5), 656–663.

Najafi, A., Sequeira, V., Kuster, D. W., & van der Velden, J. (2016). β-adrenergic receptor signalling and its functional consequences in the diseased heart. *European journal of clinical investigation, 46*(4), 362–374.

Nakamura, H., Ding, W. G., Sanada, M., Maeda, K., Kawai, H., Maegawa, H., & Matsuura, H. (2010). Presence and functional role of the rapidly activating delayed rectifier K(+) current in left and right atria of adult mice. *European journal of pharmacology*, *649*(1-3), 14–22.

Nattel, S. (2008). Effects of heart disease on cardiac ion current density versus current amplitude: important conceptual subtleties in the language of arrhythmogenic ion channel remodeling. *Circulation research, 102*(11), 1298–1300.

Nattel, S., Maguy, A., Le Bouter, S., & Yeh, Y. H. (2007). Arrhythmogenic ion-channel remodeling in the heart: heart failure, myocardial infarction, and atrial fibrillation. *Physiological reviews, 87*(2), 425–456.

Nerbonne J. M. (2004). Studying cardiac arrhythmias in the mouse--a reasonable model for probing mechanisms?. *Trends in cardiovascular medicine*, *14*(3), 83–93.

Nerbonne, J. M., & Kass, R. S. (2005). Molecular physiology of cardiac repolarization. *Physiological reviews, 85*(4), 1205–1253.

Ng, S. Y., Wong, C. K., & Tsang, S. Y. (2010). Differential gene expressions in atrial and ventricular myocytes: insights into the road of applying embryonic stem cell-derived cardiomyocytes for future therapies. *American journal of physiology. Cell physiology*, *299*(6), C1234–C1249.

Nie, J., Duan, Q., He, M., Li, X., Wang, B., Zhou, C., Wu, L., Wen, Z., Chen, C., Wang, D. W., Alsina, K. M., Wehrens, X., Wang, D. W., & Ni, L. (2019). Ranolazine prevents pressure overload-induced cardiac hypertrophy and heart failure by restoring aberrant Na+ and Ca^{2+} handling. *Journal of cellular physiology, 234*(7), 11587–11601.

Nienaber, J. J., Tachibana, H., Naga Prasad, S. V., Esposito, G., Wu, D., Mao, L., & Rockman, H. A. (2003). Inhibition of receptor-localized PI3K preserves cardiac beta-adrenergic receptor function and ameliorates pressure overload heart failure. *The Journal of clinical investigation, 112*(7), 1067–1079.

Nikolaev, V. O., Moshkov, A., Lyon, A. R., Miragoli, M., Novak, P., Paur, H., Lohse, M. J., Korchev, Y. E., Harding, S. E., & Gorelik, J. (2010). Beta2-adrenergic receptor redistribution in heart failure changes cAMP compartmentation. *Science (New York, N.Y.), 327*(5973), 1653–1657.

Nilius, B., Hess, P., Lansman, J. B., & Tsien, R. W. (1985). A novel type of cardiac calcium channel in ventricular cells. *Nature*, *316*(6027), 443–446.

Niwa, N., Yasui, K., Opthof, T., Takemura, H., Shimizu, A., Horiba, M., Lee, J. K., Honjo, H., Kamiya, K., & Kodama, I. (2004). $Ca_v3.2$ subunit underlies the functional T-type Ca^{2+} channel in murine hearts during the embryonic period. *American journal of physiology. Heart and circulatory physiology*, *286*(6), H2257–H2263.

Norman, R. A. A. (2016), Remodeling of the cardiac caveolar domain in heart failure and its putative influence on beta adrenergic signaling. *Doctoral dissertation, University of Leeds, Leeds, United Kingdom*.

Nygren, A., Fiset, C., Firek, L., Clark, J. W., Lindblad, D. S., Clark, R. B., & Giles, W. R. (1998). Mathematical model of an adult human atrial cell: the role of K^+ currents in repolarization. *Circulation research*, *82*(1), 63–81.

Ono, M., Yano, M., Hino, A., Suetomi, T., Xu, X., Susa, T., Uchinoumi, H., Tateishi, H., Oda, T., Okuda, S., Doi, M., Kobayashi, S., Yamamoto, T., Koseki, N., Kyushiki, H., Ikemoto, N., & Matsuzaki, M. (2010). Dissociation of calmodulin from cardiac ryanodine receptor causes aberrant Ca^{2+} release in heart failure. *Cardiovascular research, 87*(4), 609–617.

O'Rourke, B., Kass, D. A., Tomaselli, G. F., Kääb, S., Tunin, R., & Marbán, E. (1999). Mechanisms of altered excitation-contraction coupling in canine tachycardia-induced heart failure, I: experimental studies. *Circulation research*, *84*(5), 562–570.

Pappano, A. J., Wier, W. G. (2019). Automaticity: natural excitation of the heart. In: Cardiovascular physiology. 11th ed. *Mosby, Elsevier* p. 86–140.

Pelá, G., Missale, C., Raddino, R., Condorelli, E., Spano, P. F., & Visioli, O. (1990). Beta 1- and beta 2-receptors are differentially desensitized in an experimental model of heart failure. *Journal of cardiovascular pharmacology, 16*(5), 839–846.

Perino, A., Ghigo, A., Ferrero, E., Morello, F., Santulli, G., Baillie, G. S., Damilano, F., Dunlop, A. J., Pawson, C., Walser, R., Levi, R., Altruda, F., Silengo, L., Langeberg, L. K., Neubauer, G., Heymans, S., Lembo, G., Wymann, M. P., Wetzker, R., Houslay, M. D., … Hirsch, E. (2011). Integrating cardiac PIP3 and cAMP signaling through a PKA anchoring function of p110γ. *Molecular cell, 42*(1), 84–95.

Petkova-Kirova, P. S., London, B., Salama, G., Rasmusson, R. L., & Bondarenko, V. E. (2012). Mathematical modeling mechanisms of arrhythmias in transgenic mouse heart overexpressing TNF-α. *American journal of physiology. Heart and circulatory physiology*, *302*(4), H934–H952.

Philippaert, K., Kalyaanamoorthy, S., Fatehi, M., Long, W., Soni, S., Byrne, N. J., Barr, A., Singh, J., Wong, J., Palechuk, T., Schneider, C., Darwesh, A. M., Maayah, Z. H., Seubert, J. M., Barakat, K., Dyck, J., & Light, P. E. (2021). Cardiac Late Sodium Channel Current Is a Molecular Target for the Sodium/Glucose Cotransporter 2 Inhibitor Empagliflozin. *Circulation, 143*(22), 2188–2204.

Piacentino, V., 3rd, Weber, C. R., Chen, X., Weisser-Thomas, J., Margulies, K. B., Bers, D. M., & Houser, S. R. (2003). Cellular basis of abnormal calcium transients of failing human ventricular myocytes. *Circulation research*, *92*(6), 651–658.

Pieske, B., Maier, L. S., Bers, D. M., & Hasenfuss, G. (1999). Ca2+ handling and sarcoplasmic reticulum Ca2+ content in isolated failing and nonfailing human myocardium. *Circulation research*, *85*(1), 38–46.

Pogwizd, S. M., & Bers, D. M. (2004). Cellular basis of triggered arrhythmias in heart failure. *Trends in cardiovascular medicine*, *14*(2), 61–66.

Poláková, E., & Sobie, E. A. (2013). Alterations in T-tubule and dyad structure in heart disease: challenges and opportunities for computational analyses. *Cardiovascular research, 98*(2), 233–239.

Pott, C., Muszynski, A., Ruhe, M., Bögeholz, N., Schulte, J. S., Milberg, P., Mönnig, G., Fabritz, L., Goldhaber, J. I., Breithardt, G., Schmitz, W., Philipson, K. D., Eckardt, L., Kirchhof, P., & Müller, F. U. (2012). Proarrhythmia in a non-failing murine model of cardiac-specific Na+/Ca 2+ exchanger overexpression: whole heart and cellular mechanisms. *Basic research in cardiology*, *107*(2), 247.

Pourrier, M., Williams, S., McAfee, D., Belardinelli, L., & Fedida, D. (2014). CrossTalk proposal: The late sodium current is an important player in the development of diastolic heart failure (heart failure with a preserved ejection fraction). *The Journal of physiology, 592*(3), 411–414.

Priebe, L., & Beuckelmann, D. J. (1998). Simulation study of cellular electric properties in heart failure. *Circulation research, 82*(11), 1206–1223.

Rahm, A. K., Lugenbiel, P., Schweizer, P. A., Katus, H. A., & Thomas, D. (2018). Role of ion channels in heart failure and channelopathies. *Biophysical reviews, 10*(4), 1097–1106.

Ramirez, R. J., Nattel, S., & Courtemanche, M. (2000). Mathematical analysis of canine atrial action potentials: rate, regional factors, and electrical remodeling. *American journal of physiology. Heart and circulatory physiology*, *279*(4), H1767–H1785.

Rasmusson, R. L., Clark, J. W., Giles, W. R., Robinson, K., Clark, R. B., Shibata, E. F., & Campbell, D. L. (1990). A mathematical model of electrophysiological activity in a bullfrog atrial cell. *The American journal of physiology*, *259*(2 Pt 2), H370–H389.

Reinecke, H., Studer, R., Vetter, R., Holtz, J., & Drexler, H. (1996). Cardiac Na+/Ca2+ exchange activity in patients with end-stage heart failure. *Cardiovascular research*, *31*(1), 48–54.

Ren, Y., Barnwell, L. F., Alexander, J. C., Lubin, F. D., Adelman, J. P., Pfaffinger, P. J., Schrader, L. A., & Anderson, A. E. (2006). Regulation of surface localization of the small conductance Ca^{2+}-activated potassium channel, Sk2, through direct phosphorylation by cAMP-dependent protein kinase. *The Journal of biological chemistry*, *281*(17), 11769–11779.

Richard, S., Leclercq, F., Lemaire, S., Piot, C., & Nargeot, J. (1998). Ca^{2+} currents in compensated hypertrophy and heart failure. *Cardiovascular research, 37*(2), 300–311.

Richards, M. A., Clarke, J. D., Saravanan, P., Voigt, N., Dobrev, D., Eisner, D. A., Trafford, A. W., & Dibb, K. M. (2011). Transverse tubules are a common feature in large mammalian atrial myocytes including human. *American journal of physiology. Heart and circulatory physiology*, *301*(5), H1996–H2005.

Riehle, C., & Bauersachs, J. (2019). Small animal models of heart failure. *Cardiovascular research, 115*(13), 1838–1849.

Rivaud, M. R., Agullo-Pascual, E., Lin, X., Leo-Macias, A., Zhang, M., Rothenberg, E., Bezzina, C. R., Delmar, M., & Remme, C. A. (2017). Sodium Channel Remodeling in Subcellular

Microdomains of Murine Failing Cardiomyocytes. *Journal of the American Heart Association, 6*(12), e007622.

Rivaud, M. R., Baartscheer, A., Verkerk, A. O., Beekman, L., Rajamani, S., Belardinelli, L., Bezzina, C. R., & Remme, C. A. (2018). Enhanced late sodium current underlies pro-arrhythmic intracellular sodium and calcium dysregulation in murine sodium channelopathy. *International journal of cardiology, 263*, 54–62.

Rozier, K., & Bondarenko, V. E. (2017). Distinct physiological effects of β_1- and β_2-adrenoceptors in mouse ventricular myocytes: insights from a compartmentalized mathematical model. *American journal of physiology. Cell physiology*, *312*(5), C595–C623.

Sanchez-Alonso, J. L., Bhargava, A., O'Hara, T., Glukhov, A. V., Schobesberger, S., Bhogal, N., Sikkel, M. B., Mansfield, C., Korchev, Y. E., Lyon, A. R., Punjabi, P. P., Nikolaev, V. O., Trayanova, N. A., & Gorelik, J. (2016). Microdomain-Specific Modulation of L-Type Calcium Channels Leads to Triggered Ventricular Arrhythmia in Heart Failure. *Circulation research, 119*(8), 944–955.

Satin, J., & Cribbs, L. L. (2000). Identification of a T-type Ca(2+) channel isoform in murine atrial myocytes (AT-1 cells). *Circulation research*, *86*(6), 636–642.

Schaper, J., Kostin, S., Hein, S., Elsässer, A., Arnon, E., & Zimmermann, R. (2002). Structural remodelling in heart failure. *Experimental and clinical cardiology, 7*(2-3), 64–68.

Schwinger, R. H., Böhm, M., Schmidt, U., Karczewski, P., Bavendiek, U., Flesch, M., Krause, E. G., & Erdmann, E. (1995). Unchanged protein levels of SERCA II and phospholamban but reduced Ca2+ uptake and Ca(2+)-ATPase activity of cardiac sarcoplasmic reticulum from dilated cardiomyopathy patients compared with patients with nonfailing hearts. *Circulation*, *92*(11), 3220–3228.

Serrano, J. R., Perez-Reyes, E., & Jones, S. W. (1999). State-dependent inactivation of the alpha1G T-type calcium channel. *The Journal of general physiology*, *114*(2), 185–201.

Shannon, T. R., Wang, F., & Bers, D. M. (2005). Regulation of cardiac sarcoplasmic reticulum Ca release by luminal [Ca] and altered gating assessed with a mathematical model. *Biophysical journal, 89*(6), 4096–4110.

Shannon, T. R., Wang, F., Puglisi, J., Weber, C., & Bers, D. M. (2004). A mathematical treatment of integrated Ca dynamics within the ventricular myocyte. *Biophysical journal*, *87*(5), 3351–3371.

Shaw, R. M., & Colecraft, H. M. (2013). L-type calcium channel targeting and local signalling in cardiac myocytes. *Cardiovascular research, 98*(2), 177–186.

Signore, S., Sorrentino, A., Borghetti, G., Cannata', A., Meo, M., Zhou, Y., Kannappan, R., Pasqualini, F.S., O'Malley, H.A., Sundman, M., Tsigkas, N., Zhang, E.Y., Arranto, C.A., Mangiaracina, C., Isobe, K., Sena, B.F., Kim, J., Goichberg, P., Nahrendorf, M., Isom, L.L., Leri, A., Anversa, P., & Rota, M. (2015). Late Na+ current and protracted electrical recovery are critical determinants of the aging myopathy. *Nature Communications, 6.*

Sipido, K. R., Carmeliet, E., & Van de Werf, F. (1998). T-type Ca^{2+} current as a trigger for Ca^{2+} release from the sarcoplasmic reticulum in guinea-pig ventricular myocytes. *The Journal of physiology*, *508*(Pt 2), 439–451.

Smyrnias, I., Mair, W., Harzheim, D., Walker, S. A., Roderick, H. L., & Bootman, M. D. (2010). Comparison of the T-tubule system in adult rat ventricular and atrial myocytes, and its role in excitation-contraction coupling and inotropic stimulation. *Cell calcium*, *47*(3), 210–223.

Sobie E. A. (2009). Parameter sensitivity analysis in electrophysiological models using multivariable regression. *Biophysical journal*, *96*(4), 1264–1274.

Song, L. S., Sobie, E. A., McCulle, S., Lederer, W. J., Balke, C. W., & Cheng, H. (2006). Orphaned ryanodine receptors in the failing heart. *Proceedings of the National Academy of Sciences of the United States of America, 103*(11), 4305–4310.

Spannbauer, A., Traxler, D., Zlabinger, K., Gugerell, A., Winkler, J., Mester-Tonczar, J., Lukovic, D., Müller, C., Riesenhuber, M., Pavo, N., & Gyöngyösi, M. (2019). Large Animal Models of Heart Failure With Reduced Ejection Fraction (HFrEF). *Frontiers in cardiovascular medicine, 6*, 117.

Sprenger, J. U., Perera, R. K., Steinbrecher, J. H., Lehnart, S. E., Maier, L. S., Hasenfuss, G., & Nikolaev, V. O. (2015). In vivo model with targeted cAMP biosensor reveals changes in receptor-microdomain communication in cardiac disease. *Nature communications, 6*, 6965.

Tachibana, H., Naga Prasad, S. V., Lefkowitz, R. J., Koch, W. J., & Rockman, H. A. (2005). Level of beta-adrenergic receptor kinase 1 inhibition determines degree of cardiac dysfunction after chronic pressure overload-induced heart failure. *Circulation, 111*(5), 591–597.

Talavera, K., Janssens, A., Klugbauer, N., Droogmans, G., & Nilius, B. (2003). Extracellular Ca^{2+} modulates the effects of protons on gating and conduction properties of the T-type Ca^{2+} channel alpha1G (CaV3.1). *The Journal of general physiology*, *121*(6), 511–528.

Talavera, K., Janssens, A., Klugbauer, N., Droogmans, G., & Nilius, B. (2003). Pore structure influences gating properties of the T-type Ca^{2+} channel alpha1G. *The Journal of general physiology*, *121*(6), 529–540.

Talavera, K., Staes, M., Janssens, A., Droogmans, G., & Nilius, B. (2004). Mechanism of arachidonic acid modulation of the T-type Ca2+ channel alpha1G. *The Journal of general physiology*, *124*(3), 225–238.

Tamargo, J., Caballero, R., Gómez, R., Valenzuela, C., & Delpón, E. (2004). Pharmacology of cardiac potassium channels. *Cardiovascular research, 62*(1), 9–33.

Tamayo, M., Martín-Nunes, L., Val-Blasco, A., G M-Piedras, M. J., Navarro-García, J. A., Lage, E., Prieto, P., Ruiz-Hurtado, G., Fernández-Velasco, M., & Delgado, C. (2020). Beneficial effects of paricalcitol on cardiac dysfunction and remodelling in a model of established heart failure. *British journal of pharmacology, 177*(14), 3273–3290.

ten Tusscher, K. H., Noble, D., Noble, P. J., & Panfilov, A. V. (2004). A model for human ventricular tissue. *American journal of physiology. Heart and circulatory physiology*, *286*(4), H1573–H1589.

Tepe, N. M., & Liggett, S. B. (1999). Transgenic replacement of type V adenylyl cyclase identifies a critical mechanism of beta-adrenergic receptor dysfunction in the G alpha q overexpressing mouse. *FEBS letters*, *458*(2), 236–240.

Toischer, K., Hartmann, N., Wagner, S., Fischer, T. H., Herting, J., Danner, B. C., Sag, C. M., Hund, T. J., Mohler, P. J., Belardinelli, L., Hasenfuss, G., Maier, L. S., & Sossalla, S. (2013). Role of late sodium current as a potential arrhythmogenic mechanism in the progression of pressure-induced heart disease. *Journal of molecular and cellular cardiology, 61*, 111–122.

Toischer, K., Rokita, A. G., Unsöld, B., Zhu, W., Kararigas, G., Sossalla, S., Reuter, S. P., Becker, A., Teucher, N., Seidler, T., Grebe, C., Preuss, L., Gupta, S. N., Schmidt, K., Lehnart, S. E., Krüger, M., Linke, W. A., Backs, J., Regitz-Zagrosek, V., Schäfer, K., … Hasenfuss, G. (2010). *Differential cardiac remodeling in preload versus afterload. Circulation, 122*(10), 993–1003.

Tomaselli, G. F., & Marbán, E. (1999). Electrophysiological remodeling in hypertrophy and heart failure. *Cardiovascular research, 42*(2), 270–283.

Tong, X., Porter, L. M., Liu, G., Dhar-Chowdhury, P., Srivastava, S., Pountney, D. J., Yoshida, H., Artman, M., Fishman, G. I., Yu, C., Iyer, R., Morley, G. E., Gutstein, D. E., & Coetzee, W. A. (2006). Consequences of cardiac myocyte-specific ablation of KATP channels in transgenic mice expressing dominant negative Kir6 subunits. *American journal of physiology. Heart and circulatory physiology*, *291*(2), H543–H551.

Trenor, B., Cardona, K., Saiz, J., Noble, D., & Giles, W. (2017). Cardiac action potential repolarization revisited: early repolarization shows all-or-none behaviour. *The Journal of physiology*, *595*(21), 6599–6612.

Tuteja, D., Xu, D., Timofeyev, V., Lu, L., Sharma, D., Zhang, Z., Xu, Y., Nie, L., Vázquez, A. E., Young, J. N., Glatter, K. A., & Chiamvimonvat, N. (2005). Differential expression of small-conductance Ca2+-activated K+ channels SK1, SK2, and SK3 in mouse atrial and ventricular myocytes. *American journal of physiology. Heart and circulatory physiology*, *289*(6), H2714–H2723.

Ufret-Vincenty, C. A., Baro, D. J., Lederer, W. J., Rockman, H. A., Quinones, L. E., & Santana, L. F. (2001). Role of sodium channel deglycosylation in the genesis of cardiac arrhythmias in heart failure. *The Journal of biological chemistry, 276*(30), 28197–28203.

Undrovinas, A., Maltsev, V. A., & Sabbah, H. N. (2013). Calpain inhibition reduces amplitude and accelerates decay of the late sodium current in ventricular myocytes from dogs with chronic heart failure. *PloS one, 8*(4), e54436.

Undrovinas, N. A., Maltsev, V. A., Belardinelli, L., Sabbah, H. N., & Undrovinas, A. (2010). Late sodium current contributes to diastolic cell Ca^{2+} accumulation in chronic heart failure. *The journal of physiological sciences : JPS, 60*(4), 245–257.

Ungerer, M., Böhm, M., Elce, J. S., Erdmann, E., & Lohse, M. J. (1993). Altered expression of beta-adrenergic receptor kinase and beta 1-adrenergic receptors in the failing human heart. *Circulation, 87*(2), 454–463.

Vaidyanathan, R., O'Connell, R. P., Deo, M., Milstein, M. L., Furspan, P., Herron, T. J., Pandit, S. V., Musa, H., Berenfeld, O., Jalife, J., & Anumonwo, J. M. (2013). The ionic bases of the action potential in isolated mouse cardiac Purkinje cell. *Heart rhythm*, *10*(1), 80–87.

Valdivia, C. R., Chu, W. W., Pu, J., Foell, J. D., Haworth, R. A., Wolff, M. R., Kamp, T. J., & Makielski, J. C. (2005). Increased late sodium current in myocytes from a canine heart failure model and from failing human heart. *Journal of molecular and cellular cardiology, 38*(3), 475–483.

van Oort, R. J., Garbino, A., Wang, W., Dixit, S. S., Landstrom, A. P., Gaur, N., De Almeida, A. C., Skapura, D. G., Rudy, Y., Burns, A. R., Ackerman, M. J., & Wehrens, X. H. (2011). Disrupted junctional membrane complexes and hyperactive ryanodine receptors after acute junctophilin knockdown in mice. *Circulation, 123*(9), 979–988.

van Oort, R. J., McCauley, M. D., Dixit, S. S., Pereira, L., Yang, Y., Respress, J. L., Wang, Q., De Almeida, A. C., Skapura, D. G., Anderson, M. E., Bers, D. M., & Wehrens, X. H. (2010). Ryanodine receptor phosphorylation by calcium/calmodulin-dependent protein kinase II promotes life-threatening ventricular arrhythmias in mice with heart failure. *Circulation*, *122*(25), 2669–2679.

van Oort, R. J., Respress, J. L., Li, N., Reynolds, C., De Almeida, A. C., Skapura, D. G., De Windt, L. J., & Wehrens, X. H. (2010). Accelerated development of pressure overload-induced cardiac hypertrophy and dysfunction in an RyR2-R176Q knockin mouse model. *Hypertension (Dallas, Tex. : 1979), 55*(4), 932–938.

Vassort, G., Talavera, K., & Alvarez, J. L. (2006). Role of T-type Ca2+ channels in the heart. *Cell calcium*, *40*(2), 205–220.

Vinet, L., Pezet, M., Bito, V., Briec, F., Biesmans, L., Rouet-Benzineb, P., Gellen, B., Prévilon, M., Chimenti, S., Vilaine, J. P., Charpentier, F., Sipido, K. R., & Mercadier, J. J. (2012). Cardiac FKBP12.6 overexpression protects against triggered ventricular tachycardia in pressure overloaded mouse hearts. *Basic research in cardiology, 107*(2), 246.

Volonte, D., McTiernan, C. F., Drab, M., Kasper, M., & Galbiati, F. (2008). Caveolin-1 and caveolin-3 form heterooligomeric complexes in atrial cardiac myocytes that are required for doxorubicin-induced apoptosis. *American journal of physiology. Heart and circulatory physiology*, *294*(1), H392–H401.

Wachter, S. B., & Gilbert, E. M. (2012). Beta-adrenergic receptors, from their discovery and characterization through their manipulation to beneficial clinical application. *Cardiology, 122*(2), 104–112.

Walden, A. P., Dibb, K. M., & Trafford, A. W. (2009). Differences in intracellular calcium homeostasis between atrial and ventricular myocytes. *Journal of molecular and cellular cardiology*, *46*(4), 463–473.

Walker, C. A., & Spinale, F. G. (1999). The structure and function of the cardiac myocyte: a review of fundamental concepts. *The Journal of thoracic and cardiovascular surgery*, *118*(2), 375–382.

Walweel, K., Gomez-Hurtado, N., Rebbeck, R. T., Oo, Y. W., Beard, N. A., Molenaar, P., Dos Remedios, C., van Helden, D. F., Cornea, R. L., Knollmann, B. C., & Laver, D. R. (2019). Calmodulin inhibition of human RyR2 channels requires phosphorylation of RyR2-S2808 or RyR2-S2814. *Journal of molecular and cellular cardiology, 130*, 96–106.

Wang, H., Kohr, M. J., Wheeler, D. G., & Ziolo, M. T. (2008). Endothelial nitric oxide synthase decreases beta-adrenergic responsiveness via inhibition of the L-type Ca^{2+} current. American journal of physiology. *Heart and circulatory physiology, 294*(3), H1473–H1480.

Wang, J., Schwinger, R. H., Frank, K., Müller-Ehmsen, J., Martin-Vasallo, P., Pressley, T. A., Xiang, A., Erdmann, E., & McDonough, A. A. (1996). Regional expression of sodium pump subunits isoforms and Na^{+}-Ca^{++} exchanger in the human heart. *The Journal of clinical investigation*, *98*(7), 1650–1658.

Wansapura, A. N., Lasko, V. M., Lingrel, J. B., & Lorenz, J. N. (2011). Mice expressing ouabain-sensitive α1-Na,K-ATPase have increased susceptibility to pressure overload-induced cardiac hypertrophy. *American journal of physiology. Heart and circulatory physiology, 300*(1), H347–H355.

Wei, S., Guo, A., Chen, B., Kutschke, W., Xie, Y. P., Zimmerman, K., Weiss, R. M., Anderson, M. E., Cheng, H., & Song, L. S. (2010). T-tubule remodeling during transition from hypertrophy to heart failure. *Circulation research*, *107*(4), 520–531.

Wilson, G. G., O'Neill, C. A., Sivaprasadarao, A., Findlay, J. B., & Wray, D. (1994). Modulation by protein kinase A of a cloned rat brain potassium channel expressed in Xenopus oocytes. *Pflugers Archiv : European journal of physiology*, *428*(2), 186–193.

Winslow, R. L., Rice, J., Jafri, S., Marbán, E., & O'Rourke, B. (1999). Mechanisms of altered excitation-contraction coupling in canine tachycardia-induced heart failure, II: model studies. *Circulation research*, *84*(5), 571–586.

Woo, A. Y., & Xiao, R. P. (2012). β-Adrenergic receptor subtype signaling in heart: from bench to bedside. *Acta pharmacologica Sinica, 33*(3), 335–341.

Wright, P. T., Nikolaev, V. O., O'Hara, T., Diakonov, I., Bhargava, A., Tokar, S., Schobesberger, S., Shevchuk, A. I., Sikkel, M. B., Wilkinson, R., Trayanova, N. A., Lyon, A. R., Harding, S. E., & Gorelik, J. (2014). Caveolin-3 regulates compartmentation of cardiomyocyte beta2-adrenergic receptor-mediated cAMP signaling. *Journal of molecular and cellular cardiology, 67*, 38–48.

Wu, H. D., Xu, M., Li, R. C., Guo, L., Lai, Y. S., Xu, S. M., Li, S. F., Lü, Q. L., Li, L. L., Zhang, H. B., Zhang, Y. Y., Zhang, C. M., & Wang, S. Q. (2012). Ultrastructural remodelling of Ca(2+) signalling apparatus in failing heart cells. *Cardiovascular research, 95*(4), 430–438.

Wu, Y., Temple, J., Zhang, R., Dzhura, I., Zhang, W., Trimble, R., Roden, D. M., Passier, R., Olson, E. N., Colbran, R. J., & Anderson, M. E. (2002). Calmodulin kinase II and arrhythmias in a mouse model of cardiac hypertrophy. *Circulation*, *106*(10), 1288–1293.

Xu, H., Li, H., & Nerbonne, J. M. (1999). Elimination of the transient outward current and action potential prolongation in mouse atrial myocytes expressing a dominant negative Kv4 alpha subunit. *The Journal of physiology*, *519 Pt 1*(Pt 1), 11–21.

Xu, Y., Tuteja, D., Zhang, Z., Xu, D., Zhang, Y., Rodriguez, J., Nie, L., Tuxson, H. R., Young, J. N., Glatter, K. A., Vázquez, A. E., Yamoah, E. N., & Chiamvimonvat, N. (2003).

Molecular identification and functional roles of a Ca(2+)-activated K+ channel in human and mouse hearts. *The Journal of biological chemistry*, *278*(49), 49085–49094.

Yancy, C. W., Jessup, M., Bozkurt, B., Butler, J., Casey, D. E., Jr, Drazner, M. H., Fonarow, G. C., Geraci, S. A., Horwich, T., Januzzi, J. L., Johnson, M. R., Kasper, E. K., Levy, W. C., Masoudi, F. A., McBride, P. E., McMurray, J. J., Mitchell, J. E., Peterson, P. N., Riegel, B., Sam, F., … Wilkoff, B. L. (2013). 2013 ACCF/AHA guideline for the management of heart failure: executive summary: a report of the American College of Cardiology Foundation/American Heart Association Task Force on practice guidelines. *Circulation, 128*(16), 1810–1852.

Yang, D., Song, L. S., Zhu, W. Z., Chakir, K., Wang, W., Wu, C., Wang, Y., Xiao, R. P., Chen, S. R., & Cheng, H. (2003). Calmodulin regulation of excitation-contraction coupling in cardiac myocytes. *Circulation research, 92*(6), 659–667.

Yang, Y., Guo, T., Oda, T., Chakraborty, A., Chen, L., Uchinoumi, H., Knowlton, A. A., Fruen, B. R., Cornea, R. L., Meissner, G., & Bers, D. M. (2014). Cardiac myocyte Z-line calmodulin is mainly RyR2-bound, and reduction is arrhythmogenic and occurs in heart failure. *Circulation research, 114*(2), 295–306.

Yi, F., Ling, T. Y., Lu, T., Wang, X. L., Li, J., Claycomb, W. C., Shen, W. K., & Lee, H. C. (2015). Down-regulation of the small conductance calcium-activated potassium channels in diabetic mouse atria. *The Journal of biological chemistry*, *290*(11), 7016–7026.

Yoo, B., Lemaire, A., Mangmool, S., Wolf, M. J., Curcio, A., Mao, L., & Rockman, H. A. (2009). Beta1-adrenergic receptors stimulate cardiac contractility and CaMKII activation in vivo and enhance cardiac dysfunction following myocardial infarction. American journal of physiology. *Heart and circulatory physiology, 297*(4), H1377–H1386.

Yu, S., Li, G., Huang, C. L., Lei, M., & Wu, L. (2018). Late sodium current associated cardiac electrophysiological and mechanical dysfunction. *Pflugers Archiv : European journal of physiology, 470*(3), 461–469.

Yu, T., Deng, C., Wu, R., Guo, H., Zheng, S., Yu, X., Shan, Z., Kuang, S., & Lin, Q. (2012). Decreased expression of small-conductance Ca^{2+}-activated K^{+} channels SK1 and SK2 in human chronic atrial fibrillation. *Life sciences*, *90*(5-6), 219–227.

Yue, X., Zhang, R., Kim, B., Ma, A., Philipson, K. D., & Goldhaber, J. I. (2017). Heterogeneity of transverse-axial tubule system in mouse atria: Remodeling in atrial-specific Na^{+}-Ca^{2+} exchanger knockout mice. *Journal of molecular and cellular cardiology*, *108*, 50–60.

Zaragoza, C., Gomez-Guerrero, C., Martin-Ventura, J. L., Blanco-Colio, L., Lavin, B., Mallavia, B., Tarin, C., Mas, S., Ortiz, A., & Egido, J. (2011). Animal models of cardiovascular diseases. *Journal of biomedicine & biotechnology, 2011*, 497841.

Zhang, X. D., Coulibaly, Z. A., Chen, W. C., Ledford, H. A., Lee, J. H., Sirish, P., Dai, G., Jian, Z., Chuang, F., Brust-Mascher, I., Yamoah, E. N., Chen-Izu, Y., Izu, L. T., & Chiamvimonvat, N. (2018). Coupling of SK channels, L-type Ca^{2+} channels, and ryanodine receptors in cardiomyocytes. *Scientific reports*, *8*(1), 4670.

Zhang, X. D., Timofeyev, V., Li, N., Myers, R. E., Zhang, D. M., Singapuri, A., Lau, V. C., Bond, C. T., Adelman, J., Lieu, D. K., & Chiamvimonvat, N. (2014). Critical roles of a small conductance Ca^{2+}-activated K^{+} channel (SK3) in the repolarization process of atrial myocytes. *Cardiovascular research*, *101*(2), 317–325.

Zhou, J., Kodirov, S., Murata, M., Buckett, P. D., Nerbonne, J. M., & Koren, G. (2003). Regional upregulation of Kv2.1-encoded current, IK,slow2, in Kv1DN mice is abolished by

crossbreeding with Kv2DN mice. *American journal of physiology. Heart and circulatory physiology*, *284*(2), H491–H500.

Zhou, M. H., Yang, G., Jiao, S., Hu, C. L., & Mei, Y. A. (2012). Cholesterol enhances neuron susceptibility to apoptotic stimuli via cAMP/PKA/CREB-dependent up-regulation of Kv2.1. *Journal of neurochemistry*, *120*(4), 502–514.

Zhou, Z., & Lipsius, S. L. (1994). T-type calcium current in latent pacemaker cells isolated from cat right atrium. *Journal of molecular and cellular cardiology*, *26*(9), 1211–1219.

Zhu, W., Woo, A. Y., Zhang, Y., Cao, C. M., & Xiao, R. P. (2011). β-adrenergic receptor subtype signaling in the heart: from bench to the bedside. *Current topics in membranes, 67*, 191–204.

APPENDICES

Appendix A: Atrial Model Parameters and Equations

Appendix A.1 T-type Ca^{2+} Current (I_{CaT})

Parameter	Definition	Value
k_{CaTpv}	Forward activation rate constant between closed states	9,500exp(V/15.0) s^{-1}
k_{CaTmv}	Backward activation rate constant between closed states	32.0exp(–V/18.0) s^{-1}
k_{CaTpo}	Forward activation rate constant between closed and open states	4,000 s^{-1}
k_{CaTmo}	Backward activation rate constant between open and closed states	25.0exp(–V/34.0) s^{-1}
k_{CaTpi}	Forward inactivation rate constant	70.0 s^{-1}
k_{CaTmi}	Backward inactivation rate constant	0.98 s^{-1}
f_{CaT}	Allosteric factor for inactivation	0.2
h_{CaT}	Allosteric factor for recovery from inactivation	0.5
G_{CaT}	Specific maximum conductivity for T-type Ca^{2+} channel (non-phosphorylated)	0.01275 mS/µF
G_{CaTp}	Specific maximum conductivity for T-type Ca^{2+} channel (phosphorylated)	0.02545 mS/µF
f_{ICaT}^{cav}	Fraction of the T-type Ca^{2+} channels located in caveolae	0.68
$E_{CaT,rev}$	Reversal potential of the T-type Ca^{2+} current	35.0 mV
k_{ICaT_PKA}	Phosphorylation rate of the T-type Ca^{2+} channel by PKA	0.174 μM^{-1} s^{-1}
k_{ICaT_PP}	Dephosphorylation rate of the T-type Ca^{2+} channel by PP1 and PP2A	0.0466 μM^{-1} s^{-1}
K_{ICaT_PKA}	Relative affinity of the T-type Ca^{2+} channel for PKA	5.0
K_{ICaT_PP}	Relative affinity of the T-type Ca^{2+} channel for PP1 and PP2A	0.1

$$I_{CaT} = I_{CaT}^{cav} + I_{CaT}^{cyt} \qquad (A.1.1)$$

$$I_{CaT}^{cav} = f_{ICaT}^{cav}\left(G_{CaT}\left(1 - f_{CaT,p}^{cav}\right) + G_{CaTp} f_{CaT,p}^{cav}\right) O_{CaT}\left(V - E_{CaT,rev}\right) \quad (A.1.2)$$

$$I_{CaT}^{cyt} = \left(1 - f_{ICaT}^{cav}\right)\left(G_{CaT}\left(1 - f_{CaT,p}^{cyt}\right) + G_{CaTp} f_{CaT,p}^{cyt}\right) O_{CaT}\left(V - E_{CaT,rev}\right) \quad (A.1.3)$$

$$\frac{dC_{0,CaT}}{dt} = k_{CaTmv} C_{1,CaT} - 4k_{CaTpv} C_{0,CaT} + \frac{k_{CaTmi}}{h_{CaT}^3} I_{0,CaT} - k_{CaTpi} f_{CaT}^3 C_{0,CaT} \quad (A.1.4)$$

$$\frac{dC_{1,CaT}}{dt} = 4k_{CaTpv} C_{0,CaT} - k_{CaTmv} C_{1,CaT} + 2k_{CaTmv} C_{2,CaT} - 3k_{CaTpv} C_{1,CaT} + \frac{k_{CaTmi}}{h_{CaT}^2} I_{1,CaT} - k_{CaTpi} f_{CaT}^2 C_{1,CaT} \quad (A.1.5)$$

$$\frac{dC_{2,CaT}}{dt} = 3k_{CaTpv} C_{1,CaT} - 2k_{CaTmv} C_{2,CaT} + 3k_{CaTmv} C_{3,CaT} - 2k_{CaTpv} C_{2,CaT} + \frac{k_{CaTmi}}{h_{CaT}} I_{2,CaT} - k_{CaTpi} f_{CaT} C_{2,CaT} \quad (A.1.6)$$

$$\frac{dC_{3,CaT}}{dt} = 2k_{CaTpv} C_{2,CaT} - 3k_{CaTmv} C_{3,CaT} + 4k_{CaTmv} C_{4,CaT} - k_{CaTpv} C_{3,CaT} + k_{CaTmi} I_{3,CaT} - k_{CaTpi} C_{3,CaT} \quad (A.1.7)$$

$$\frac{dC_{4,CaT}}{dt} = k_{CaTpv} C_{3,CaT} - 4k_{CaTmv} C_{4,CaT} + k_{CaTmo} O_{CaT} - k_{CaTpo} C_{4,CaT} + k_{CaTmi} I_{4,CaT} - k_{CaTpi} C_{4,CaT} \quad (A.1.8)$$

$$\frac{dO_{CaT}}{dt} = k_{CaTpo} C_{4,CaT} - k_{CaTmo} O_{CaT} + k_{CaTmi} I_{O,CaT} - k_{CaTpi} O_{CaT} \quad (A.1.9)$$

$$\frac{dI_{0,CaT}}{dt} = k_{CaTmv} h_{CaT} I_{1,CaT} - \frac{4k_{CaTpv}}{f_{CaT}} I_{0,CaT} + k_{CaTpi} f_{CaT}^3 C_{0,CaT} - \frac{k_{CaTmi}}{h_{CaT}^3} I_{0,CaT} \quad (A.1.10)$$

$$\frac{dI_{1,CaT}}{dt} = \frac{4k_{CaTpv}}{f_{CaT}} I_{0,CaT} - k_{CaTmv} h_{CaT} I_{1,CaT} + 2k_{CaTmv} h_{CaT} I_{2,CaT} - \frac{3k_{CaTpv}}{f_{CaT}} I_{1,CaT} + k_{CaTpi} f_{CaT}^2 C_{1,CaT} - \frac{k_{CaTmi}}{h_{CaT}^2} I_{1,CaT} \quad (A.1.11)$$

$$\frac{dI_{2,CaT}}{dt} = \frac{3k_{CaTpv}}{f_{CaT}} I_{1,CaT} - 2k_{CaTmv} h_{CaT} I_{2,CaT} + 3k_{CaTmv} h_{CaT} I_{3,CaT} - \frac{2k_{CaTpv}}{f_{CaT}} I_{2,CaT} + k_{CaTpi} f_{CaT} C_{2,CaT} - \frac{k_{CaTmi}}{h_{CaT}} I_{2,CaT} \quad (A.1.12)$$

$$\frac{dI_{3,CaT}}{dt} = \frac{2k_{CaTpv}}{f_{CaT}} I_{2,CaT} - 3k_{CaTmv} h_{CaT} I_{3,CaT} + 4k_{CaTmv} I_{4,CaT} - k_{CaTpv} I_{3,CaT} + k_{CaTpi} C_{3,CaT} - k_{CaTmi} I_{3,CaT} \quad (A.1.11)$$

$$\frac{dI_{4,CaT}}{dt} = k_{CaTpv} I_{3,CaT} - 4k_{CaTmv} I_{4,CaT} + k_{CaTmo} I_{O,CaT} - k_{CaTpo} I_{4,CaT} + k_{CaTpi} C_{4,CaT} - k_{CaTmi} I_{4,CaT} \quad (A.1.14)$$

$$\frac{dI_{O,CaT}}{dt} = k_{CaTpo} I_{4,CaT} - k_{CaTmo} I_{O,CaT} + k_{CaTpi} O_{CaT} - k_{CaTmi} I_{O,CaT} \quad (A.1.15)$$

$$\frac{df_{CaT,p}^{cav}}{dt} = k_{ICaT\_PKA} \frac{(1 - f_{CaT,p}^{cav})[C]^{cav}}{K_{ICaT\_PKA} + (1 - f_{CaT,p}^{cav})} - k_{ICaT_{PP}} \frac{f_{CaT,p}^{cav}[PP]^{cav}}{K_{ICaT_{PP}} + f_{CaT,p}^{cav}} \quad (A.1.16)$$

$$\frac{df_{CaT,p}^{cyt}}{dt} = k_{ICaT\_PKA} \frac{(1 - f_{CaT,p}^{cyt})[C]^{cyt}}{K_{ICaT\_PKA} + (1 - f_{CaT,p}^{cyt})} - k_{ICaT_{PP}} \frac{f_{CaT,p}^{cyt}([PP2A]^{cyt} + [PP1]_{f}^{cyt})}{K_{ICaT_{PP}} + f_{CaT,p}^{cyt}} \quad (A.1.17)$$

Appendix A.2 Small-conductance Ca^{2+}-activated K^+ Current ($I_{K,Ca}$)

Parameter	Definition	Value
k_{KCaf1}	Forward activation rate constant between closed states	120.0$[Ca^{2+}]_i$ s^{-1}
k_{KCaf2}	Forward activation rate constant between closed states	96.0$[Ca^{2+}]_i$ s^{-1}
k_{KCaf3}	Forward activation rate constant between closed states	48.0$[Ca^{2+}]_i$ s^{-1}
k_{KCab1}	Backward activation rate constant between closed states	80.0 s^{-1}
k_{KCab2}	Backward activation rate constant between closed states	80.0 s^{-1}
k_{KCab3}	Backward activation rate constant between closed states	200.0 s^{-1}
k_{KCafo1}	Forward activation rate constant between closed and open states	160.0 s^{-1}
k_{KCafo2}	Forward activation rate constant between closed and open states	1200.0 s^{-1}

k_{KCabo1}	Backward activation rate constant between closed and open states	1000.0 s^{-1}
k_{KCabo2}	Backward activation rate constant between closed and open states	100.0 s^{-1}
k_{KCa_PKA}	Phosphorylation rate of the small-conductance Ca^{2+}-activated K^+ channel by PKA	0.001479 μM^{-1} s^{-1}
k_{KCa_PP}	Dephosphorylation rate of the small-conductance Ca^{2+}-activated K^+ channel by PP1 and PP2A	0.00029125 μM^{-1} s^{-1}
K_{KCa_PKA}	Relative affinity of the small-conductance Ca^{2+}-activated K^+ channel for PKA	2.5
K_{KCa_PP}	Relative affinity of the small-conductance Ca^{2+}-activated K^+ channel for PP1 and PP2A	0.01

$$I_{K,Ca} = G_{K,Ca}(V)\left(O_{1K,Ca} + O_{2K,Ca}\right)\left(1 - f_{K,Cap}^{cav}\right) \quad (A.2.1)$$

$$G_{K,Ca}(V) = 4.4 \cdot 10^{-6}V^3 + 4.0 \cdot 10^{-4}V^2 + 0.0164V + 0.7488 \ \ (\frac{mS}{\mu F}) \quad (A.2.2)$$

$$\frac{dC_{1,KCa}}{dt} = k_{KCab1}C_{2,KCa} - k_{KCaf1}C_{1,KCa} \quad (A.2.3)$$

$$\frac{dC_{2,KCa}}{dt} = k_{KCaf1}C_{1,KCa} - k_{KCab1}C_{2,KCa} + k_{KCab2}C_{3,KCa} - k_{KCaf2}C_{2,KCa} \quad (A.2.4)$$

$$\frac{dC_{3,KCa}}{dt} = k_{KCaf2}C_{2,KCa} - k_{KCab2}C_{3,KCa} + k_{KCab3}C_{4,KCa} - k_{KCaf3}C_{3,KCa} + k_{KCabo1}O_{1,KCa} - k_{KCafo1}C_{3,KCa} \quad (A.2.5)$$

$$\frac{dC_{4,KCa}}{dt} = k_{KCaf3}C_{3,KCa} - k_{KCab3}C_{4,KCa} + k_{KCabo2}O_{2,KCa} - k_{KCafo2}C_{4,KCa} \quad (A.2.6)$$

$$\frac{dO_{1,KCa}}{dt} = k_{KCafo1}C_{3,KCa} - k_{KCabo1}O_{1,KCa} \quad (A.2.7)$$

$$\frac{dO_{2,KCa}}{dt} = k_{KCafo2}C_{4,KCa} - k_{KCabo2}O_{2,KCa} \quad (A.2.8)$$

$$\frac{df_{K,Cap}^{cav}}{dt} = k_{KCa\_PKA}\frac{(1 - f_{K,Cap}^{cav})[C]^{cav}}{K_{KCa\_PKA} + (1 - f_{K,Cap}^{cav})} - k_{KCa_{PP}}\frac{f_{K,Cap}^{cav}[PP]^{cav}}{K_{KCa_{PP}} + f_{K,Cap}^{cav}} \quad (A.2.9)$$

Appendix A.3 Rapidly activating, slowly inactivating K^+ current encoded by Kv1.5 ($I_{K,slow1}$)

Parameter	Definition	Value
k_{Kslow1_PKA}	Phosphorylation rate of the rapidly activating, slowly inactivating K^+ channel by PKA	6.9537×10^{-3} μM^{-1} s^{-1}
k_{Kslow1_PP}	Dephosphorylation rate of the rapidly activating, slowly inactivating K^+ channel by PP1	3.170×10^{-2} μM^{-1} s^{-1}
K_{Kslow1_PKA}	Relative affinity of the rapidly activating, slowly inactivating K^+ channel for PKA	0.138115
K_{Kslow1_PP}	Relative affinity of the rapidly activating, slowly inactivating K^+ channel for PP1	0.23310

$$I_{K,slow1} = \left(G_{K,slow1} f_{K,slow1}^{ecav} + G_{K,slow1p}\left(1 - f_{K,slow1}^{ecav}\right)\right) a_{K,slow1} i_{K,slow1} (V - E_K) \qquad (A.3.1)$$

$$E_K = \frac{RT}{F} ln\left(\frac{[K^+]_o}{[K^+]_i}\right) \qquad (A.3.2)$$

$$\frac{df_{K,slow1}^{ecav}}{dt} = k_{Kslow1\_PP} \frac{(1 - f_{K,slow1}^{ecav})[PP1]^{ecav}}{K_{Kslow1\_PP} + (1 - f_{K,slow1}^{ecav})} - k_{Kslow1_{PKA}} \frac{f_{K,slow1}^{ecav}[C]^{ecav}}{K_{Kslow1_{PKA}} + f_{K,slow1}^{ecav}} \qquad (A.3.3)$$

$$\frac{da_{K,slow1}}{dt} = \frac{a_{ss} - a_{K,slow1}}{\tau_{aK,slow1}} \qquad (A.3.4)$$

$$\frac{di_{K,slow1}}{dt} = \frac{i_{ss} - i_{K,slow1}}{\tau_{iK,slow1}} \qquad (A.3.5)$$

$$a_{ss} = \frac{1}{1 + e^{-(V+22.5)/7.7}} \qquad (A.3.6)$$

$$i_{ss} = \frac{1}{1 + e^{(V+45.2)/5.7}} \qquad (A.3.7)$$

$$\tau_{aK,slow1} = \frac{6.1}{e^{0.0629(V+40.0)} + e^{-0.0629(V+40.0)}} + 2.058 \qquad (A.3.8)$$

$$\tau_{iK,slow1} = 803.0 - \frac{18.0}{1 + e^{\frac{V+45.2}{5.7}}} \quad (A.3.9)$$

Appendix A.4 Rapidly Activating, Slowly Inactivating K^+ Current Encoded by Kv2.1 ($I_{K,slow2}$)

$$I_{K,slow2} = G_{K,slow2} a_{K,slow2} i_{K,slow2} (V - E_K) \quad (A.4.1)$$

$$a_{K,slow2} = a_{K,slow1} \quad (A.4.2)$$

$$\frac{di_{K,slow2}}{dt} = \frac{i_{ss} - i_{K,slow2}}{\tau_{iK,slow2}} \quad (A.4.3)$$

$$\tau_{iK,slow1} = 5334.0 - \frac{4912.0}{1 + e^{\frac{V+45.2}{5.7}}} \quad (A.4.4)$$

Appendix A.5 Ionic Concentrations $[Ca^{2+}]_i$ and $[K^+]_i$

$$\frac{d[Ca^{2+}]_i}{dt} = B_i \left\{ J_{leak} + J_{xfer} - J_{up} - J_{trpn} - (I_{Cab} - 2I_{NaCa} + I_{p(Ca)} + I_{CaL}^{cav} + I_{CaT}) \frac{A_{cap} C_m}{2V^{cyt} F} \right\} \quad (A.5.1)$$

$$\frac{d[K^+]_i}{dt} = -\left(I_{Kto,f} + I_{K,slow1} + I_{K,slow2} + I_{Kss} + I_{K1} + I_{Kr} + I_{K,Ca} - 2I_{NaK} - I_{stim} \right) \frac{A_{cap} C_m}{V^{cyt} F} \quad (A.5.2)$$

Appendix B: Heart Failure Model Parameters and Equations

The mathematical model of the combined β1- and β2-adrenergic signaling system in failing mouse ventricular myocytes consists of the model equations (Appendix B.1)-(Appendix B.6) and model parameters presented in this Appendix plus model equations (A.64)-(A.301) and model parameters from (Bondarenko 2014) and model equations (A.1)-(A125) and model parameters from (Rozier & Bondarenko, 2017).

Appendix B.1 Rapidly Activating, Slowly Inactivating K^+ Current Encoded by $K_v1.5$ ($I_{K,slow1}$)

Parameter	Definition	Value
$\boldsymbol{k_{Kslow1\_PKA}}$	Phosphorylation rate of the rapidly activating, slowly inactivating K^+ channel by PKA	6.9537×10^{-3} μM^{-1} s^{-1}
$\boldsymbol{k_{Kslow1\_PP}}$	Dephosphorylation rate of the rapidly activating, slowly inactivating K^+ channel by PP1	3.170×10^{-2} μM^{-1} s^{-1}
$\boldsymbol{K_{Kslow1\_PKA}}$	Relative affinity of the rapidly activating, slowly inactivating K^+ channel for PKA	0.138115
$\boldsymbol{K_{Kslow1\_PP}}$	Relative affinity of the rapidly activating, slowly inactivating K^+ channel for PP1	0.23310

$$I_{K,slow1} = \left(G_{K,slow1} f_{K,slow1}^{ecav} + G_{K,slow1p}\left(1 - f_{K,slow1}^{ecav}\right)\right) a_{K,slow1} i_{K,slow1} (V - E_K) \qquad (B.1.1)$$

$$E_K = \frac{RT}{F} ln\left(\frac{[K^+]_o}{[K^+]_i}\right) \qquad (B.1.2)$$

$$\frac{df_{K,slow1}^{ecav}}{dt} = k_{Kslow1\_PP} \frac{(1 - f_{K,slow1}^{ecav})[PP1]^{ecav}}{K_{Kslow1\_PP} + (1 - f_{K,slow1}^{ecav})} - k_{Kslow1_{PKA}} \frac{f_{K,slow1}^{ecav}[C]^{ecav}}{K_{Kslow1_{PKA}} + f_{K,slow1}^{ecav}} \qquad (B.1.3)$$

$$\frac{da_{K,slow1}}{dt} = \frac{a_{ss} - a_{K,slow1}}{\tau_{aK,slow1}} \qquad (B.1.4)$$

$$\frac{di_{K,slow1}}{dt} = \frac{i_{ss} - i_{K,slow1}}{\tau_{iK,slow1}} \quad (B.1.5)$$

$$a_{ss} = \frac{1}{1 + e^{-(V+22.5)/7.7}} \quad (B.1.6)$$

$$i_{ss} = \frac{1}{1 + e^{(V+45.2)/5.7}} \quad (B.1.7)$$

$$\tau_{aK,slow1} = \frac{6.1}{e^{0.0629(V+40.0)} + e^{-0.0629(V+40.0)}} + 2.058 \quad (B.1.8)$$

$$\tau_{iK,slow1} = 803.0 - \frac{18.0}{1 + e^{\frac{V+45.2}{5.7}}} \quad (B.1.9)$$

Appendix B.2 Rapidly Activating, Slowly Inactivating K^+ Current Encoded by $K_v2.1$ ($I_{K,slow2}$)

$$I_{K,slow2} = G_{K,slow2} a_{K,slow2} i_{K,slow2} (V - E_K) \quad (B.2.1)$$

$$a_{K,slow2} = a_{K,slow1} \quad (B.2.2)$$

$$\frac{di_{K,slow2}}{dt} = \frac{i_{ss} - i_{K,slow2}}{\tau_{iK,slow2}} \quad (B.2.3)$$

$$\tau_{iK,slow1} = 5334.0 - \frac{4912.0}{1 + e^{\frac{V+45.2}{5.7}}} \quad (B.2.4)$$

Appendix B.3 Late Na^+ current $I_{Na,L}$

Parameter	Definition	Value
k_{INaL_PKA}	Phosphorylation rate of the late Na^+ channel by PKA	2.520×10^{-2} μM^{-1} s^{-1}
k_{INaL_PP}	Dephosphorylation rate of the late Na^+ channel by PP1	5.941×10^{-2} μM^{-1} s^{-1}
K_{INaL_PKA}	Relative affinity of the late Na^+ channel for PKA	0.0549415
K_{NaL_PP}	Relative affinity of the late Na^+ channel for PP1	0.78605

$$I_{NaL} = \left(G_{NaL}(1 - f_{INaL}^{cav}) + G_{NaLp} f_{INaL}^{cav}\right) a_{NaL}^3 h_{NaL}(V - E_{NaL}) \qquad (B.3.1)$$

$$E_{NaL} = \frac{RT}{F} ln\left(\frac{[Na^+]_o}{[Na^+]_i}\right) \qquad (B.3.2)$$

$$\alpha_{mNaL} = \frac{0.32(V + 47.13)}{1 - exp(-0.1(V + 47.13))} \qquad (B.3.3)$$

$$\beta_{mNaL} = 0.08\, exp\left(-\frac{V}{11.0}\right) \qquad (B.3.4)$$

$$h_{NaL}^{\infty} = \frac{1}{1 + exp((V + 91)/6.1)} \qquad (B.3.5)$$

$$\frac{da_{NaL}}{dt} = \alpha_{mNaL}(1 - a_{NaL}) - \beta_{mNaL} a_{NaL} \qquad (B.3.6)$$

$$\frac{dh_{NaL}}{dt} = \frac{h_{NaL}^{\infty} - h_{NaL}}{\tau_{NaL}} \qquad (B.3.7)$$

$$\frac{df_{INaL}^{cav}}{dt} = k_{INaL\_PKA} \frac{(1 - f_{INaL}^{cav})[C]^{cav}}{K_{INaL\_PKA} + (1 - f_{INaL}^{cav})} - k_{INaL_{PP}} \frac{f_{INaL}^{cav}[PP]^{cav}}{K_{INaL_{PP}} + f_{INaL}^{cav}} \qquad (B.3.8)$$

Appendix B.4 Ryanodine Receptors

$$\frac{dP_{RyR}}{dt} = -0.04P_{RyR} - 0.1\frac{I_{CaL}}{I_{CaL,max}}\, e^{-\frac{(V+5.0)^2}{648.0}} \qquad (\boldsymbol{Control}) \qquad (B.4.1a)$$

$$\frac{dP_{RyR}}{dt} = -0.008P_{RyR} - 0.07\frac{I_{CaL}}{I_{CaL,max}}\, e^{-\frac{(V+5.0)^2}{648.0}} \qquad (\boldsymbol{Heart\ failure}) \qquad (B.4.1b)$$

Appendix B.5 Ca^{2+} Leak Rate Constant from the NSR

$$\nu_2 = (1.2701 + 3.6045[C]^{ecav}) \cdot 10^{-5}\ ms^{-1} \qquad (\boldsymbol{Control}) \qquad (B.5.1a)$$

$$\nu_2 = 1.15 \cdot (1.2701 + 3.6045[C]^{ecav}) \cdot 10^{-5}\ ms^{-1} \qquad (\boldsymbol{Heart\ failure}) \qquad (B.5.1b)$$

Appendix B.6 Ionic Concentrations

$$\frac{d[Ca^{2+}]_i}{dt} = B_i \left\{ J_{leak} + J_{xfer} - J_{up} - J_{trpn} - (I_{Cab} - 2I_{NaCa} + I_{p(Ca)} + I_{CaL}^{cav}) \frac{A_{cap} C_m}{2V^{cyt} F} \right\} \quad (\textbf{Control}) \quad (B.6.1a)$$

$$\frac{d[Ca^{2+}]_i}{dt} = B_i \left\{ J_{leak} + J_{xfer} - J_{up} - J_{trpn} - (I_{Cab} - 2I_{NaCa} + I_{p(Ca)} + I_{CaL}^{cav} + 0.5 I_{CaL}^{ecav}) \frac{A_{cap} C_m}{2V^{cyt} F} \right\} \quad (\textbf{Heart failure}) \quad (B.6.1b)$$

$$\frac{d[Ca^{2+}]_{ss}}{dt} = B_{ss} \left\{ J_{rel} \frac{V_{JSR}}{V_{ss}} - J_{xfer} \frac{V^{cyt}}{V_{ss}} - I_{CaL}^{ecav} \frac{A_{cap} C_m}{2V_{ss} F} \right\} \quad (\textbf{Control}) \quad (B.6.2a)$$

$$\frac{d[Ca^{2+}]_{ss}}{dt} = B_{ss} \left\{ J_{rel} \frac{V_{JSR}}{V_{ss}} - J_{xfer} \frac{V^{cyt}}{V_{ss}} - 0.5 I_{CaL}^{ecav} \frac{A_{cap} C_m}{2V_{ss} F} \right\} \quad (\textbf{Heart failure}) \quad (B.6.2b)$$

$$\frac{d[K^+]_i}{dt} = -\left(I_{Kto,f} + I_{K,slow1} + I_{K,slow2} + I_{Kss} + I_{K1} + I_{Kr} - 2I_{NaK} - I_{stim}\right) \frac{A_{cap} C_m}{V^{cyt} F} \quad (B.6.3)$$

$$\frac{d[Na^+]_i}{dt} = -(I_{Na} + I_{NaL} + I_{Nab} + 3I_{NaCa} + 3I_{NaK}) \frac{A_{cap} C_m}{V^{cyt} F} \quad (B.6.4)$$